

2000

Across-shelf sediment transport modeling and its application to storms at Duck, North Carolina

Guan-hong. Lee

College of William and Mary - Virginia Institute of Marine Science

Follow this and additional works at: <https://scholarworks.wm.edu/etd>



Part of the [Oceanography Commons](#)

Recommended Citation

Lee, Guan-hong., "Across-shelf sediment transport modeling and its application to storms at Duck, North Carolina" (2000). *Dissertations, Theses, and Masters Projects*. Paper 1539616735.

<https://dx.doi.org/doi:10.25773/v5-f908-bv18>

This Dissertation is brought to you for free and open access by the Theses, Dissertations, & Master Projects at W&M ScholarWorks. It has been accepted for inclusion in Dissertations, Theses, and Masters Projects by an authorized administrator of W&M ScholarWorks. For more information, please contact scholarworks@wm.edu.

INFORMATION TO USERS

This manuscript has been reproduced from the microfilm master. UMI films the text directly from the original or copy submitted. Thus, some thesis and dissertation copies are in typewriter face, while others may be from any type of computer printer.

The quality of this reproduction is dependent upon the quality of the copy submitted. Broken or indistinct print, colored or poor quality illustrations and photographs, print bleedthrough, substandard margins, and improper alignment can adversely affect reproduction.

In the unlikely event that the author did not send UMI a complete manuscript and there are missing pages, these will be noted. Also, if unauthorized copyright material had to be removed, a note will indicate the deletion.

Oversize materials (e.g., maps, drawings, charts) are reproduced by sectioning the original, beginning at the upper left-hand corner and continuing from left to right in equal sections with small overlaps.

Photographs included in the original manuscript have been reproduced xerographically in this copy. Higher quality 6" x 9" black and white photographic prints are available for any photographs or illustrations appearing in this copy for an additional charge. Contact UMI directly to order.

**Bell & Howell Information and Learning
300 North Zeeb Road, Ann Arbor, MI 48106-1346 USA
800-521-0600**

UMI[®]

**ACROSS-SHELF SEDIMENT TRANSPORT MODELING AND ITS APPLICATION
TO STORMS AT DUCK, NORTH CAROLINA**

**A Dissertation
Presented to
The Faculty of the School of Marine Science
The College of William and Mary**

**In Partial Fulfillment
Of the Requirement for the Degree of
Doctor of Philosophy**

by

**Guan-hong Lee
2000**

UMI Number: 9974958

UMI[®]

UMI Microform 9974958

Copyright 2000 by Bell & Howell Information and Learning Company.

All rights reserved. This microform edition is protected against
unauthorized copying under Title 17, United States Code.

Bell & Howell Information and Learning Company
300 North Zeeb Road
P.O. Box 1346
Ann Arbor, MI 48106-1346

APPROVAL SHEET


This dissertation is submitted in partial fulfillment of

the requirements for the degree of

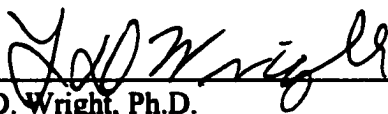
Doctor of Philosophy


Guan-hong Lee


Approved, August 2000



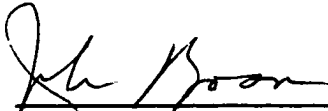
Carl T. Friedrichs, Ph.D.
Committee Co-Chairman/Co-Advisor



L. D. Wright, Ph.D.
Committee Co-Chairman/Co-Advisor




Jerome Maa, Ph.D.



John Boon, Ph.D.



Mark R. Patterson, Ph.D.



W. A. Birkemeier
Army Corps of Engineers
Duck, North Carolina

TABLE OF CONTENTS

	Page
ACKNOWLEDGMENTS	vi
LIST OF TABLES	vii
LIST OF FIGURES	viii
ABSTRACT	xiv
I. INTRODUCTION	2
II. EXAMINATION OF DIFFUSION VERSUS ADVECTION DOMINATED SEDIMENT SUSPENSION ON THE INNER SHELF UNDER STORM AND SWELL CONDITIONS, DUCK, N.C.	7
2.1. INTRODUCTION	7
2.2. FIELD EXPERIMENT AND ENVIRONMENTAL CONDITIONS ...	11
2.2.1. Study Site	11
2.2.2. Pod Instrumentation and Data Analysis	13
2.2.3. Environmental Conditions and Characteristics of Observed Suspended Sediment Concentrations	15
2.3. EDDY VISCOSITY AND EDDY DIFFUSIVITY	26
2.4. DIFFUSION-DOMINATED VERTICAL DISTRIBUTION OF SUSPENDED SEDIMENT	30
2.5. CRITERIA ON DIFFUSION AND ADVECTION DOMINATED SEDIMENT SUSPENSION	34
2.6. COMBINED DIFFUSION AND ADVECTION MODEL OF VERTICAL DISTRIBUTION OF SUSPENDED SEDIMENT	38
2.7. DISCUSSION AND CONCLUSIONS	42
III. FORMULATION AND IMPLEMENTATION OF A WIND AND WAVE FORCED CURRENT MODEL FOR SEDIMENT TRANSPORT ACROSS THE INNER SHELF	50
3.1. INTRODUCTION	50
3.2. FIELD DATA	53
3.2.1. Wind	53

3.2.2.	Waves	57
3.2.3.	Currents	57
3.3.	WIND-DRIVEN CURRENT MODEL	58
3.3.1.	Momentum Balance	61
3.3.2.	Bilinear Eddy Viscosity	64
3.3.3.	Constant Eddy Viscosity	69
3.3.4.	Analytical Solution with f_u Neglected	72
3.4.	WAVE AND WAVE-DRIVEN CURRENT MODEL	73
3.4.1.	Wave Orbital Velocity	74
3.4.2.	Wave Transformation	74
3.4.3.	Wave-Driven Steady Current	77
3.5.	DISCUSSION AND CONCLUSIONS	79
3.5.1.	Wind-Driven Currents	81
3.5.2.	Waves and Wave-Driven Currents	83
IV.	CROSS-SHORE SEDIMENT TRANSPORT MODELING AND ASSOCIATED MORPHOLOGICAL CHANGE ACROSS THE INNER SHELF DURING STORMS	88
4.1.	INTRODUCTION	88
4.2.	FIELD DATA	92
4.2.1.	Field Site	93
4.2.2.	Bathymetry	93
4.2.3.	Sediment	94
4.2.4.	Significant Storms	96
4.3.	SEDIMENT TRANSPORT MODEL	99
4.3.1.	Suspended Sediment	99
4.3.2.	Bedload Transport	101
4.4.	MORPHOLOGIC CHANGE MODEL	107
4.4.1.	Model Formulation	107
4.4.2.	Application to October 1996 Data Set	110
4.4.3.	Application to Multi-Storm Data Set	115

4.5. DISCUSSION AND CONCLUSIONS	120
V. CONCLUSIONS	125
LITERATURE CITED	130
VITA	137

ACKNOWLEDGMENTS

I would like to extend my most gratitude to Carl T. Friedrichs. Without his enthusiasm, direction, support and encouragement, I may have not successfully finished my research. I also thank his time reading and correcting my manuscripts which were written in lousy English, and timely, ingenious suggestions to the problems which often stalled my progress. I acknowledge L. Donelson Wright, my other co-advisor, for his interest and patience. I also want to thank other members of my advisory committee, Jerome Maa, John Boon and Mark Patterson, for their reviews of my manuscripts and interest.

I would like to extend my special thanks to Bill Birkemeier and Robert Nicholls who led me to walk out into shoreface (inner shelf) from beach, and taught me how to write papers. I thank Chris Vincent who generously allowed to use his ABS instrument and software and reminded me of the importance of bedforms. Sung Chan Kim deserves my acknowledgment for his encouragement and many hours of discussion on various issues ranging from benthic boundary layer processes to local politics of Korea.

LIST OF TABLES

Table		Page
Table 2-1.	Size fraction of bed sediment	19
Table 3-1.	Wind, wave and bottom profile data collected at the FRF.	55
Table 3-2.	Correlations and average absolute differences between observed and modeled along- and across-shelf current velocities. Parentheses indicate exclusion of data during the October 1996 storm.	66
Table 3-3.	Correlations and average absolute differences between observed and modeled across-shelf current velocities. Parentheses indicate exclusion of data during the October 1996 storm.	80
Table 4-1.	Sediment size distribution at various depths. Observed sediment size distributions are in bold. Stations without direct measurements use the nearest directly observed location.	96
Table 4-2.	Significant storms identified between 1987 and 1993.	98
Table 4-3.	Volume change on the shoreface and bottom changes at 13- m depth during storms. Volume change was observed, while bottom change at 13-m depth was modeled.	117
Table 4-4.	Significance test between shoreface volume change and bottom change induced by each component of modeled currents at 13 m depth. F-values significant at 95% confidence are in bold.	119

LIST OF FIGURES

Figure		Page
Figure 2-1.	Location map of study site. VIMS tripod was deployed at a depth of about 13 m off the Field Research Facility, Duck, North Carolina.	12
Figure 2-2.	Plan view of VIMS tripod and configuration of instruments	14
Figure 2-3.	Comparison of concentration by sand suction and ABS measurement at a distance of 54 cm from the ABS transducers.	16
Figure 2-4.	Environmental conditions during VIMS tripod deployment. Storm and swell conditions are delineated by vertical lines.	
Figure 2-5.	Sediment size fraction of trap sediment. A significant increase in percent fine sediment deposition is seen between coarser storm and swell deposits.	17
Figure 2-6.	Mean sediment concentration during the deployment. Relatively high sediment suspension occurred during the storm (4-8 October, 1996) and swell (20-21 October), but virtually no suspension during the fairweather condition (10-20 October). Bottom accreted about 20 cm during the storm.	21
Figure 2-7.	Average sediment concentration profile during the storm and swell. Near bottom sediment concentration during the storm was higher (by a factor of 2) than during the swell. However, the concentration gradient (decay rate) with elevation was greater during the storm.	23
Figure 2-8.	Intra-burst sediment concentration during storm and swell.	

Intermittent bursting and rapid decay are evident during the storm. Contrary to the storm case, bursting and sustained suspension are prevalent for the entire swell burst and responsible for steeper gradient in the higher elevation above the bed shown in Figure 2-7. 24

Figure 2-9. Observed sediment concentration at 5, 15 and 30 cmab and observed bed level change during storm and swell. Higher resuspension above the bedform crest is clearly seen during both storm and swell. A similar pattern of higher concentration above bedform crests continues up to about 20 cm during storm and above 30 cm during swell. Above 20 cmab during the storm, higher concentration does not necessarily corresponds to bedform location, indicating a different vertical mixing mechanism is at work. Solid line - F1; dash - F2; dot - F3. 25

Figure 2-10. Modeled bed roughness during storm and swell. k_b - dot; k_{br} - dash-dot; k_{bm} - dash; k_b' - solid. 28

Figure 2-11. Eddy viscosity and diffusivity profiles during storm and swell conditions. Eddy viscosity using u_{*cw} above the wave boundary layer is shown by a dot-dashed line for the swell case. Wave period (T), current speed at 1 mab (u_c) and near-bottom orbital velocity (u_b) are also shown in the figure. 29

Figure 2-12. Time-series of shear velocities during storm and swell. 31

Figure 2-13. Observed (F2) and modeled sediment concentration during storm and swell. Two-layered (Grant and Glenn, 1987) and three-layered (Madsen and Wikramanayake, 1991) Rouse equations were used to model suspended sediment concentration. 33

Figure 2-14.	Time-series of observed and modeled concentration at 5 and 30 cm ab during storm and swell conditions. Shading indicates times when the assumption of (3) is invalid.	35
Figure 2-15.	a) Time-series of scaling parameter, R , which is a ratio of the vertical advection velocity to the mean current, $u_{c,s}$ at the top of the wave boundary layer during storm and swell conditions. The vertical advection velocity, u_j , is scaled to $(\eta/\lambda)u_b$ where η and λ are the ripple height and ripple length, respectively, and u_b is the maximum near-bottom orbital velocity; b) Current velocity and near-bottom wave orbital velocity. Arbitrary line is set to delineate weak current condition.; c) Time-series of shear velocities of u_{*c} , u_{*cw} and u_{*cr} for the mean sediment size.	37
Figure 2-16.	Sediment concentration profiles during storm and swell. Combined diffusion and advection model of Nielsen (1992) is compared with the observed concentration and two-layered Rouse model.	39
Figure 2-17.	Sediment concentration profiles modeled by using three-layered combined diffusion and advection model during storm and swell are compared with those of the observed, two-layered Rouse and Nielsen's combined and advection models.	41
Figure 2-18.	Sediment concentration profiles for a weak current condition. u_{*cw} was used above the wave boundary layer in the two-layered Rouse model.	45
Figure 2-19.	Time-series of sediment concentration during storm and swell. u_{*cw} was used above the wave boundary layer when R -values are greater than 0.5.	46
Figure 2-20.	a) Observed (solid line) and predicted current velocities	

through time of EMCM2. Prediction was made by forcing the wave boundary layer as δ_w (cross), $2\delta_w$ (square) and δ_{zs} (circle) in the GMG model; b) Observed and predicted current velocities through time of ADV. The prediction scheme is the same as a); c) Height above bottom of EMCM2 and ADV, GMG wave boundary layer thickness, and top of the linearly increasing eddy diffusivity. EMCM2 - dash-dot; ADV - dash; δ_w - dot; δ_{zs} - solid line. 47

Figure 3-1. Wind velocity, surface shear stress and near-bottom wave orbital velocity during October 1996. Solid - along-shelf component of wind stress; dot - across-shelf component of wind stress. 56

Figure 3-2. Angle-corrected along-shelf current velocities at 0.93, 3.25, 5, 6.75, 8.5 and 10.5 m ab, along with (the virtually undetectable) variation associated with a 3° rotation either direction. 59

Figure 3-3. Angle-corrected across-shelf current velocities at 0.93, 3.25, 5, 6.75, 8.5 and 10.5 m ab, along with variation associated with a 3° rotation either direction 60

Figure 3-4. Time series of the largest terms in the along-shelf momentum balance at 13-m depth. Units are 10^{-5} cm/s². 63

Figure 3-5. Comparison of observed and predicted along-shelf current velocities at 6 heights. Solid - observed; dash - predicted (Jenter and Madsen); dash-dot - predicted (Mitchum and Clarke); dot - predicted (fu neglected, bilinear eddy viscosity). 67

Figure 3-6. Comparison of observed and predicted across-shelf current velocities at 6 heights. Solid - observed; dash - predicted (Jenter and Madsen); dash-dot - predicted (Mitchum and

	Clarke); dot - predicted (f_u neglected, constant A_z).	68
Figure 3-7.	a) Apparent eddy viscosity versus surface shear stress, b) Best-fit between (τ_s/ρ) and A_z with A_z lagged 3 hours behind (τ_s/ρ)	70
Figure 3-8.	Comparison of u_b . Solid - u_b converted from observed H_{m0} at 8-m depth by the FRF; dash - observed u_b at 13-m depth; + - u_b transformed from 8-m to 13-m depth.	76
Figure 3-9.	Comparison of wave directions. Legends are the same as in Figure 3-8.	78
Figure 3-10.	Vertical structure of u-components with downwelling favorable winds. Left panel shows the vertical structure during a storm, while the left panel is from a none-storm period. Solid - observed; dash - u_{x-wind} ; dot - u_{y-wind} ; dash-dot - return; circle - streaming; plus - total.	84
Figure 3-11.	Vertical structure of salinity and temperature observed at the end of the FRF pier during storm and non-storm period. Note that depth increases from the water surface to the bottom. Solid - salinity; dash - temperature.	85
Figure 4-1.	Input bathymetry. Pluses represent 25 model grid points.	95
Figure 4-2.	Comparison of shear velocities using the GMG model with observed currents and waves (solid) and predicted currents and waves (dash) at 13-m depth. a) skin friction shear velocity; b) shear velocity due to the combined effect of waves and currents; and c) shear velocity due to currents outside the wave boundary layer. Note that solid in c) is shear velocity due to currents obtained by log-fitting observed currents.	100
Figure 4-3.	Suspended sediment concentration at 5 and 20 cm ab using observed waves and currents (solid - 5 cm ab; dash - 20 cm	

	ab) and predicted waves and currents (asterid - 5 cm ab; circle - 20 cm ab).	102
Figure 4-4.	Wave-averaged suspended sediment flux for u_{x-wind} , u_{y-wind} , u_{return} and u_{stream} components along with observed sediment flux. Solid - observed; dash - u_{x-wind} ; dot - u_{y-wind} ; dash-dot - u_{return} ; plus - u_{stream} ; circle - total.	103
Figure 4-5.	Comparison of bedload transport. Solid - wave-forced bedload transport using observed instantaneous wave velocity; dash - current-enhanced bedload transport using observed instantaneous wave velocity; dot - wave-forced bedload transport using Stokes second order wave velocity; dash-dot - current-enhanced bedload transport using Stokes second order wave velocity.	105
Figure 4-6.	Basic structure of morphodynamics model.	108
Figure 4-7.	Depth-integrated instantaneous sediment flux along the across-shelf grid on October 3 (19:00 EST).	111
Figure 4-8.	a) Near-bottom wave orbital velocity. o - u_b ; x - u_{b2} ; b) Across-shelf current at 1 m ab for each wind- and wave- driven currents along the across-shelf grid on October 3 (19:00 EST). + - u_{x-wind} ; * - u_{y-wind} ; o - u_{return} ; x - u_{stream}	113
Figure 4-9.	Instantaneous bed level change induced by each sediment transport components along the across-shelf grid on October 3 (19:00 EST).	114
Figure 4-10.	Time series of modeled and observed bed level change during October 1996. Modeled bottom change by each sediment transport components are also shown. dashed line - observation; solid line - modeled total bottom change; u_{x-} u_{y-wind} (*); u_{return} (*); u_{stream} (o); $Q_{b,w}$ (x); $Q_{b,cw}$ (box).	116

ABSTRACT

A benthic boundary layer tripod supporting 6 point-measuring current meters, an acoustic Doppler current profiler, and three near-bed profiling acoustic backscatter sensors documented storm and swell conditions during October, 1996, at a depth 13 m on the inner shelf off Duck, North Carolina. Three sediment suspension models were used to examine underlying assumptions of a diffusion-settling balance in the vertical and equality between eddy viscosity and eddy diffusivity. During the storm period, diffusivity inverted from observed concentrations agreed well with viscosity derived above the wave boundary layer (WBL), indicating a diffusion-dominated process for sediment suspension. Sediment suspension models with two- and three-layered eddy viscosity reproduced the observed concentration well. During the swell period, effective diffusivity did agree with modeled viscosity due to waves within the WBL extrapolated to a height greater than the modeled WBL. It is speculated that during swell shedding vortices enhance mass and momentum exchange above the WBL. All the sediment suspension models underpredicted the observed concentrations if applied with a standard WBL. However, the Rouse models with enhanced vertical exchange incorporated via a thick WBL reproduced the observed concentrations remarkably well.

A physics-based morphodynamics model was then developed to determine which components of hydrodynamic forcing and resulting sediment transport are predicted to be most significant to morphological change outside the surf zone on the inner shelf of the Middle Atlantic Bight. Simple analytical formulations were developed for depth-dependent currents driven by the along- and across-shelf components of the wind and by waves via Stokes return flow and boundary layer streaming. Benthic boundary layer structure, sediment suspension and bedload transport were formulated using analytical models for wave-current interaction. Predicted currents and sediment concentrations were compared with observations collected at 13 m depth off Duck, NC, during October, 1996. The along-shelf current model predicted the along-shelf current structure reasonably well ($r > 0.6$). The predicted across-shelf current due to the across-shelf wind was highly correlated to observed current in the middle and upper water column (up to $r \sim 0.9$ at surface), while predicted across-shelf current forced by the along-shelf wind were more highly correlated to observed near-bed currents ($r \sim 0.4$). There was still significant disagreement between observed and predicted current velocities, particularly in the across-shelf direction. Inclusion of wave-induced currents did not improve correlations significantly. Nonetheless, inclusion of boundary layer streaming slightly increased correlations with observed near-bed currents during the storm and caused the total mean current very near the bed to turn shoreward as observed.

Bottom change was modeled for 24 significant storms which were documented by before-and-after shoreface profiles collected by the Field Research Facility of the US Army Corps of Engineers at Duck, NC, between 1987 and 1993. Significant correlations were found between observed shoreface volume change between 600-800 m offshore and predicted depth change on the inner shelf due to across-shelf sediment flux. Overall, correlations between observed and predicted change were higher for wave-driven components of sediment flux than for wind-driven components. This result contradicts previous observations from Duck which have suggested that net sediment transport across the inner shelf during storms is dominated by wind-driven currents. It is possible that the observed morphological change data used in this study is strongly influenced by surf zone processes, since the deepest available profile data was still partly inside the surf zone during significant storms.

**ACROSS-SHELF SEDIMENT TRANSPORT MODELING AND ITS APPLICATION
TO STORMS AT DUCK, NORTH CAROLINA**

I. INTRODUCTION

It is well known that storms tend to move sediment rapidly offshore, while under lower-energy conditions waves move sediment onshore, causing gradual beach accretion (e.g., Komar, 1976). Moreover, it has long been recognized that onshore-offshore sediment exchange is not confined to the average surf zone, but includes exchange across the inner shelf (Niedoroda et al, 1985; Wright et al, 1985, 1987). The inner shelf of the middle Atlantic Bight is characterized as storm dominated (Wright et al, 1994) and the most significant sediment exchange between the surf zone and the inner shelf occurs during storms. For example, Lee et al (1998) reported, through analysis of beach-nearshore profiles collected over 11 years at Duck, NC, that the shoreface/inner shelf (5-9 m depths) accreted sediment during or immediately after large storms. During the intervening periods, the inner shelf gradually lost sediments, feeding sediments onshore. These morphologic changes during storms and the intervening periods appear to play an important role in long-term profile evolution at Duck. However, Lee et al (1998) raised questions concerning the sediment source and physical mechanisms driving sediment accretion during storms on the inner shelf. This motivated the present study that attempts to understand and predict sediment transport during storms on the inner shelf.

An approach widely used to predict sediment transport on the inner shelf has been to determine the time-averaged, vertical profile of horizontal flow velocity, \bar{u} , and the time-averaged profile of sediment concentration, \bar{C} , and then calculate the profile of suspended sediment flux, $\bar{u}\bar{C}$, with the assumption that sediments are transported horizontally with the mean velocity (Nielsen, 1992). Bottom change is calculated from gradients in sediment transport. In order to predict sediment transport and resulting bottom change, the flow field must be known. The flow regime of the inner shelf is

different from that of the surf zone in that circulation is not primarily driven by wave breaking. On the inner shelf, friction associated with wind stress is important in that surface and bottom boundary layers overlap and often occupy the entire water column (Mitchum and Clarke, 1986; Wright, 1995). An important response to wind on the inner shelf of the middle Atlantic Bight occurs during 'northeasters' (extratropical storms), generating large waves and strong currents (Wright et al, 1994). Wind-driven mean currents have been reported to be the dominant forcing component determining sediment transport across the inner shelf at Duck, NC (e.g., Wright et al, 1991). Waves contribute by suspending sediments off the bed. However, recent studies have also identified important roles for waves in the mean across-shelf momentum balance (Lentz et al, 1999) and in generating wave-driven steady currents (Xu and Bowen, 1994). Thus hydrodynamic models, including both wind- and wave-driven currents, are investigated to predict the flow field across the inner shelf.

On the inner shelf, sediment resuspension occurs due to the combined action of waves and currents (Wright, 1995). Benthic boundary layer processes link the combined effects of waves and currents to sediment suspension in terms of the frictional forces (Smith, 1977; Grant and Madsen, 1986). Benthic boundary layer processes are mutually dependent on sediment size and bed forms (Wiberg and Harris, 1994). On the inner shelf, bed roughness varies considerably, ranging from a plane moving bed during storms to large ripples during fairweather (Wright, 1993). Thus, it is important to understand boundary layer processes in conjunction with micromorphodynamics, which also affects sediment suspension and sediment transport.

Most models predict wave-averaged sediment concentration for combined waves and currents by solving the steady state diffusion equation (e.g., Smith, 1977; Sleath, 1984; Glenn and Grant, 1987). The steady state diffusion equation simply states that the mechanism for time-averaged sediment suspension is a diffusive process such that upward sediment flux by turbulent diffusion is balanced by downward flux due to gravitational settling, and the sediment diffusivity in the diffusion equation is usually assumed to nearly equal to eddy viscosity (e.g., Grant and Madsen, 1996; Glenn and

Grant, 1987). This diffusion-settling balance can be a good approximation when the turbulent diffusion process is dominant, for example, during a storm. Adopting linearly increasing eddy viscosity near the bed, the Rouse equation is obtained solving the steady state diffusion equation. The vertical distribution of suspended sediment predicted by the Rouse equation is reported to agree well with measurements in unidirectional stream flow (e.g., Vanoni, 1975) and over a plane bed under waves in laboratory flumes (e.g., Ribberink and Al-Salem, 1994). However, this balance may not hold when other mechanisms than diffusion are at work. For example, when sharp-crested ripples are present under regular waves, laboratory results indicate that the dominant process for sediment suspension is vertical advection associated with the cyclic development and convection of large vortices (e.g., Sleath, 1982; Ribberink and Al-Salem, 1994). Nielsen (1992) suggested a combined diffusion and advection model to predict the vertical distribution of suspended sediment that incorporates sediment advection due to shedding vortices. Thus it is of interest under what condition the diffusion-settling balance holds. If not, which model for sediment suspension better predicts sediment suspension?

A model accounting for across-shelf transport during storms has great potential to describe inner-shelf morphodynamic processes. Previous studies of sediment flux on the inner shelf of the Middle Atlantic Bight have indicated that the largest flux rates are associated with wind-driven near bottom currents occurring during storms (Wright et al., 1991; 1994). Transport by incident waves was usually secondary during storm and fairweather conditions, causing either onshore or offshore sediment fluxes depending on the bottom morphology. However, waves caused strong onshore advection of sediment under moderate wave energy conditions, particularly when the wind was weak. Low-frequency waves and gravity made only secondary contributions to cross-shore sediment flux. Identifying which components of hydrodynamic forcing induce most the significant morphologic change is an important step toward understanding inner shelf morphodynamic processes. Thus, a physics-based morphodynamics model is developed to predict profile change during storms. The relationship between bottom change and hydrodynamic forcing, including wind- and wave-driven components, is examined.

Objectives

The overall objective of this study is to understand the morphodynamics of the inner shelf during storms. To accomplish this, several specific objectives are addressed:

- 1) Use high resolution observations of velocity and suspended sediment in the bottom boundary layer to better understand the nature of eddy diffusivity under waves and currents on the inner shelf.
- 2) Improve models of bottom boundary layer processes and sediment suspension for both diffusion- and advection-dominated cases.
- 3) Understand inner shelf physical oceanography and model the lowest order hydrodynamics fundamental to across-shelf sediment transport.
- 4) Develop a physics-based morphodynamics model to predict bottom profile changes during significant storms and compare results with existing observations of morphologic change.
- 5) Determine which components of hydrodynamic forcings and resulting sediment transport are predicted and observed to be most significant to morphologic change on the inner shelf and why.

The organization of this study is as follows:

In Chapter II, the relationship between eddy viscosity and eddy diffusivity during storm and swell conditions is examined using data collected in October 1996 on the inner shelf off Duck, NC. Sediment suspension models, including Rouse-type diffusion models, combined advection and diffusion models, and a Rouse model with a thickened WBL, are compared to determine which model best reproduces observed sediment concentration profiles. In Chapter III, wind- and wave-driven hydrodynamics are modeled in the inner shelf. In Chapter IV, sediment transport and morphologic change are modeled and the morphologic change model is applied to significant storms to identify which components of hydrodynamic forcing and resulting sediment transport are predicted to be most significant to morphological change during storms on the inner shelf of the Middle Atlantic Bight. In Chapter V, the results of this study are summarized and conclusions

are presented.

II. EXAMINATION OF DIFFUSION VERSUS ADVECTION DOMINATED SEDIMENT SUSPENSION ON THE INNER SHELF UNDER STORM AND SWELL CONDITIONS, DUCK, N.C.

2.1. INTRODUCTION

In the shelf environment, sediment resuspension and transport occur due to the combined action of waves and currents. An approach widely used to predict sediment transport rates on shelves has been to determine the time-averaged, vertical profile of horizontal velocity, u , and the time-averaged profile of sediment concentration, C , and then to calculate the profile of suspended sediment flux, uC , with the assumption that sediments are transported horizontally with the mean velocity. Many models predict the time-averaged profile of sediment concentration for combined waves and currents by solving the steady state diffusion equation (e.g., Smith, 1977; Sleath, 1984; Glenn and Grant, 1987)

The rate of change of the suspended sediment concentration at a certain elevation above the bed, z , is given by the equation of sediment volume conservation, assuming that the horizontal gradients are negligible relative to the vertical gradients

$$\frac{\partial C(t)}{\partial t} = w_s \frac{\partial C(t)}{\partial z} - \frac{\partial q_z}{\partial z} \quad (2-1)$$

where $C(t)$ is the instantaneous concentration of the suspended sediment, q_z is the upward flux of the sediment and w_s is sediment fall velocity. In the sediment diffusion model, q_z is generally described in terms of gradient diffusion

$$q_z = -\epsilon_s \frac{\partial C(t)}{\partial z} \quad (2-2)$$

The diffusive flux is proportional to the concentration gradient, $\frac{\partial C(t)}{\partial z}$, and to the sediment diffusivity, ϵ_s . Integration of (2-1), after substituting (2-2) into (2-1) and taking a time average, results in the steady state diffusion equation

$$w_s \bar{C} + \varepsilon_s \partial \bar{C} / \partial z = 0 \quad (2-3)$$

where \bar{C} indicates the time averaged concentration. This equation simply states that the mechanism for time-averaged sediment suspension is a diffusive process such that upward sediment flux by turbulent diffusion is balanced by downward flux due to gravitational settling.

To obtain an expression for ε_s , one common assumption is that

$$\varepsilon_s = \varepsilon_m = \kappa u_{*cw} z \quad \text{for } z \leq \delta_w, \quad (2-4a)$$

$$\varepsilon_s = \varepsilon_m = \kappa u_{*c} z \quad \text{for } z \geq \delta_w, \quad (2-4b)$$

where ε_m is eddy viscosity, κ is von Karman's constant (~ 0.4), u_{*cw} is shear velocity due to the combined effect of waves and current inside the wave boundary layer (WBL) of thickness $\delta_w = 2\kappa u_{*cw} / \omega$, ω is wave radian frequency, and u_{*c} is shear velocity due to currents outside δ_w (Grant and Madsen, 1986; Glenn and Grant, 1987). Using acoustic backscatter sensor (ABS) data to invert (3), Vincent and Downing (1994) reported that eddy diffusivity profiles, under combined waves and currents, increased linearly from the bed level to about 20 cm above the bed and decreased above that level. Other authors have also found linearly increasing eddy diffusivity near the bed to be scaled by the characteristic shear velocity (Sheng and Hay, 1995; Vincent and Osborne, 1995). The vertical length scale of the coherent diffusivity profile and its behavior above the linear region are subject to further research and firsthand discussion on the subject can be found in Sheng and Hay (1995). Thus, it is reasonable to take a linearly increasing eddy viscosity model at least in the near-bottom region. Integration of (2-3) using (2-4) yields the Rouse-type equation. This approach has been widely used in the shelf environment (e.g., Grant and Glenn, 1987; Vincent and Green, 1990; Li et al., 1997; Lynch et al., 1997) and the vertical distribution of suspended sediment predicted by the Rouse-type equation is reported to agree also with measurements in unidirectional stream flow (e.g., Vanoni, 1975) and over a plane bed under waves in laboratory flumes (e.g., Ribberink and Al-Salem, 1994).

The diffusion-settling balance can be a good approximation close to the bed when

the turbulent diffusion process is dominant, for example, during a storm event. However this balance may not hold when mechanisms other than diffusion are at work. When sharp-crested ripples are present under regular waves, laboratory results indicate that the dominant process of sediment suspension is no longer turbulent diffusion, but rather vertical advection associated with the cyclic development and convection of large vortices (e.g., Sleath, 1982; Ribberink and Al-Salem, 1994). The vertical distribution of suspended sediment over ripples for laboratory data has been described by (2-3) with constant eddy diffusivity, resulting in exponential profiles. In this context, eddy diffusivity represents the efficiency with which vortices eject sediment up into the water column. Both laboratory measurements (e.g., Sleath, 1982; Dick and Sleath, 1991; Van Rijn et al., 1993; Ribberink and Al-Salem, 1994) and field measurements (e.g., Nielsen, 1984; Wai et al., 1991; Vincent and Osborne, 1995) of sediment concentration have been fitted to exponential profiles when wave-induced bedforms were present and sediment advection by shedding vortices was observed (in the laboratory) or inferred (in the field).

To address vertical advection by vortices over bedforms, Nielsen (1992) proposed a wave-averaged advection model of the form

$$w_s \bar{C} - PF(z) = 0 \quad (2-5)$$

where $F(z)$ is the probability function that a given particle can reach a certain level, z , and $P = w_s C_r$ is the pickup rate where C_r is the reference concentration. Empirical results suggest a probability function of the form:

$$F(z) = (1 + 11z(k_b' A_b)^{-1/6})^{-2} \quad (2-6)$$

where k_b' is the bed roughness and A_b is the near-bottom orbital excursion. Nielsen further argued that in the presence of both advection and diffusion, the vertical distribution of suspended sediment can be described by a combined model that incorporates both effects. The steady state combined diffusion and advection equation of Nielsen is given by

$$w_s \bar{C} + \epsilon_s d \bar{C} / dz - PF(z) = 0 \quad (2-7)$$

Nielsen assumes the eddy diffusivity is constant with height such that

$$\epsilon_s = 0.016 \omega k_b' A_b \quad (2-8)$$

The combined advection and diffusion approach was tested by Lee and Hanes (1996) using ABS data collected under combined waves and currents. However, Lee and Hanes used a linearly increasing three-layered eddy viscosity model of Madsen and Wikramanayake (1991) instead of constant eddy viscosity, and examined three suspension models: pure diffusion, pure advection, and combined diffusion and advection. The model of Madsen and Wikramanayake is similar to (2-4), but with an intermediate constant ϵ_s layer inserted to keep ϵ_s continuous. Lee and Hanes showed that the pure diffusion and the combined diffusion and advection models with graded sands predicted the observed concentration well under high energy conditions. Under low energy conditions (with small ripples present), the combined diffusion and advection model performed best among the models, but it still underpredicted the steep concentration profiles observed above 10 cm above the bed (cm ab hereafter) (see Figure 2-6 of Lee and Hanes, 1996).

Previous studies reviewed here indicate that under high energy conditions turbulent diffusion is probably the dominant process for vertical mixing. Under high energy, the assumption of (2-4), perhaps slightly modified following Madsen and Wikramanayake (1991), appears to be reasonable and the diffusion model of (2-3) adequately describes the vertical distribution of suspended sediments. Under low-energy conditions when bedforms are present and vortex shedding is the dominant vertical mixing process, the assumption of (2-4) is expected to fail and the vertical distribution of suspended sediments is not expected to be well represented by (2-3). The advection model or the combined diffusion and advection model is expected to do better. To determine which mechanism for suspending sediments is dominant and which model for the vertical distribution of suspended sediment is appropriate, it is essential to further examine the assumption of (2-4). Thus, the relationship between eddy viscosity and eddy diffusivity during storm and swell conditions observed on the inner shelf off Duck, North Carolina was investigated. The interest lies, in particular, in determining under what conditions the assumptions of (2-3) and (2-4) are valid. In this chapter, the ability of Rouse-type diffusion models, combined advection and diffusion models, and a Rouse-

type model with a thickened WBL to reproduce observed sediment concentration profiles was also compared. Recently, the relative strength of waves and currents has been reported to be important in influencing the types of bedforms present and the resulting pattern of sediment suspension (e.g., Van Rijn et al., 1993; Amos et al., 1998). However, the effect of the relative strength of waves and currents on the detailed profile of eddy diffusivity and sediment concentration has not been well quantified. Thus, it was also attempted to quantify this by parameterizing the relative strength of waves and currents.

2.2. FIELD EXPERIMENT AND ENVIRONMENTAL CONDITIONS

2.2.1 Study Site

The Virginia Institute of Marine Science deployed an instrumented benthic boundary layer tripod at depth of 13 m on the inner shelf off Duck, NC (Figure 2-1), during September 26 ~ October 22, 1996. This area has relatively straight, simple offshore bathymetry. The inner shelf profile is concave upward over the region extending from the surf zone to about the 15-m isobath. Bottom sediments < 10 cm) are moderately well sorted, ranging from medium to fine sand. Silts and clays comprise less than 10% of the surficial sediment. Median sediment size of diver-collected samples was 120 μm .

Tides at the Field Research Facility are semi-diurnal with a mean range of approximately 1 m (spring tide range = 1.2 m). Average annual significant wave height is 1.0 m (1980-1991) with a standard deviation of ± 0.6 m, having a mean peak spectral period of 8.3 ± 2.6 sec (Leffler et al., 1993). Wave energy is usually higher during the winter months and lower during the spring and summer. Longshore current speed and direction display seasonal trends. Frequent, short-term reversals of the current are common, but it is generally directed to the north in the summer months and southward during the winter. Storm occurrences are dominated by frequent extratropical northeasters during the fall, winter and early spring months and occasionally by tropical

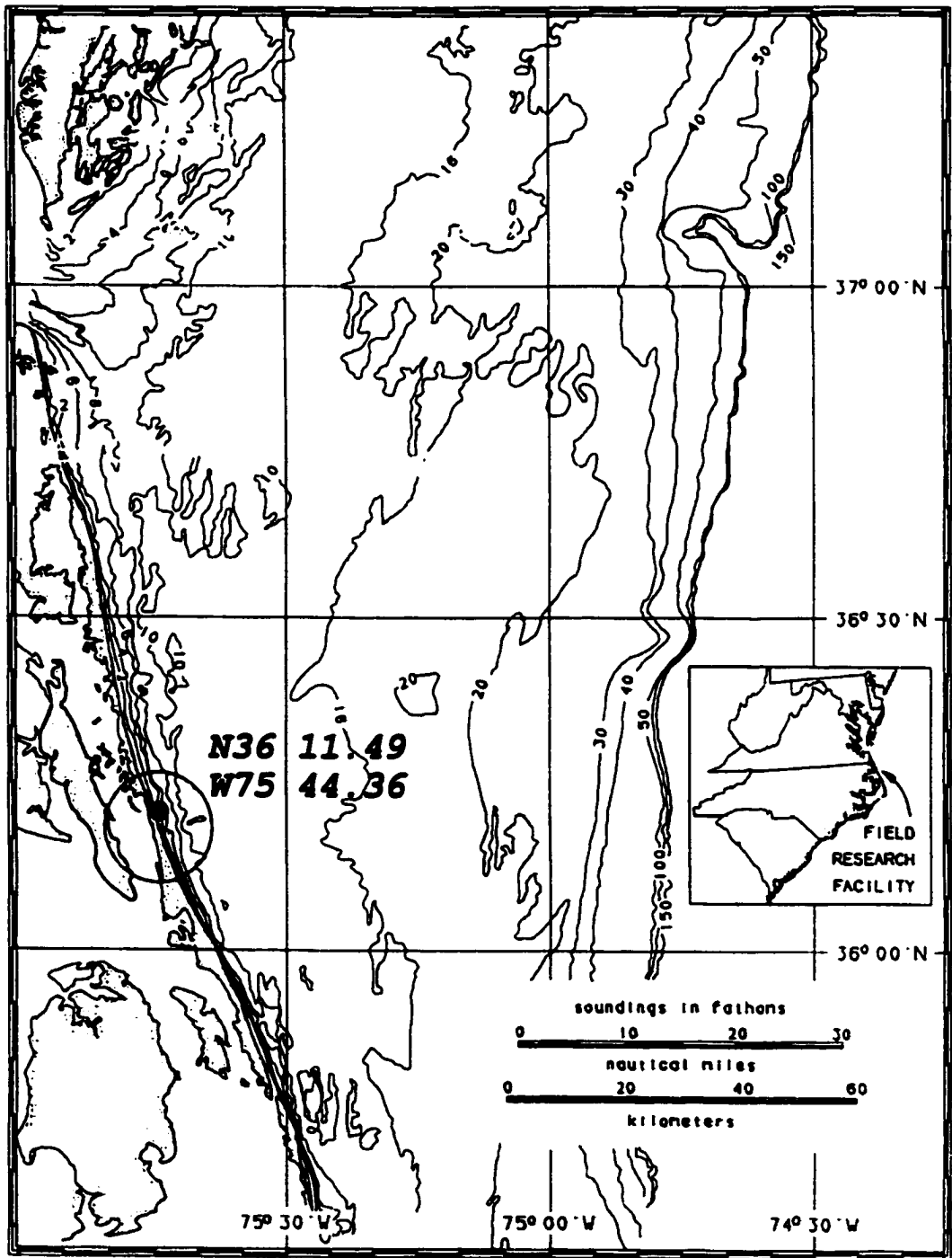


Figure 2-1. Location map of study site. VIMS tripod was deployed at a depth of about 13 m off the Field Research Facility, Duck, North Carolina

storms and hurricanes during the summer and fall season. Birkemeier et al. (1985) provide a more detailed description of the site.

2.2.2 Pod Instrumentation and Data Analysis

Instrumentation consisted of five electromagnetic current meters (EMCMs), at initial heights of 8, 38, 68, 98 and 125 cm above the bottom (ab), one pressure sensor (195 cm ab), three transceiver acoustic backscatter sensors (ABSs: all 88 cm ab) and one acoustic doppler velocimeter (ADV: 19 cm ab). A sediment trap was mounted on a leg of the pod 100 cm ab. Instrument configuration is shown in Figure 2-2. The EMCMs and pressure sensor recorded data at 1 Hz for burst durations of 34 min at 2 hour intervals, while the ABS and ADV recorded data at 5 Hz for about 12 min at 2 hour intervals. The data were recorded in self-contained data loggers. The tripod was also equipped with optical backscatter sensors (OBSs) which unfortunately fouled badly and thus OBS data were not used in this study.

Estimation of wave characteristics utilized a current meter initially located 98 cm ab. Wave components were determined by removing the mean velocity components from each burst. Wave directions were defined as the direction of maximum variance for each burst (Madsen et al., 1993). Within a burst variance of each bin (1°) was estimated by

$$\sigma_\theta = \sum_{\theta}^{\theta+1} (\bar{u}^2 + \bar{v}^2) \quad (2-9)$$

where \bar{u} and \bar{v} are the periodic components of u and v , respectively. Each bin was then averaged using an 11° low pass filter. The root mean squared (rms) wave orbital velocity for each burst was calculated from $u_b = \sqrt{2}\sigma_u$ where σ_u^2 is the total variance of the oscillatory flow. The wave orbital velocity was rotated to the dominant wave direction, and the dominant wave period was estimated by using the zero up-crossing method. In addition, the coordinate system was rotated 20° to shore parallel from true north.

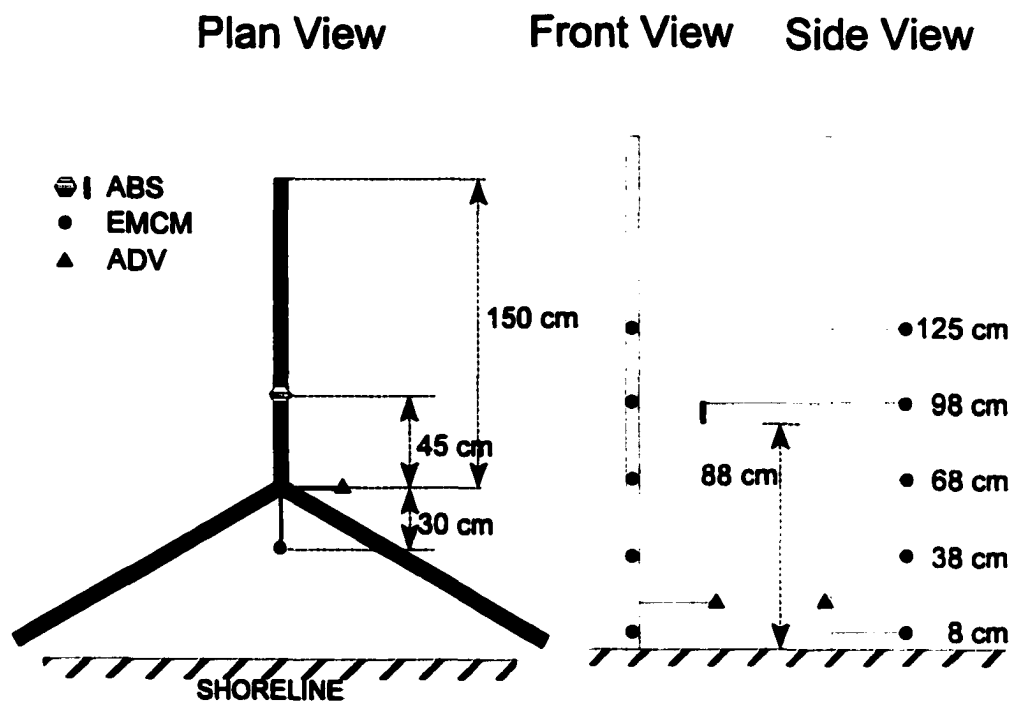


Figure 2-2. Plan view of VIMS tripod and configuration of instruments

Three ABSs, whose acoustic frequencies are 1 (F1), 2 (F2) and 5 (F3) MHz and pulse lengths are about 10 μ s, were mounted 88 cm ab, looking downward. They were stacked together and thus provided three independent measurements of sediment concentration within less than 5 cm in the horizontal direction. Range gating the backscattered acoustic signal allowed the sediment concentration profile to be estimated at 124 range bins, with a vertical resolution of 1 cm. The pulse repetition rate was 32 Hz and 6 profiles were averaged before recording the data in the data logger. A detailed description and theory of ABS can be found in Thorne et al. (1993). The ABSs were calibrated in a laboratory resuspension tank at the University of East Anglia using a mixture of sand collected in the sediment trap during the experiment and sand taken from the bottom by divers at the beginning of the experiment. The backscatter signals at 54 cm below the three ABS transducers were inverted to obtain suspended sediment concentration profiles. Figure 2-3 shows the comparison of ABS measurement and suction samples at 54 cm below the transducer.

2.2.3 Environmental Conditions and Characteristics of Observed Suspended Sediment Concentrations

On the third of October, 1996, a northeaster developed in the area and lasted about four days. During this storm, wind speed reached more than 10 m/sec and changed its direction to westward as the pressure system passed the area and moved north. The current was predominantly southward along the coast, and its peak speed reached about 50 cm/sec at the beginning of the storm and gradually decreased (Figure 2-4). On the 6th of October, current speed diminished below 10 cm/sec and then increased rapidly to over 30 cm/sec on the 7th of October, gradually decreasing afterward. Near bottom orbital velocity was about 40 cm/sec throughout the storm, and the wave period was about 9 sec. Toward the end of the deployment, there was a period of well organized swell. Wave period was about 12 sec and near bottom orbital velocity reached about 30 cm/sec. However, current speed was very weak (< 10 cm/sec) compared to that during the

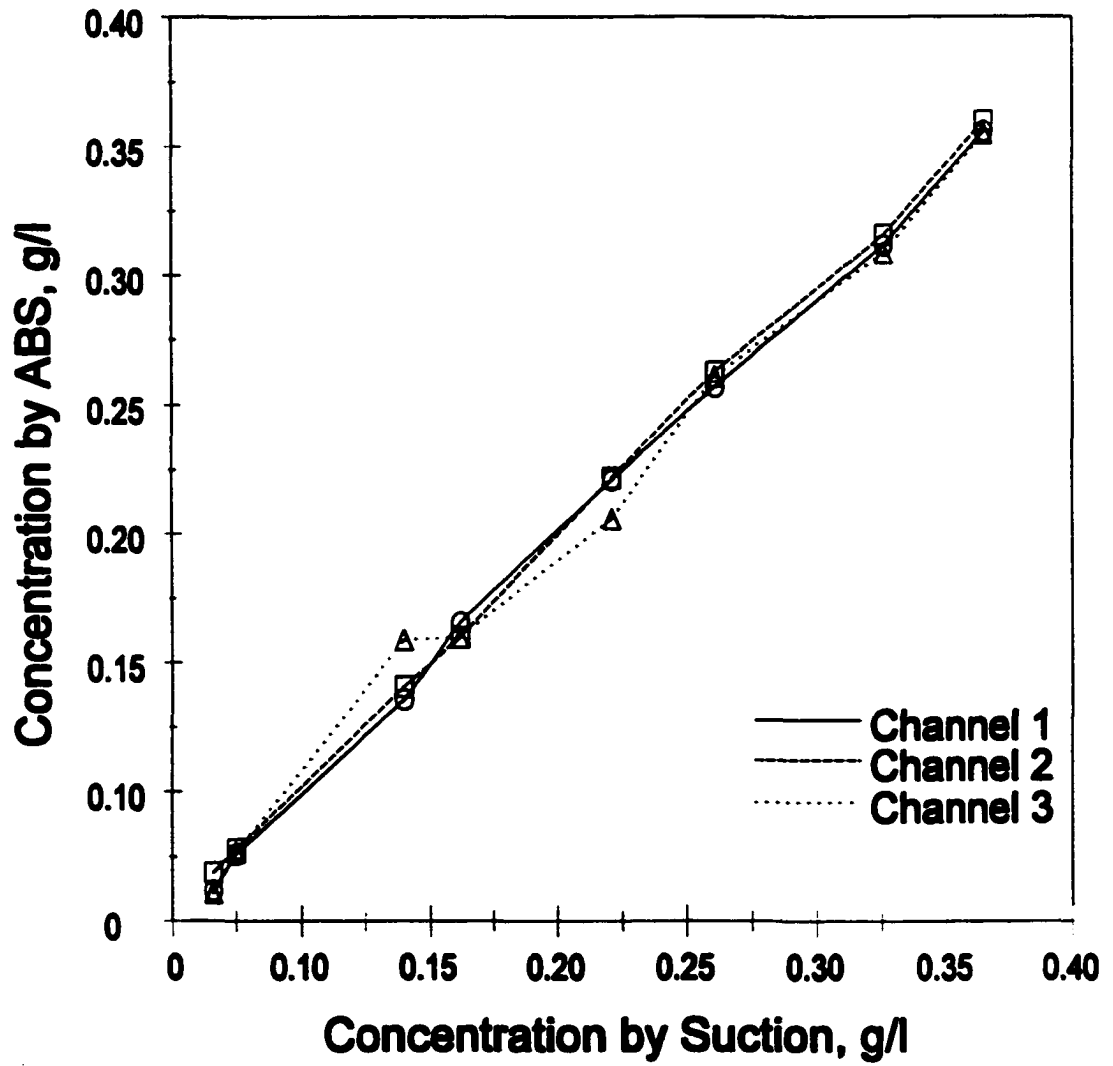


Figure 2-3. Comparison of concentration by sand suction and ABS measurement at a distance of 54 cm from the ABS transducers.

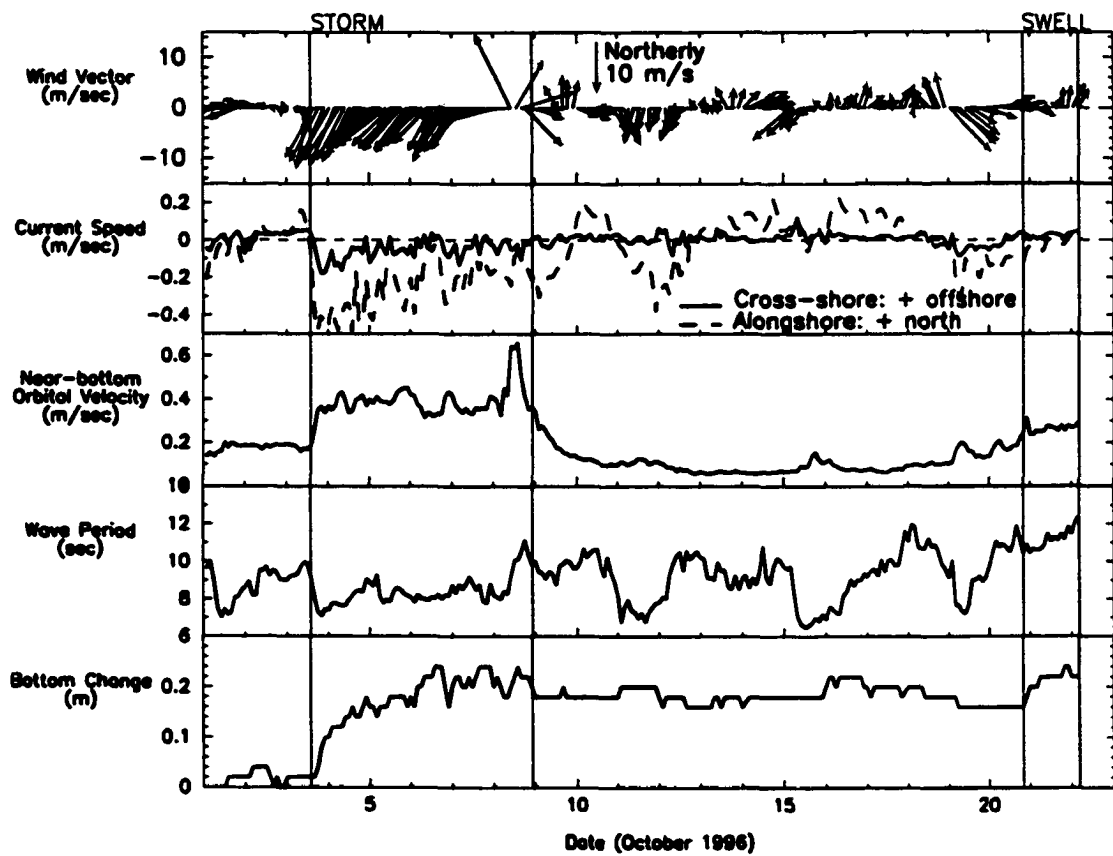


Figure 2-4. Environmental conditions during VIMS tripod deployment. Storm and swell conditions are delineated by vertical lines.

storm.

Sediment size analyses were performed for a bed sediment core collected by divers at the pod site at the start of the field experiment, and for additional sediment samples obtained in a sediment trap mounted on a leg at 100 cm ab. Both were subsampled at 1 cm intervals, producing 10 and 21 subsamples for bed and trap samples, respectively. Each subsample was divided into sand and silt/clay by wet sieving by following Folk (1968). A Rapid Sand Analyzer was used to measure sand size fractions, while a Micrometrics SediGraph was used to measure silt and clay fractions. Table 2-1 displays the depth-averaged size fractions of the bed sediment. Size fractions were almost uniform throughout the core. Fine and very fine sands comprised almost 90 percent and the silt/clay fraction comprised less than 10 percent. Within the sediment trap (Figure 2-5), there were two layers for which silt/clay comprised more than 50 percent: layers ~1 and ~16 corresponding to low energy periods at the beginning of the experiment and October 10~20, respectively. The latter distinguishes the swell deposition from the storm deposition. In the swell layers, fine and very fine sands comprised 45 and 14 percent of the total sediment, respectively. Silt and clay accounted for about 20 percent of the total sediment and coarser sediment ($< 3\phi$) comprised the rest ~20 percent. The storm layers showed a similar size distribution to the swell layers.

Bottom changes observed by the ABS (Figure 2-4e) exhibit two features: bed form migration and net bed elevation change. During the storm, it appears that mega-ripples (O(5~6 cm) in height) passed under the ABSs, whereas smaller ripples (O(2~3 cm) in height) passed under the ABSs during the more quiescent periods. Net accretion on the order of 20 cm occurred during the beginning phase of the storm and to a smaller degree during the storm (O 10 cm). It is uncertain how much of the net accretion is attributable to tripod settling.

Mean sediment concentrations obtained from the ABS (F2) are shown in Figure 2-6. Relatively high sediment suspension occurred during the storm and swell, reaching 0.1 g/l at 30 cm above the bottom, while little sediment resuspension occurred during the intervening fairweather conditions. Sediment concentration in the wave boundary layer

Sediment Size, mm	Percentage
0.354	0.69
0.210	1.90
0.149	29.15
0.105	60.03
0.074	2.84
0.044	3.23
0.007	2.16

Table 2-1. Size fraction of bed sediment

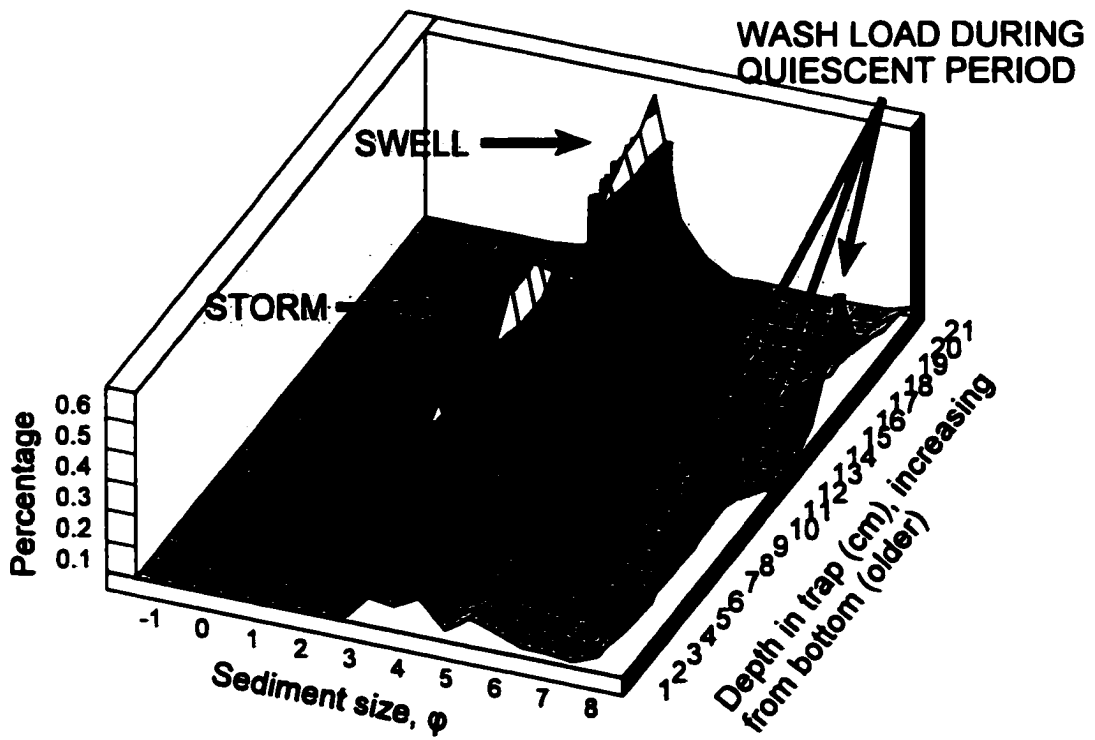


Figure 2-5. Sediment size fraction of trap sediment. A significant increase in percent fine sediment deposition is seen between coarser storm and swell deposits.

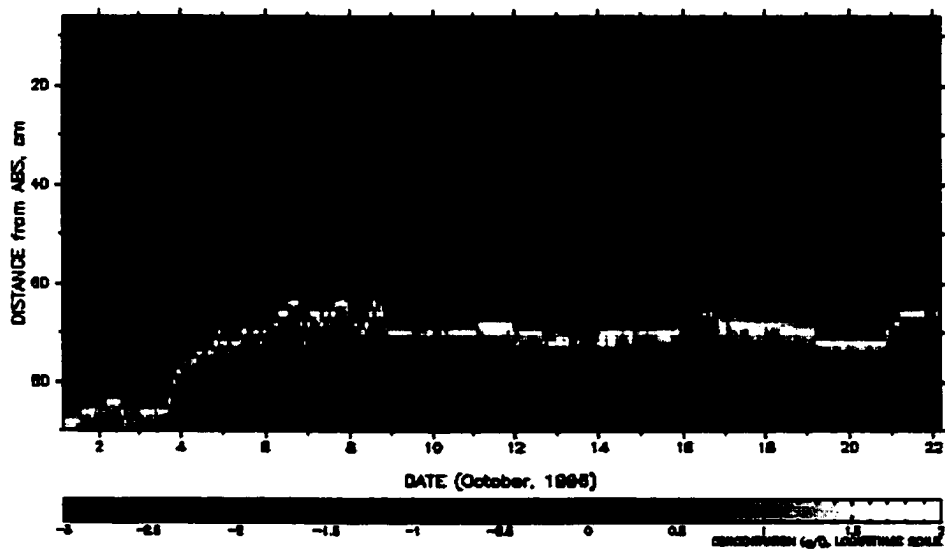


Figure 2-6. Mean sediment concentration during the deployment. Relatively high sediment suspension occurred during the storm (4-8 October, 1996) and swell (20-21 October), but virtually no suspension during the fairweather condition (10-20 October). Bottom accreted about 20 cm during the storm.

was significantly higher during the storm than it was during the swell: concentration at 2 cm ab during the storm exceeded about 1 g/l on average, while it was about 0.5 g/l during the swell (Figure 2-7). However, the storm concentration profile exhibited a faster decay with height than the swell profile (Figure 2-7). As a result, the concentration at 30 cm ab during the swell was higher than that during the storm. Close inspection of intra-burst sediment concentration reveals that intermittent suspension of sediment is evident during the storm and swell conditions (Figure 2-8). During the storm, individual bursting events do not inject sediment as high into the water column as is evident during swell conditions. The burst-averaged concentration reflects this same pattern, with steeper concentration profiles during swell (Figure 2-7). Note that similarly steep profiles have been reported by others when waves are present in the absence of strong currents (Vincent and Osborne, 1995; Lee and Hanes, 1996). This characteristic feature will be discussed later in the paper.

Observed sediment concentrations also reflect measurement location relative to bedforms. Figure 2-9 shows concentration time-series at 5, 15 and 30 cm ab and bed elevation during storm and swell. Bed elevation change is displayed relative to that at the beginning of the experiment. Higher resuspension was generally observed above bedform crests both during the storm and swell periods. Crests are better resolved by all three ABSs simultaneously during the storm, suggesting the ripples were more sharply crested during the swell than during the storm. During most of the storm, the pattern of higher concentration above the bedform crests was no longer evident above ~20 cm ab. Similar patterns of significant phase coupling between the resuspended sediment and the bedforms in the near bed region (< 10 cm ab) and less significant coupling above that level have also been observed on a macro-tidal beach in the UK (Osborne and Vincent, 1996). In contrast, during the majority of the swell period in Figure 2-9, high concentration above bedform crests extended more than 30 cm ab. This is because, as described above, waves during the storm did not appear to eject sediment as high into the water column as they did during swell. Alternatively, one might argue that the stronger mean current during storm conditions horizontally advected the suspended sediment

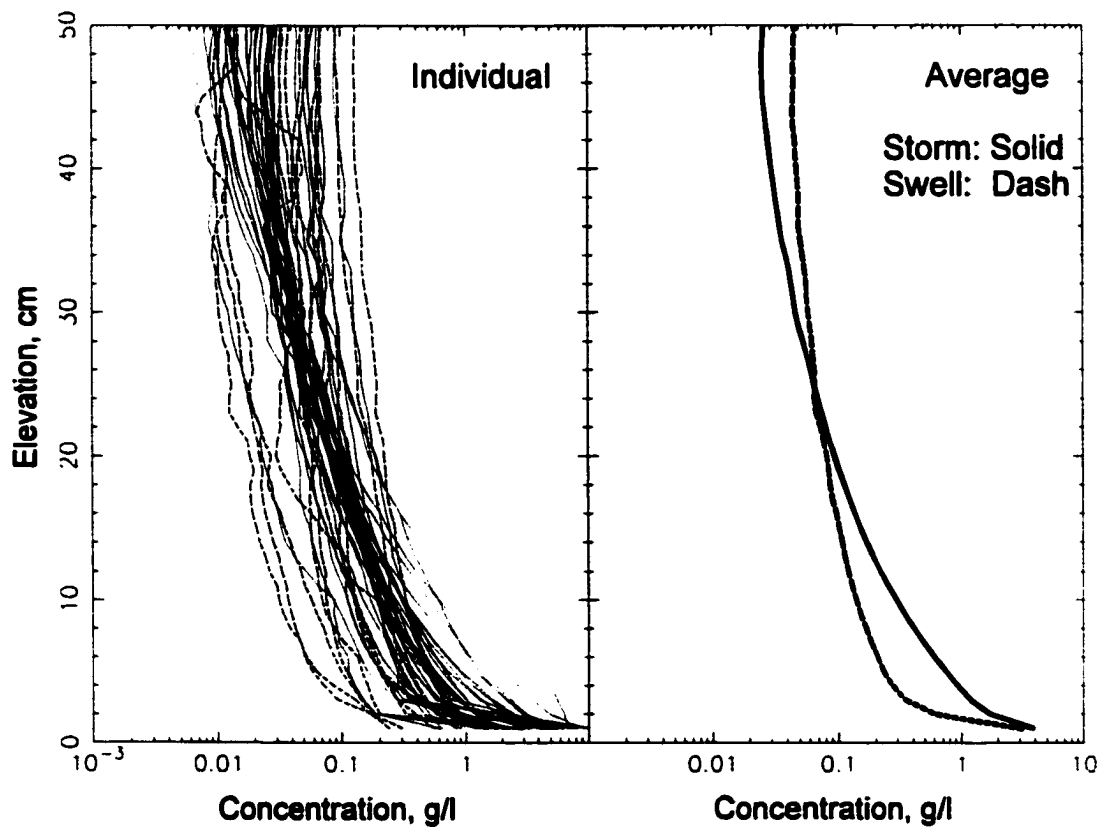


Figure 2-7. Average sediment concentration profile during the storm and swell. Near bottom sediment concentration during the storm was higher (by a factor of 2) than during the swell. However, the concentration gradient (decay rate) with elevation was greater during the storm.

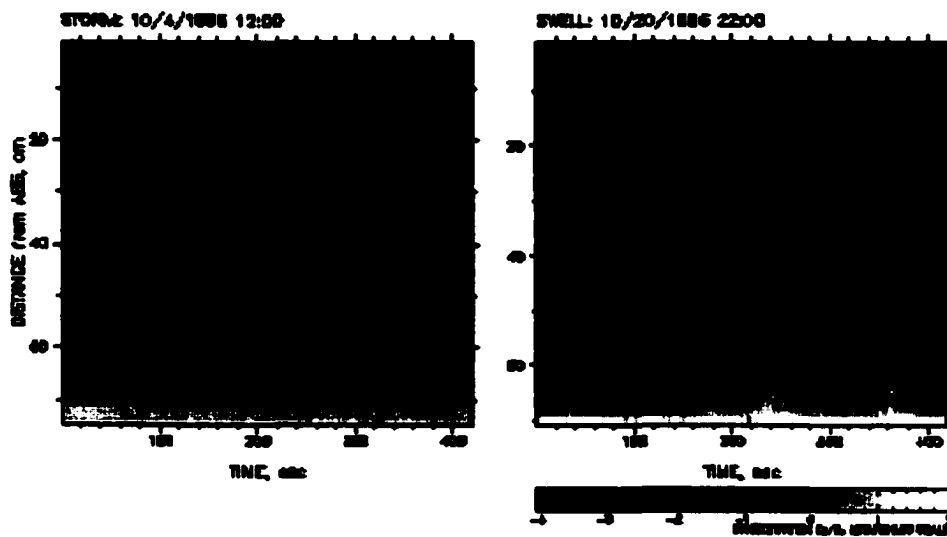


Figure 2-8. Intra-burst sediment concentration during storm and swell. Intermittent bursting and rapid decay are evident during the storm. Contrary to the storm case, bursting and sustained suspension are prevalent for the entire swell burst and responsible for steeper gradient in the higher elevation

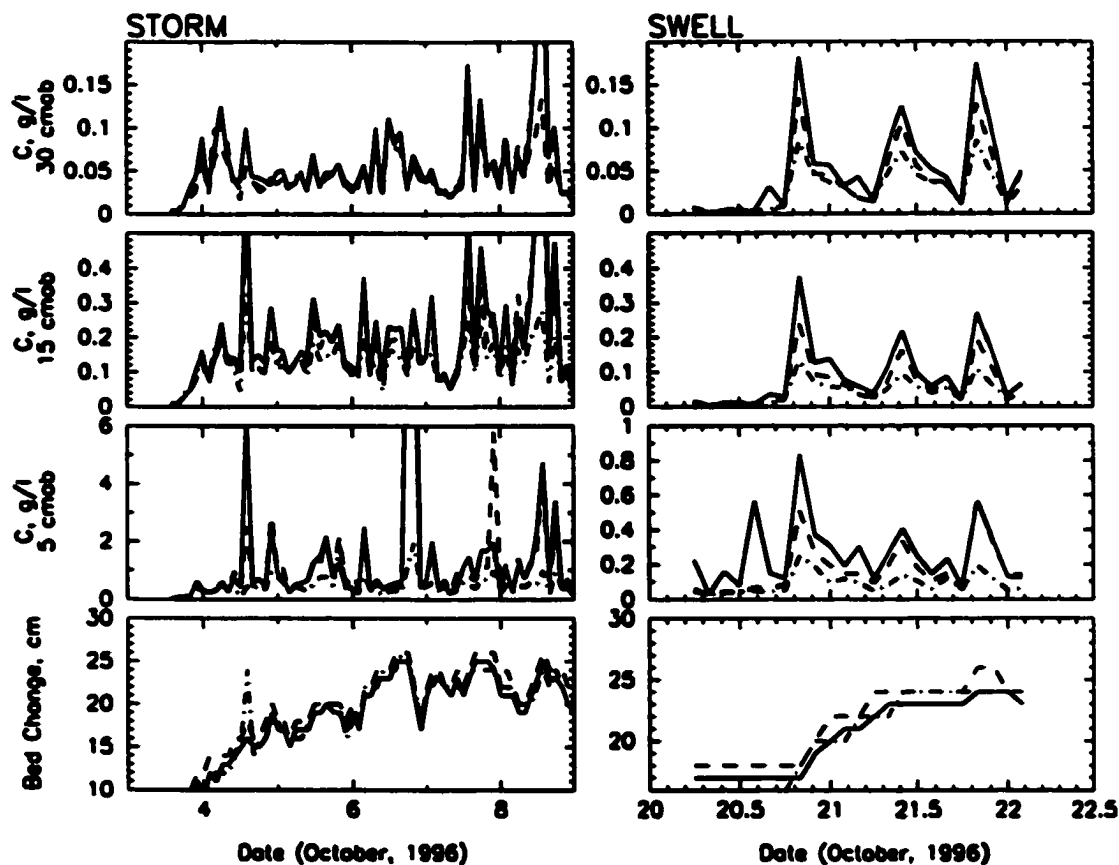


Figure 2-9. Observed sediment concentration at 5, 15 and 30 cmab and observed bed level change during storm and swell. Higher resuspension above the bedform crest is clearly seen during both storm and swell. A similar pattern of higher concentration above bedform crests continues up to about 20 cm during storm and above 30 cm during swell. Above 20 cmab during the storm, higher concentration does not necessarily corresponds to bedform location, indicating a different vertical mixing mechanism is at work. Solid line - F1; dash - F2; dot - F3.

away before it could be observed higher in the water column. But if this were the main explanation, then nearby suspension events during the storm would also have been horizontally advected into the sensor array. This does not appear to be the case for the rapid burst-averaged decay with height seen during storm conditions. Thus, these observations indicate sediment resuspension and vertical distribution of suspended sediment was controlled by the bedform presence and its relative position, in addition to the flow strength responsible for sediment suspension. Sediment concentration at higher elevations appeared to be due to different vertical mixing mechanisms operating under different conditions.

2.3. SEDIMENT EDDY VISCOSITY AND EDDY DIFFUSIVITY

In order to obtain the linearly increasing eddy viscosity profiles specified by (2-4), characteristic shear velocities must be determined. To do so here, two methods were applied: the best-fit log profile and a wave-current interaction model. The best-fit log profile method involves estimating the shear velocity from the mean current profile within the current boundary layer utilizing the law of the wall

$$u_c = (u_*c/\kappa) \ln(z/z_{oc}) \quad (2-10)$$

where u_c is the time averaged flow velocity and z_{oc} is the z intercept at which u_c becomes zero.

A second method for estimating the shear velocity is via a wave-current interaction model. Wave-current interaction models are usually used to predict u_*c and z_{oc} , apparent roughness, values defining the current profile above the wave boundary layer, from knowledge of current at a point, near-bottom wave orbital velocity and physical bottom roughness characteristics. The Grant-Madsen-Glenn (hereafter GMG; Grant and Madsen, 1986; Glenn and Grant, 1987) wave-current interaction model was applied because this model uses a strictly linear eddy viscosity model. In addition, it is relatively simple and has been widely applied in the literature. This model also provides the shear velocity due to waves and the shear velocity due to the combined effect of

waves and current in the wave boundary layer (Grant and Madsen, 1986). Other models use slightly more complicated, continuous profiles for viscosity (e.g., Smith, 1977; Madsen and Wikramanayake, 1991). Viscosity within these other models is asymptotic to (2-4) within portions of the wave and current boundary layer. The ultimate result for predicted sediment concentration is not sensitive to the difference in these authors' viscosity formulation.

To apply the GMG model, total bed roughness was defined as

$$k_b' = k_b + k_{br} + k_{bm} \quad (2-11)$$

The grain roughness, k_b , is on the order of grain diameter ($2.5d_s$, where $d_s = 0.017$ cm is the mean sediment size in the bed) and the drag roughness, k_{br} , used the relationship given by Nielsen (1992) in terms of ripple geometry

$$k_{br} = 8\eta_b(\eta_b/\lambda_b) \quad (2-12)$$

where η_b is the ripple height and λ_b is the ripple length. Ripple height and length were estimated using the Wiberg and Harris (1994) ripple model. Movable bed roughness due to sediment transport, k_{bm} , was estimated by following Xu and Wright (1995)

$$k_{bm} = 5(\tau_m' - \tau_{cr})/((\rho_s - \rho)g) \quad (2-13)$$

where ρ_s and ρ are densities of the sediment and fluid and g is acceleration of gravity.

The skin friction shear stress τ_m' is defined by

$$\tau_m' = 1/2\rho f_{cw}u_b^2 \quad (2-14)$$

where f_{cw} is the skin friction factor given by Madsen and Wikramanayake (1991). The critical stress for initiation of motion is $\tau_{cr} = 0.16$ Pa for $d_s = 0.017$ cm (Dyer, 1986).

Figure 2-10 displays the predicted contributions to k_b' from the three roughness components through the storm and swell events.

Figure 2-11 shows typical eddy diffusivity and eddy viscosity profiles estimated as described above during storm and swell events. Apparent eddy diffusivity profiles were estimated independently using each of the three ABS channels by

$$\epsilon_s = w_s \bar{c} / (\partial \bar{c} / \partial z) \quad (2-15)$$

Under storm conditions, the vertical structure of eddy viscosity associated with the mean current was consistent with diffusivity calculated by (2-15) about 20 cm into the current

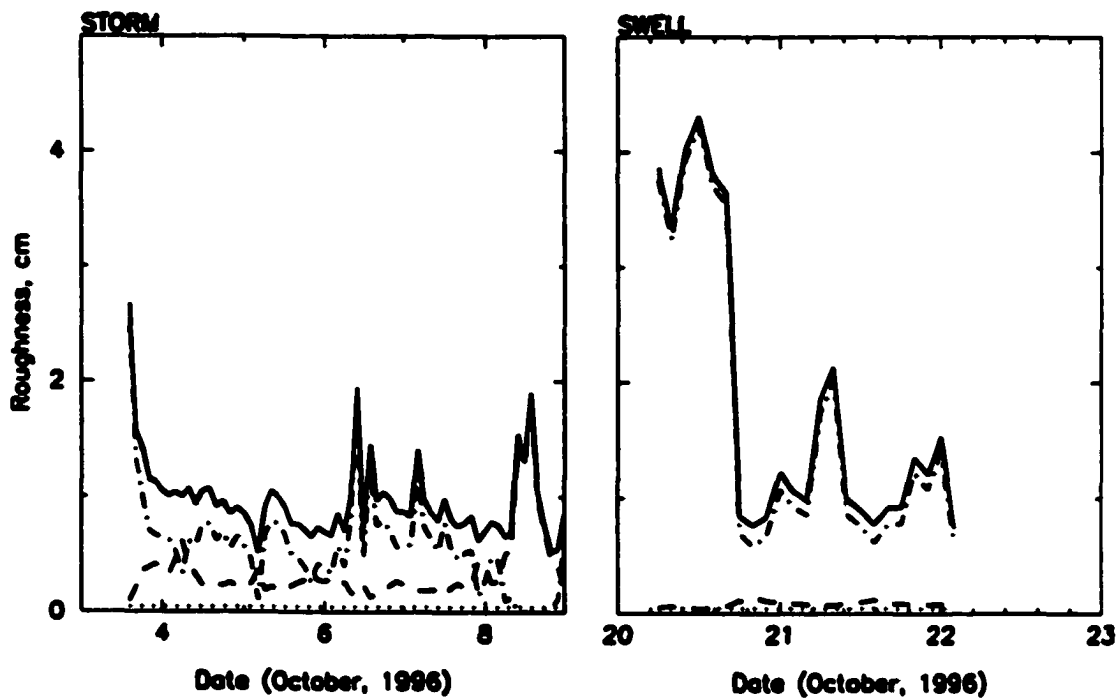


Figure 2-10. Modeled bed roughness during storm and swell. k_b - dot; k_{br} - dash-dot; k_{bm} - dash; k_b' - solid.

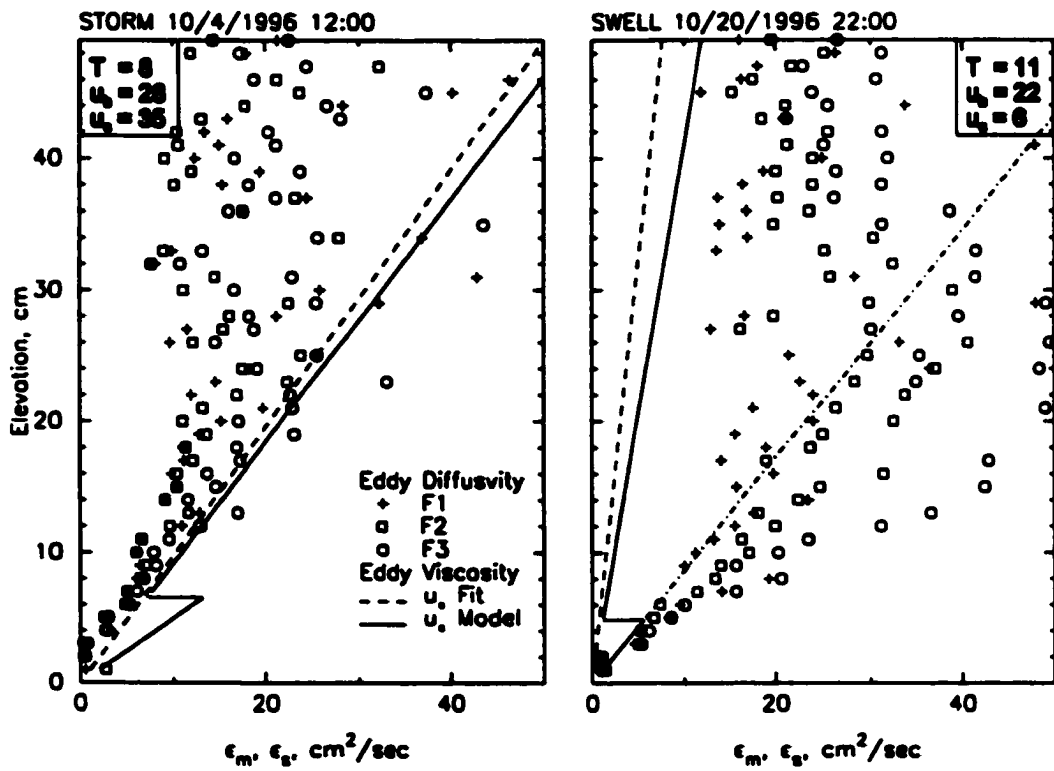


Figure 2-11. Eddy viscosity and diffusivity profiles during storm and swell conditions. Eddy viscosity using u_{cw} above the wave boundary layer is shown by a dot-dashed line for the swell case. Wave period (T), current speed at 1 mab (u_c) and near-bottom orbital velocity (u_b) are also shown in the figure.

boundary layer. Above the linear region, the diffusivity profile exhibited a less consistent structure. Nonetheless, ϵ_m associated with u_{*c} still provided an upper bound on observed ϵ_s . Note that eddy viscosity profiles estimated by a log linear fit and predicted by the GMG agree well. Under swell, the vertical structure of ϵ_s was consistent with ϵ_m within the wave boundary layer. Above the wave boundary layer, ϵ_s diverged from ϵ_m associated with u_{*c} , but continued to increase as if still determined by u_{*cw} . Similar to the storm diffusivity profile, the swell diffusivity profile exhibited a less coherent structure above ~20 cm ab.

Figure 2-12 displays time-series of shear velocities during storm and swell. u_{*zs} was inferred via a least-square fit to the linearly increasing eddy diffusivity profiles of ABS F2 using (2-3) with $w_s = 1.8$ cm/sec (Dietrichs, 1982). The maximum height of the linearly increasing eddy diffusivity for purposes of curve-fitting was determined by two criteria. Either the gradient determining eddy diffusivity was greater than 10 cm²/s or there were more than two consecutive gradients with negative values. It is noted that we also attempted to obtain u_{*cws} based on the eddy diffusivity profile below the WBL thickness as predicted by the GMG model. However, the estimates were unreliable due to high scatter and too few data points. As described above, u_{*zs} agreed well with u_{*cw} during swell and with u_{*c} most of time during the storm. It is noted, however, that u_{*zs} also followed a projection of u_{*cw} above the boundary layer during swell and during several “storm” bursts on October 6.

2.4. DIFFUSION-DOMINATED VERTICAL DISTRIBUTION OF SUSPENDED SEDIMENT

In this section, the two layered Rouse-type model of Glenn and Grant (1987) for suspended sediment distribution is applied to the above storm and swell dominated observations. The two-layered Rouse-type model is obtained by integration of (2-3) using (2-4) below and above the WBL, neglecting sediment induced stratification;

$$C_{zi} = C_{ri}(z/z_o)^{-w_s/ku_{*cw}} \quad z \leq \delta_w \quad (2-16a)$$

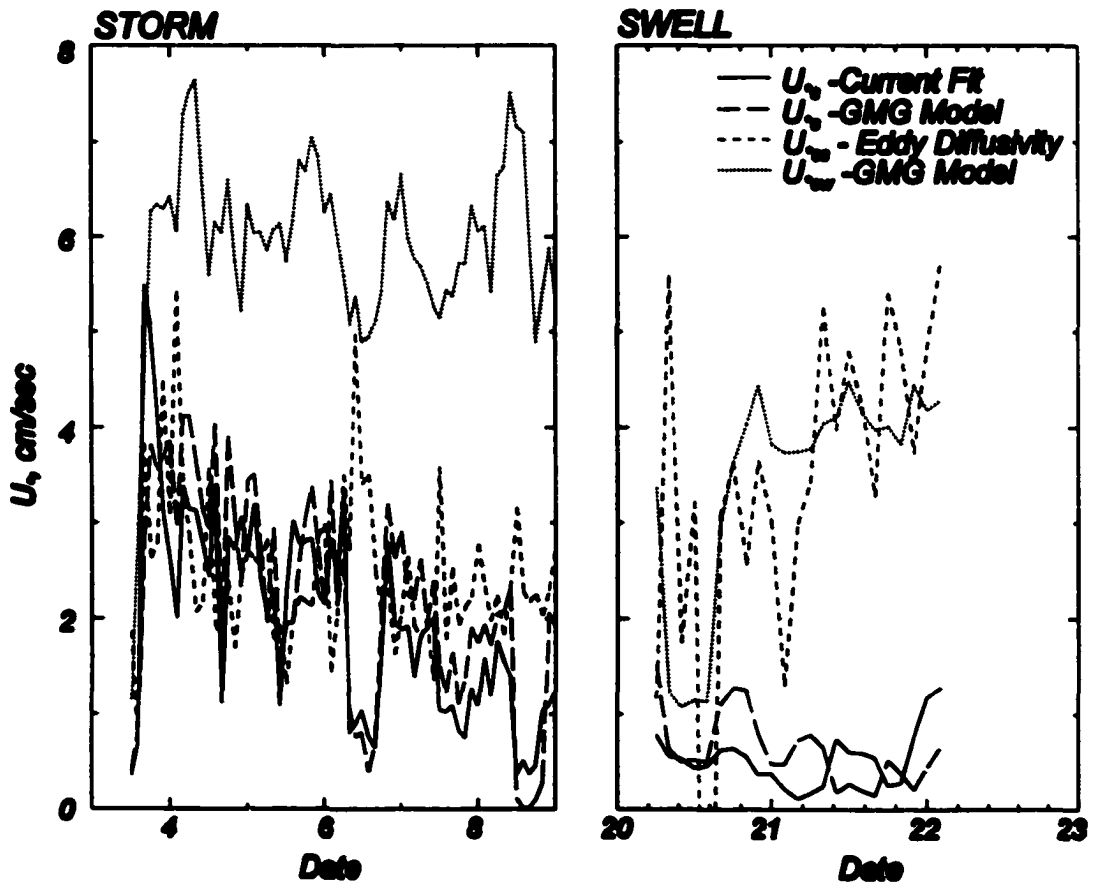


Figure 2-12. Time-series of shear velocities during storm and swell.

$$C_{zi} = C_{ri}(\delta_w/z_r)^{-w_i/\kappa u_*} (z/\delta_w)^{-w_i/\kappa u_*} \quad z > \delta_w \quad (2-16b)$$

where C_z and C_n are the concentrations at a height, z , and at a reference height, z_r , respectively and the subscript i indicates the i th size class. The reference concentrations are given as;

$$C_{ri} = \gamma_o C_{bi} \left(\frac{\tau'_m - \tau_{cri}}{\tau_{cri}} \right) \quad (2-17)$$

where γ_o is the resuspension coefficient which is set to 0.0002, C_{bi} are the volume concentrations in the bed sediment, and τ_{cri} are the critical shear stresses for initiation of motion.

Seven grain sizes, shown in Table 1, were used to reproduce the distribution observed in the bed. In addition, a mixing depth was incorporated into the model, following Wiberg et al. (1994) such that

$$\delta_m = q_{bl} T / (C_b \lambda_b) + \delta_b \quad (2-18)$$

where δ_m is mixing depth, q_{bl} is bedload transport rate and T is wave period. δ_b represents a background mixing depth, set to 1 mm. This is useful when flow conditions are so weak that there is no bed load transport, but fine sediment can be removed from the mixed sediment. The bedload transport rate was estimated from the Meyer-Peter and Müller (1948) equation, $q_{bl} = 8(\tau'_m - \tau_{cr})^{1.5} / (\rho_s - \rho)g$. Bed armoring was incorporated into the model following Wiberg et al. (1994). Total suspended sediment, predicted by (2-16) for each size fraction, was integrated from the bed to half the water depth and was compared to the available sediment for each fraction above the mixing depth. If the total suspension of a fraction exceeded the available sediment in the bed down to δ_m , the reference concentration for that fraction was reduced until the total suspended sediment of that size no longer exceeded the amount available.

Figure 2-13 shows the vertical distribution of suspended sediment from the bed level to 50 cm above the bottom during storm and swell conditions. The example bursts are the same as those used in Figure 2-11. The two-layered Rouse-type model

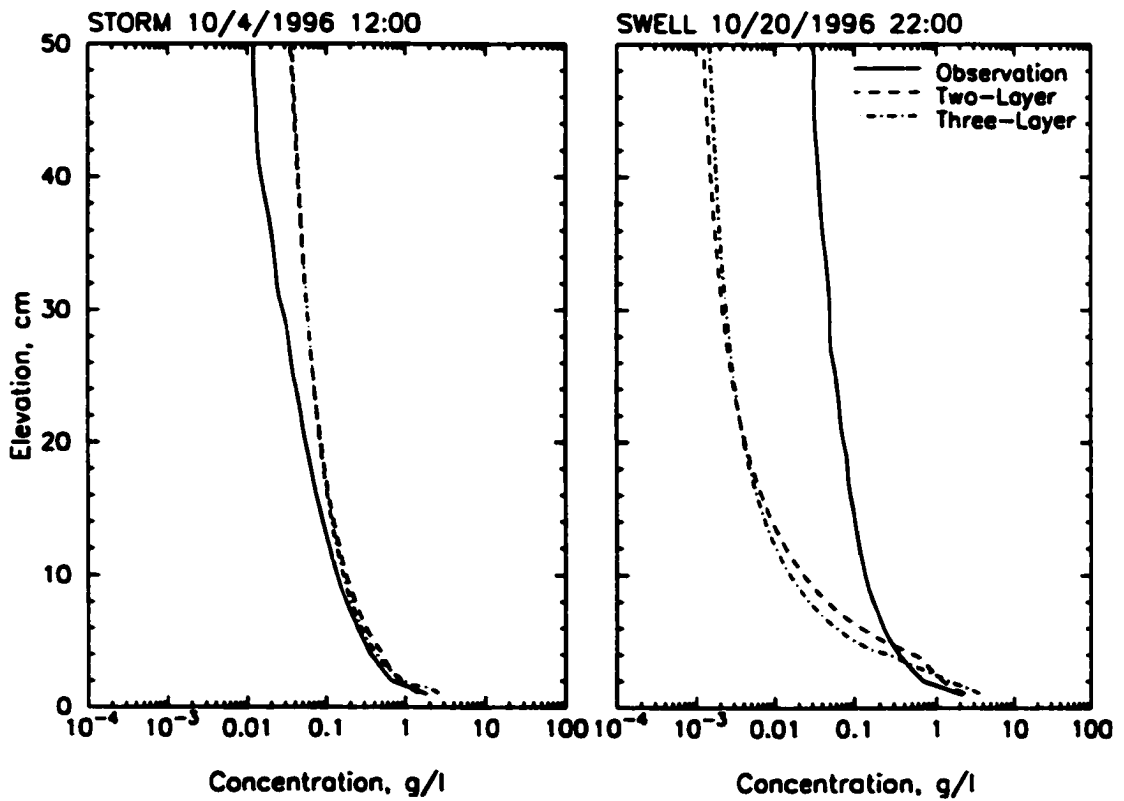


Figure 2-13. Observed (F2) and modeled sediment concentration during storm and swell. Two-layered (Grant and Glenn, 1987) and three-layered (Madsen and Wikramanayake, 1991) Rouse equations were used to model

reproduced the storm data quite well, while it considerably underestimated concentration above the wave boundary layer during swell conditions. This is consistent with the results for apparent eddy diffusivity: the GMG model reproduced ϵ_s above the WBL well during the storm, whereas the model significantly underestimated ϵ_s as derived from (2-15) during swell. Also shown in Figure 2-13 are the results for a three-layer Rouse-type model which incorporates the intermediate constant viscosity layer of Madsen and Wikramanayake (1991). The intermediate layer allows the viscosity profile to remain continuous, which is important for implementation of Nielsen's (1992) advection component later in this paper. As shown in Figure 2-13, the time-averaged concentration profile predicted by diffusion alone is insensitive to this modification. In contrast, it is noted that multiple grain size in combination with bed armoring (Wiberg et al., 1994) greatly improved the model results during storm conditions relative to the results for a single grain size without armoring.

Figure 2-14 displays time series of observed and modeled sediment concentrations at 5 and 30 cm above the bed during storm and swell conditions. The bursts for which the Rouse-type model failed to reproduce the observations above the wave boundary layer are shaded, signifying that the assumption of equality between model predicted eddy viscosity and observed apparent eddy diffusivity was invalid. These periods when u_{*cs} follows u_{*cw} included most of the swell cases as well as several bursts during the storm on October 6. The physical mechanisms associated with these two distinct suspension modes are discussed in the following section.

2.5. CRITERIA FOR DIFFUSION VERSUS ADVECTION DOMINATED SEDIMENT SUSPENSION

In the previous section, we showed that the assumption of (2-4), equality of observed ϵ_m and modeled ϵ_s , was valid during most of the storm event, but was invalid during swell and during a few storm bursts. In order to further examine under what conditions the assumption of (2-4) was invalid, we introduce a scaling parameter, R ,

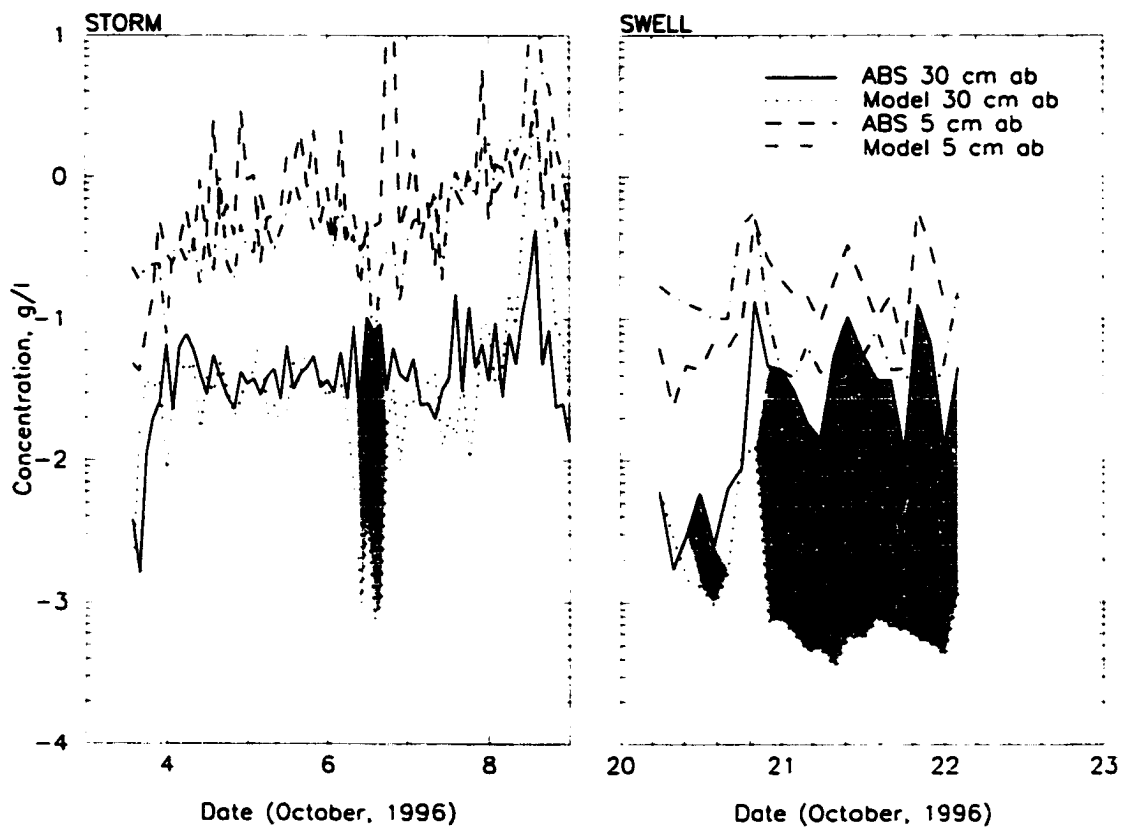


Figure 2-14. Time-series of observed and modeled concentration at 5 and 30 cm ab during storm and swell conditions. Shading indicates times when the assumption of (3) is invalid.

which is the ratio of the vertical advection velocity relative to the mean current, $u_{c,s}$ at the top of the GMG wave boundary layer. Here, the vertical advection or “jet” velocity, u_j , is scaled to $(\eta_b/\lambda_b)u_b$ where η_b and λ_b are the modeled ripple height and ripple length, respectively, and u_b is the maximum near-bottom orbital velocity. Andreopoulos and Rodi (1984) performed laboratory experiments on nearbed jets impinging on a mean current. They found that at small ratios of jet-to-crossflow velocity ($R < \sim 0.5$), the jet was immediately bent over by the crossflow, while at higher R-values ($R > \sim 0.5$) the jet penetrated further into the crossflow. The results of Andreopoulos and Rodi can be applied to vortex shedding by waves over ripples under a mean current. Following their argument, at small R-values, turbulent diffusion by mean current shear outside the classical wave boundary layer should be the dominant process of vertical mixing because the current itself will block the “jets” associated with ripple vortex shedding. For cases of higher R-value, the current will no longer block the vortices and suspension above the classical WBL should be supported by vertical advection associated with vortex shedding.

Figure 2-15(a) displays a time-series of the scaling parameter, R. In addition, wave orbital velocity and current velocity are shown in Figure 2-15(b). Figure 2-15(c) displays u_{cw} , u_c and $u_{cr} = w_s$ for the mean sediment size. As predicted, periods with $R > 0.5$ generally correspond to times when the assumption of (2-4) failed (See Figure 2-14). This pattern is consistent with the observations of jet penetration by Andreopoulos and Rodi (1984). The periods of higher R-values ($R > 0.5$) correspond to weak currents (crossflow less than 10 cm/sec), and waves strong enough to suspend sediment from the bed (Figure 2-15b). Interestingly, when R was greater than 0.5, u_c was usually smaller than the fall velocity of the sediment (Figure 2-15c). The weak currents enabled the shedding vortices to penetrate further above the predicted wave boundary layer while turbulence associated with the mean current was simultaneously too weak to maintain sediment in suspension. Smaller values of $R < 0.5$ corresponded to strong current conditions when the associated shear was greater than w_s . Thus, the dominant process for $R < 0.5$ was sediment diffusion associated with current generated turbulence outside

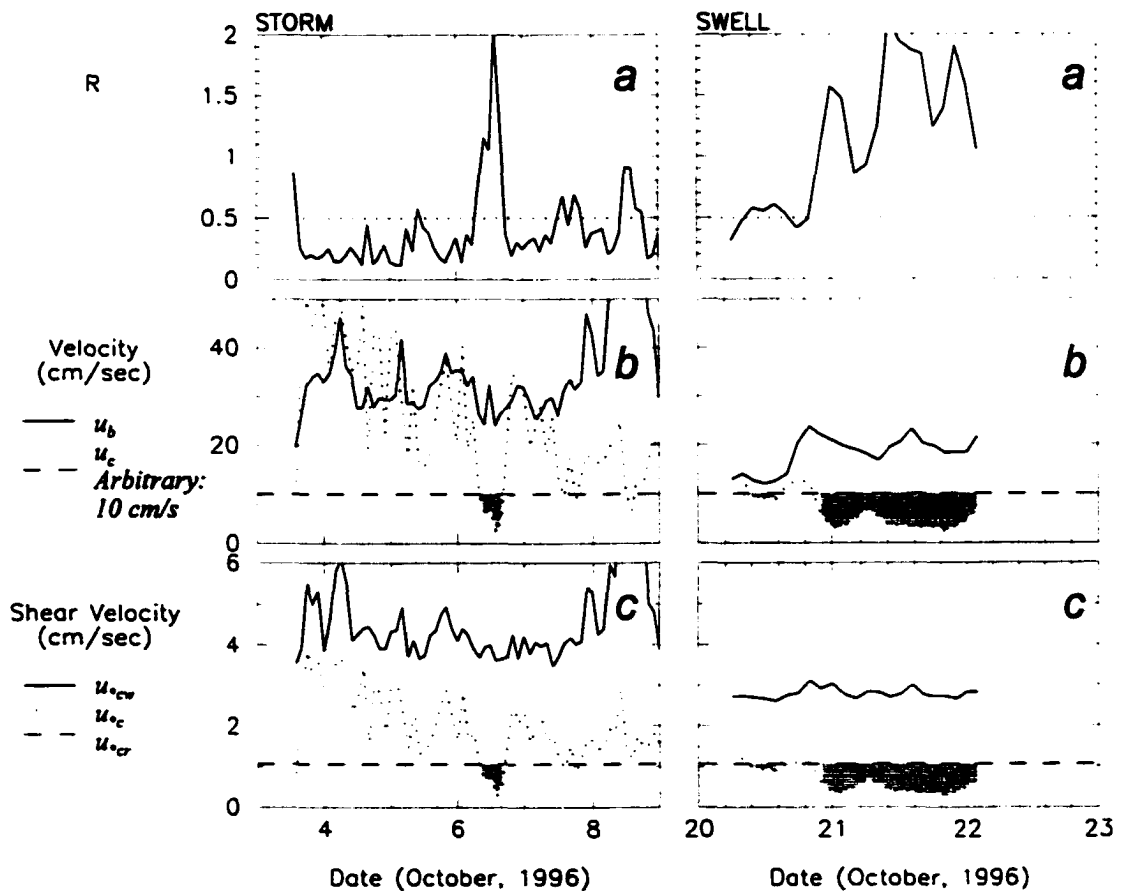


Figure 2-15. a) Time-series of scaling parameter, R , which is a ratio of the vertical advection velocity to the mean current, $u_{c,\delta}$ at the top of the wave boundary layer during storm and swell conditions. The vertical advection velocity, u_v , is scaled to $(\eta/\lambda)u_b$ where η and λ are the ripple height and ripple length, respectively, and u_b is the maximum near-bottom orbital velocity; b) Current velocity and near-bottom wave orbital velocity. Arbitrary line is set to delineate weak current condition.; c) Time-series of shear velocities of u_{*c} , u_{*cw} and u_{*cr} for the mean sediment size

the wave boundary layer. Somewhat paradoxically, the strong current actually reduced mean sediment concentration 30-40 cm ab relative to swell conditions by blocking the sediment-laden jet penetration.

2.6. COMBINED DIFFUSION AND ADVECTION MODEL OF VERTICAL DISTRIBUTION OF SUSPENDED SEDIMENT

In the previous section, a diffusion-based model was used to solve (2-3) for the time-averaged suspended sediment distribution. The diffusion-gravitational settling balance appeared to be a good approximation close to the bed during the storm when turbulent diffusion associated with a strong mean current was a dominant process. However, this balance as formulated by the GMG model did not appear to hold when the current was weak but wave energy was still strong enough to suspend sediment from the bed. In this section, we apply Nielsen's (1992) combined diffusion and advection model (2-7). The integration of (2-7) with (2-6), (2-8) and $P = w_s C_n$ yields

$$C_{zi} = C_{ri} e^{-w_{si}z/\epsilon_s} \left(\frac{w_{si}}{\epsilon_s} \int_0^z \frac{e^{w_{si}z'/\epsilon_s}}{(1 + 11z'(k_b' A_b)^{-1/2})^2} dz' + 1 \right) \quad (2-19)$$

C_{ri} was determined by (2-17) along with armoring effects as described in the previous section.

Suspended sediment concentrations predicted by the combined diffusion and advection model are shown in Figure 2-16, along with the observed concentrations and the predicted concentrations using the two-layered Rouse-type model. Although the combined model reproduced the swell data better than the Rouse-type model, it still underestimated the observed concentrations. Furthermore, it significantly underpredicted the storm data. This appears to result from the adoption of the constant eddy diffusivity. Eddy diffusivity estimated by (2-8) gave small values throughout the water column, $O(1 \text{ cm}^2/\text{sec})$. This may be a reasonable estimation very near the bed, but effective ϵ_s was observed to be an order of magnitude larger 10-20 cm ab (See Figure 2-11).

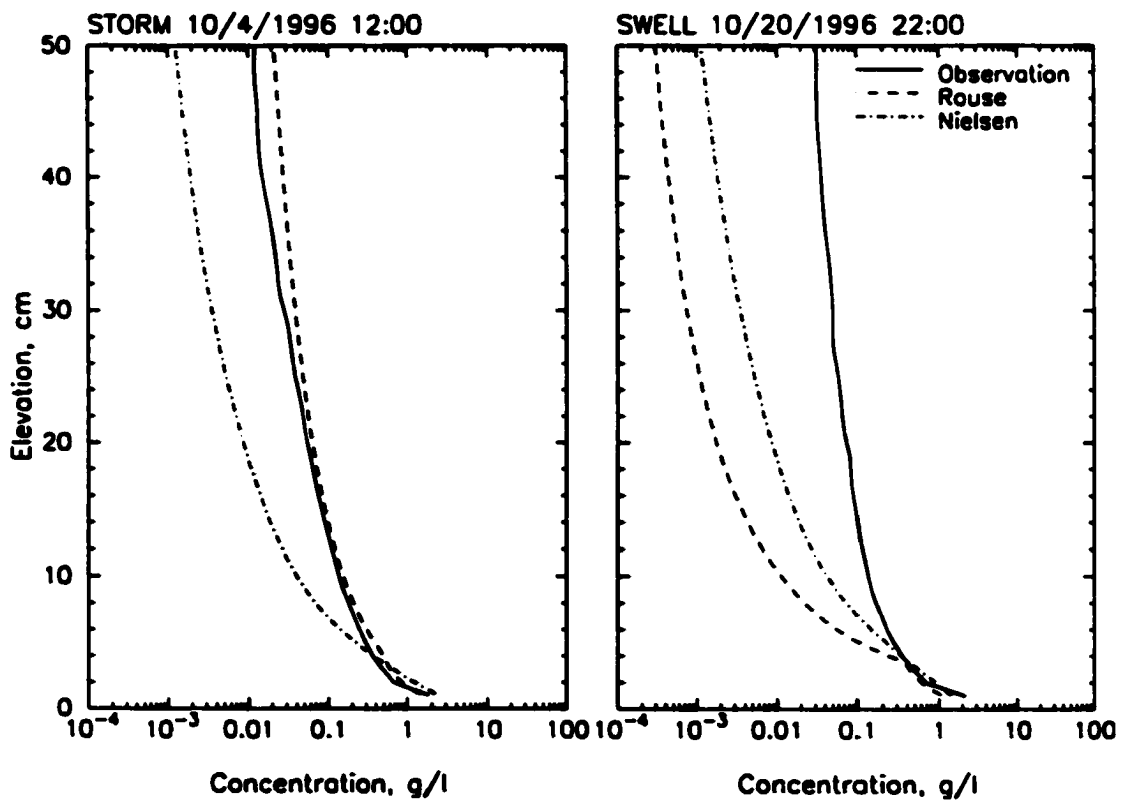


Figure 2-16. Sediment concentration profiles during storm and swell. Combined diffusion and advection model of Nielsen (1992) is compared with the

In the previous section, it was observed that effective eddy diffusivity increased linearly in the near bottom region not only during the storm, but also during swell conditions. Thus, it is appropriate to examine Nielsen's combined diffusion and advection model using a linearly increasing eddy diffusivity. Nielsen's approach requires viscosity to be continuous. Otherwise the concentration profile is not continuous at the top of the WBL. Since the two-layered eddy viscosity model is discontinuous, the modified three-layered eddy viscosity model of Madsen and Wikramanayake (1991) (GMGW model) is adopted. The profile of eddy diffusivity is expressed by the following equation:

$$\varepsilon_m = \varepsilon_s = \kappa u_{*cw} z, \quad 0 \leq z \leq \delta_w \quad (2-20a)$$

$$\kappa u_{*cw} \delta_w, \quad \delta_w \leq z \leq \delta_w / \varepsilon_a \quad (2-20b)$$

$$\kappa u_{*c} z, \quad \delta_w / \varepsilon_a \leq z \quad (2-20c)$$

The intermediate layer, $\delta_w \leq z \leq \delta_w / \varepsilon_a$, allows a transition from the wave boundary layer to the current boundary layer. The height of this layer is scaled by $\varepsilon_a = u_{*c} / u_{*cw}$. Adopting the three-layered eddy diffusivity model, the solutions for (2-7) using (2-20) and $P = w_s C_n$ are provided by Lee and Hanes (1996). The parameters used in this model were obtained from the GMGW model and bed armoring effects with 7 grain sizes were incorporated as in the other models.

Figure 2-17 shows concentration profiles predicted by the GMGW plus advection model during storm and swell. For comparison, concentration profiles of the GMG model without advection, and the Nielsen model with constant eddy diffusivity are also displayed in the figure, along with the observed concentration profiles. The GMGW model plus advection reproduced the storm data very well and the concentration profile is almost identical to the GMG model without advection. During the weak current condition, the GMG plus advection prediction was relatively close to the prediction of Nielsen's combined diffusion and advection model. Thus, GMGW plus advection performed better than the diffusion equation during swell, and better than Nielsen's combined diffusion and advection model during the storm. These results indicate that the constant eddy viscosity model was unrealistic for modeling sediment concentration

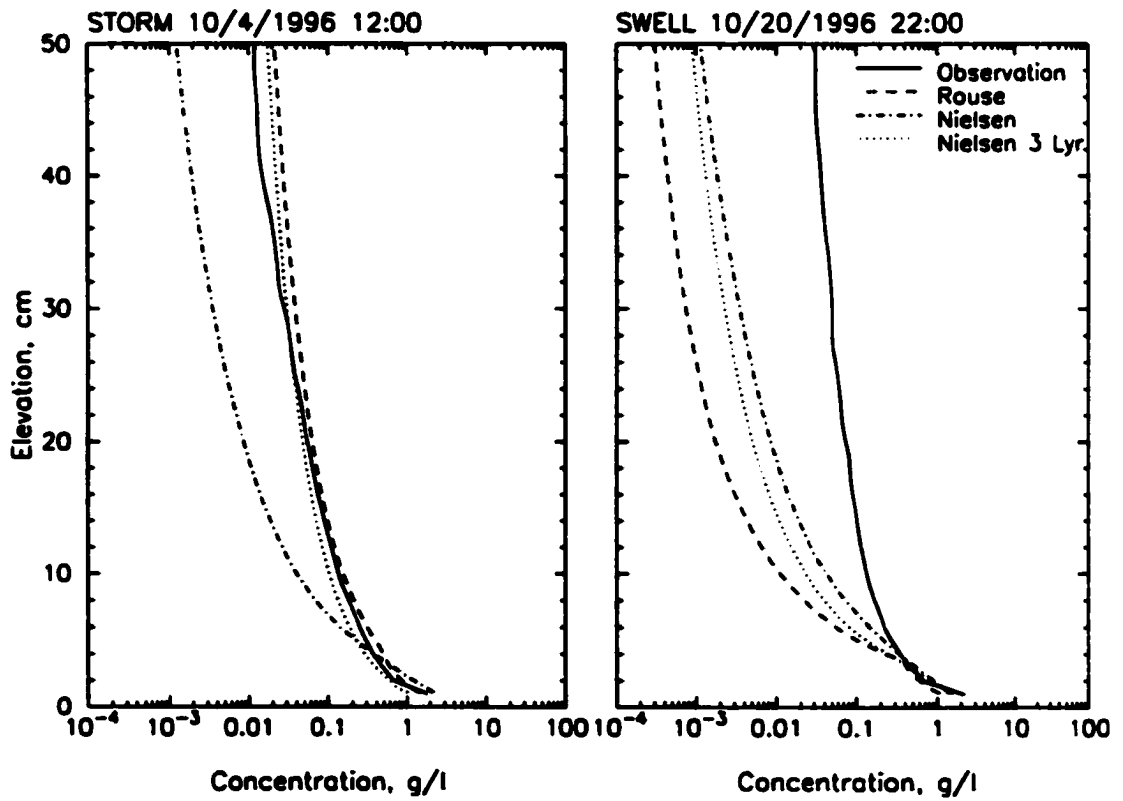


Figure 2-17. Sediment concentration profiles modeled by using three-layered combined diffusion and advection model during storm and swell are compared with those of the observed, two-layered Rouse and Nielsen's combined and

for the field experiment considered here. The three-layered combined diffusion and advection with linearly increasing eddy diffusivity performed best among the models considered. Nonetheless, it is not entirely satisfying in that it failed to reproduce the observed steep concentration gradient above 10 cm during weak current conditions. This result is similar to the findings of Lee and Hanes (1996).

2.7. DISCUSSION AND CONCLUSIONS

Observations of sediment concentration exhibited two distinctive patterns: high near-bed concentration which decreased rapidly with height above the bed during the storm versus lower near-bed concentration which decreased much more slowly with height during swell. Perturbations in near-bed concentration associated with bed form crests also dissipated more rapidly with elevation during the storm relative to swell. And patterns of intermittent suspension during storm versus swell showed similarly disparate rates of decay in concentration with height. The analysis was focused on evaluating the significance of the various mixing processes that possibly produce the observed patterns, and the conditions under which each process dominates. Two dominant mixing processes, diffusion and advection, were evaluated by examining sediment suspension models. In addition, the assumption of equality between eddy viscosity and eddy diffusivity was examined.

Eddy diffusivity was inferred from the observed concentrations. The results showed that there was a near-bottom region over which eddy diffusivity increases linearly during both storm and swell conditions (Figure 2-11). Assuming a diffusive balance, shear velocity inferred from the linearly increasing eddy diffusivity profiles agreed well with u_{*c} during the storm and with u_{*cw} during swell (Figure 2-11). The conditions for which ϵ_s above the classical wave boundary layer were associated with u_{*c} or u_{*cw} were delineated by the scaling parameter, R , which is the ratio of jet velocity associated with vortex shedding off bed roughness elements relative to the crossflow velocity associated with the mean current. The period that u_{*cs} agreed with u_{*c} corresponded to the period of

low R-values ($R < 0.5$) and strong currents. Higher R-values ($R > 0.5$) and weak currents corresponded to the period of $u_{cs} = u_{cw}$. It is suggested that a strong current (low R) block vortices shed by waves over ripples from extending beyond the predicted WBL. In the absence of a strong mean current (high R), sediment-laden vortices are injected well above the classical WBL, steepening the mean concentration profile.

Three sediment suspension models were examined: the two-layered GMG Rouse-type model, Nielsen's combined diffusion and advection model with constant eddy diffusivity, and the three-layered GMGW model plus vertical advection. During strong current conditions when turbulent diffusion associated with the mean current is a dominant process, the GMG/W model with or without advection reproduced the observed concentration well. It is noted that bed armoring with graded sediment sizes is important for correctly predicting the concentration under these conditions. The combined model with constant eddy diffusivity resulted in underprediction. This is because the constant eddy diffusivity, $O(1 \text{ cm}^2/\text{sec})$, although reasonable very close to the bed, is inadequate more than a few centimeters into the water column. During weak currents in the presence of strong waves, all of the models failed to reproduce the observed concentrations.

Observations and modeling both reinforce the conclusion that turbulent diffusion associated with current shear above the wave boundary layer is the dominant process for sediment suspension during strong current conditions. An interesting finding is that ϵ_s , associated with u_{cw} may extend well above the predicted wave boundary layer during weak current conditions. One possible explanation is that turbulent-like mixing above the classical wave boundary layer under weak currents is driven by the fluid advected up from the wave boundary layer. For example, Sleath (1990) reasoned that even though vortex shedding is clearly different from turbulence, shedding of vortices produces a vertical exchange which has a net effect similar to that of turbulence. If organized vortex shedding has turbulent properties when averaged at large enough scale, then it is possible that an effective eddy viscosity can still be usefully applied to model both mass and momentum exchange by ripple induced vortices. In some respect, application of an "effective" $\epsilon_s = \epsilon_m$ is physically more attractive than adding a term for advection of mass

alone because the latter neglects the associated transfer of momentum. Figure 2-18 shows the observed and predicted concentrations of the two-layered Rouse-type model during swell conditions using an effective diffusivity associated with u_{*cw} up to a height of 50 cm. The agreement between them is quite good. Figure 2-19 shows the time-series of observed and predicted concentrations during storm and swell with the effective WBL thickness set to 50 cm for cases with $R < 0.5$. The plot shows the improved prediction at 30 cm ab during the weak current conditions (compare the plot to Figure 2-14). During swell conditions, the predictions still do not mimic the observed higher (and lower) concentrations above the ripple crest (and trough), but result in somewhat average concentrations over the period of swell as a whole. This indicates that the estimation of shear stresses by the wave and current interaction model and the concentrations predicted by the Rouse-type equation are spatial averages of heterogeneous areal features.

It is important to consider also how sensitive the predicted current profile is to changes in the “effective” viscosity profile. Figure 2-20 shows observed and modeled current velocities during the storm and swell for the lower two current meters (initially 19 and 38 cm ab). Three wave boundary layer thicknesses were used in the model: 1) the GMG prediction, 2) twice GMG and 3) the vertical length scale of coherent concentration response. Here, the vertical length scale of coherent concentration response was determined from the maximum height of the linearly increasing eddy diffusivity inferred from the concentration profiles. The error estimates between the observed velocity and the predicted velocities for the three wave boundary layer thicknesses ranged from 38 to 39 percent. However, the differences among the predicted velocities were under 2 percent. Thus the resolution of current shear provided by the current meters was too low to distinguish between the various choices of WBL thickness. In other words, thickening the effective WBL during periods of low current made relatively little difference to the current profile and was no more inconsistent with the observed currents than application of a thinner WBL.

Most boundary layer wave and current interaction models do not consider the effect of shedding vortices and the resulting enhanced vertical exchange above the wave

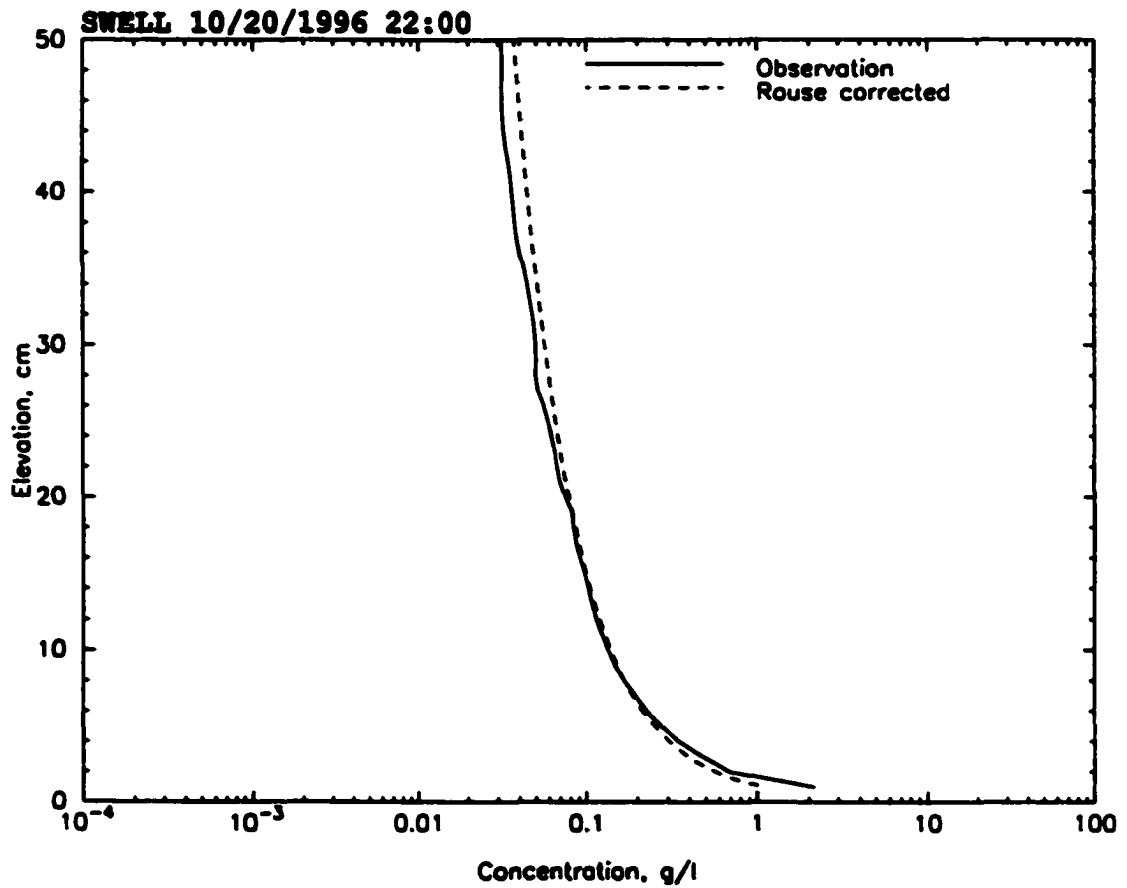


Figure 2-18. Sediment concentration profiles for a weak current condition. u_{*cw} was used above the wave boundary layer in the two-layered Rouse model.

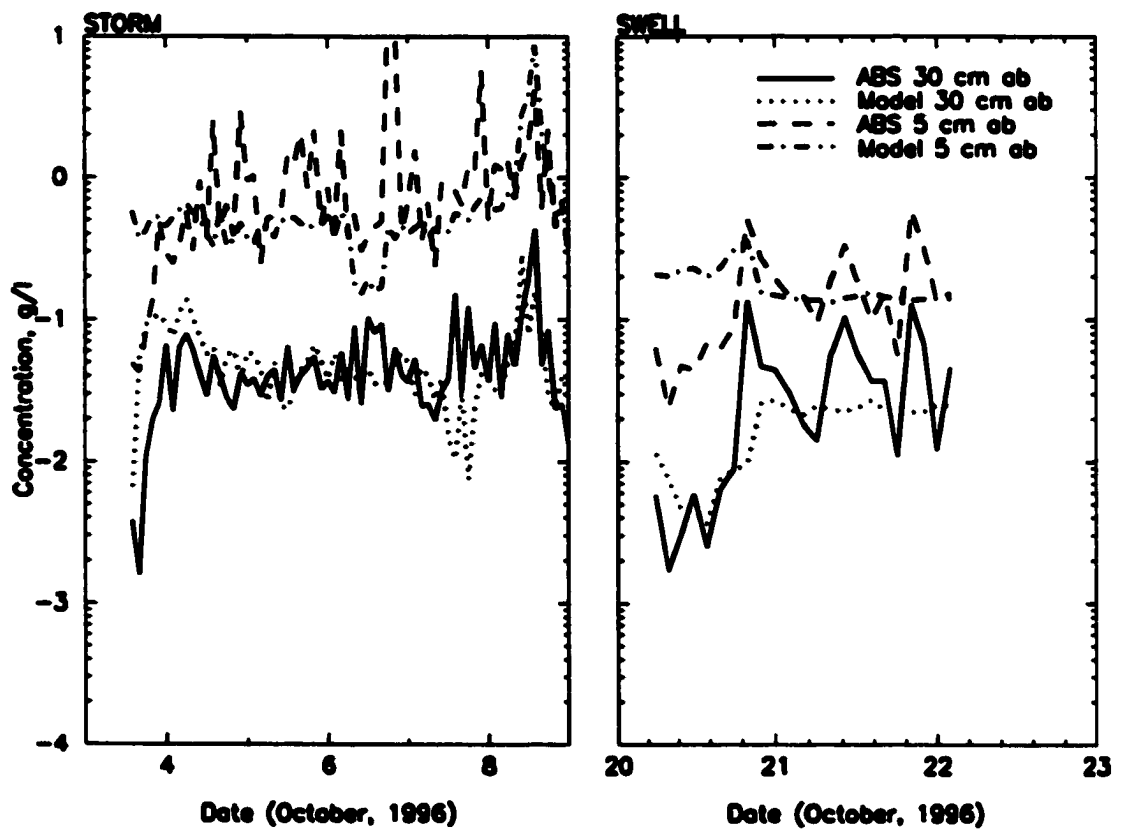


Figure 2-19. Time-series of sediment concentration during storm and swell. u_{cw} was

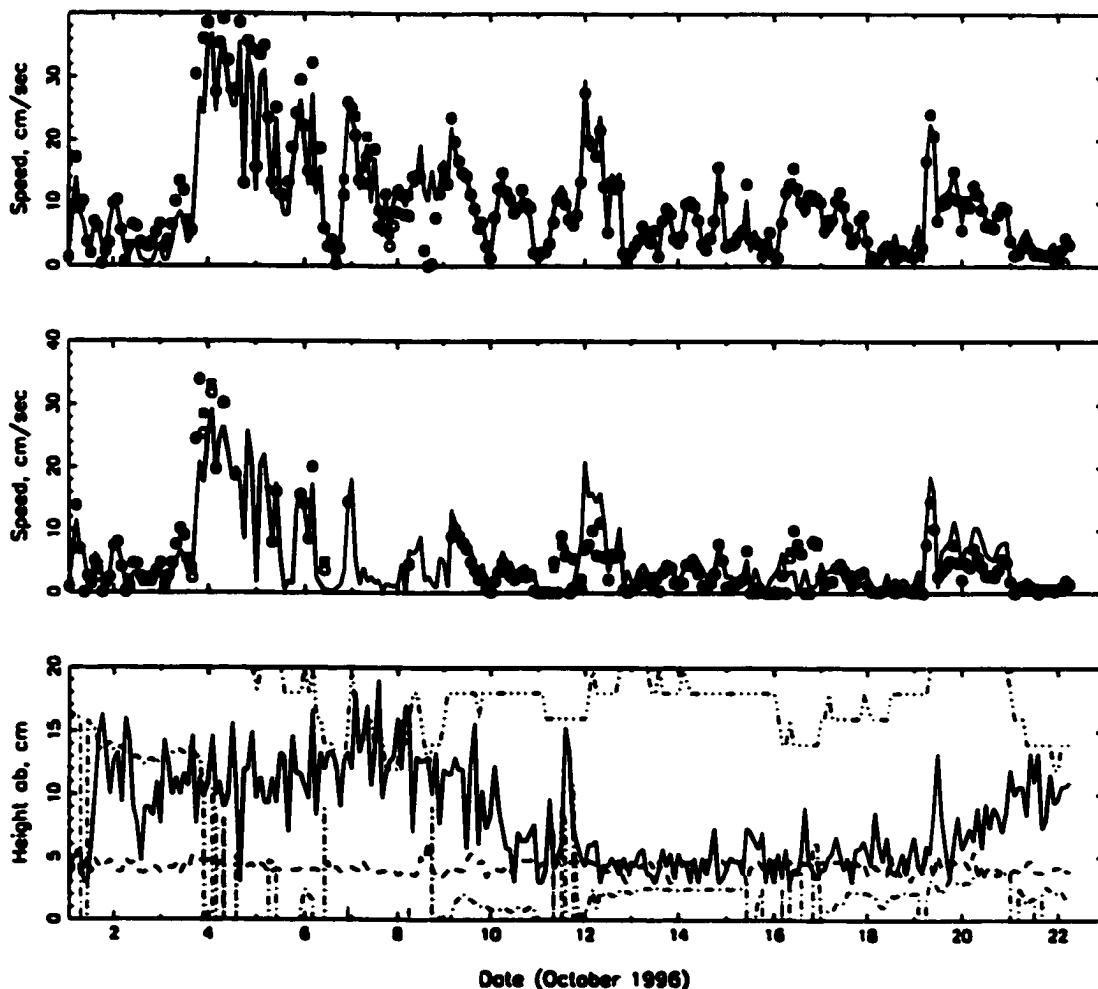


Figure 2-20. a) Observed (solid line) and predicted current velocities through time of EMCM2. Prediction was made by forcing the wave boundary layer as δ_w (cross), $2\delta_w$ (square) and δ_{es} (circle) in the GMG model; b) Observed and predicted current velocities through time of ADV. The prediction scheme is the same as a); c) Height above bottom of EMCM2 and ADV, GMG wave boundary layer thickness, and top of the linearly increasing eddy diffusivity. EMCM2 - dash-dot; ADV - dash; δ_w - dot; δ_{es} - solid line.

boundary. Those that do so via an advection term do not adequately reproduce steep concentration profiles observed under weak current conditions (Lee and Hanes, 1996, This chapter). This effect still needs to be incorporated into wave and current interaction models in order to better describe vertical mixing and to predict sediment concentration more accurately. Perhaps one viable approach is use of an “effective” diffusivity which parameterizes this enhanced exchange as being similar to turbulence when averaged horizontally and temporally. Further field observations of flow structure in this region are required to examine the validity of this hypothesis, particularly with respect to its effect on mean current shear very close to the bed.

The configuration of the tripod may have affected the vertical distribution of sediment concentration. The greatest concern is that sediment plumes scoured by the pod’s legs may have advected past our instruments. During the storm when currents were strong, the direction of horizontal suspended sediment advection would have been predominantly south, in which case the disturbance from pod to the ABS might have been minimal (see Figure 2-2). During weak current conditions, sediment movement would have been predominantly on/offshore aligned with the shore normal wave direction. Thus disturbance associated with the offshore leg might have been significant at the center post. This effect might have been exaggerated during low current conditions when periodic wave motion might have advected scoured sediment respectively back and forth under the pod. This could conceivably account for a steepened concentration profile under swell conditions. An indication of severe scour nearby might be a reversed concentration profile: higher concentrations at higher height. The concentration data showed no such events, except for minor fluctuations consistent with random variations. Furthermore, it is not clear why a steepened profile associated with pod-induced scour would be fit so well by an extension of u_{*cw} beyond the WBL or why our observation of steep concentration profiles would then be so consistent with Lee and Hanes (1996). Still, the sustained suspended sediment concentration observed during weak current conditions could be supported in part by disturbance from the pod frame, in addition to the shedding of vortices associated with wave orbital movement over bedforms. It is not

certain how much disturbance by the pod has affected the distribution of suspended sediment.

III. FORMULATION AND IMPLEMENTATION OF A WIND AND WAVE FORCED CURRENT MODEL FOR SEDIMENT TRANSPORT ACROSS THE INNER SHELF

3.1. INTRODUCTION

In the surf zone, circulation is almost entirely driven by forces that result from the dissipation of breaking waves (e.g, Battjes et al., 1990). Alongshore currents and rip currents attain speeds of over 1 m/sec, and the vertically segregated offshore flow (undertow) transports sediments seaward. Most of these intense flows are confined within the surf zone, but large storm generated rip currents can extend well out onto the inner shelf (Wright, 1995).

The flow regime of the inner shelf is different from that of the surf zone in that circulation is not primarily driven by wave breaking. On the inner shelf, friction associated with wind stress is important in that surface and bottom boundary layers overlap and often occupy the entire water column (Mitchum and Clarke, 1986). Lentz et al. (1999) reported that the lowest order along-shelf momentum balance at ~13 m depth during fall on the inner shelf off Duck, NC., is typically between the surface wind stress and bottom stress, with along-shelf pressure gradients usually providing a smaller contribution. However, Lentz et al. (1999) and Rennie et al. (1999) found that along-shelf pressure gradients became important over the inner shelf off Duck during events associated with along-shore propagation of low-salinity plumes from the Chesapeake Bay. Lentz et al. (1999) found the cross-shelf momentum balance at 13 m to be between the cross-shelf pressure gradient, wave-radiation stress gradients, the Coriolis force acting on the along-shelf current, and the cross-shelf wind stress.

An important response to wind over the inner shelf is the generation of upwelling

or downwelling. When winds blow alongshore or obliquely to the shore with the coast to the right of the wind, which is the typical situation with 'northeasters' (extratropical storms) in the middle Atlantic Bight, the across-shelf component of the current driven by the wind causes a setup of water level against the coast. This results in an enhanced along-shelf current and a shore-normal pressure gradient that drive bottom currents (Wright, 1995). These mean currents have been reported to be the dominant morphodynamic component determining sediment transport across the inner shelf at Duck (e.g., Wright et al., 1991). The along-shelf response and upwelling associated with a wind blowing in the opposite direction over the inner shelf is generally weaker (Niedoroda et al., 1985).

The presence of the Chesapeake Bay plume at Duck has been documented recently by the results of the extensive National Science Foundation "Coastal Ocean Processes (CoOP)" study which took place in the summer and fall of 1994 (Rennie et al., 1999). The plume may alter otherwise wind-driven along- and across-shelf currents and create significant density stratification over the inner shelf. Within the stratified region, the surface layer is insulated from bottom effects by the diminished vertical eddy viscosity in the pycnocline (Rennie, 1998). This suggests that linearly increasing eddy viscosity in the interior of the water column may not properly represent the reduced turbulence associated with the presence of the pycnocline.

Waves generally contribute to suspending sediments off the bed on the inner shelf, but contribute only secondarily to net advection of sediments. The inner shelf is the transition zone for waves where the decreasing depths cause the form of the waves to change to more peaked crests of greater height (through shoaling), and to alter their direction of propagation toward a more shore-normal orientation (through refraction). As waves propagate across the inner shelf toward shallower water, the near-bottom wave orbital velocity becomes asymmetric with a brief, faster onshore velocity beneath the crest, and a longer, slower offshore velocity beneath the trough. This suggests that asymmetrical wave orbital velocities promote shoreward sediment transport (Niedoroda et al., 1985). Wave asymmetry can be represented by Stokes second-order wave theory.

However, Dean and Perlin (1986) indicate that Stokes second order theory is inadequate to estimate bed stress and more elaborate models must be used. Nevertheless, the second-order Stokes model is useful because it provides a simple analytical solution and insights on how orbital asymmetry affects sediment transport processes.

Another feature of gravity waves predicted by Stokes theory is a net current driven by the waves defined as boundary layer streaming (Longuet-Higgins, 1953). Progressive waves on a free surface, beneath which the flow is horizontally nonuniform, give rise to vertical velocities within the wave boundary layer. These vertical velocities, which are a consequence of the continuity condition, lead to a non-zero, cycle-averaged, shear stresses which in turn results in a weak mean current at the top of the wave boundary layer (Fresoe and Deigaard, 1992). Boundary layer streaming has been evoked as a dominant term in the onshore transport of sediment outside the surf zone (Bowen, 1980). However, Trowbridge and Madsen (1984) found that the direction and magnitude of mass transport depends critically on temporal variation of eddy viscosity. With time-variant eddy viscosity, there was a tendency for reversal in the direction of wave-averaged mass transport under long waves.

A third feature of second order theory is the generation of Stokes drift velocity. The mean Lagrangian velocity of a fluid particle induced by a linear wave is landward for two reasons. First, a fluid particle stays longer below the wave crest than below the wave trough because the fluid velocity is positive below the crest and negative below the trough. Second, because the particle is higher above the bottom under the crest, the velocity is slightly higher, resulting in a small positive contribution to the drift (Fresoe and Dieggard, 1992). A seaward Eulerian velocity is required to counteract the Lagrangian velocity and conserve mass. This wave-induced return flow, or “undertow”, has been observed to be a major cause of offshore sediment transport just outside the surf zone (Osborne and Greenwood, 1992).

To date, no analytical model of waves and currents across the inner shelf has incorporated all of the above forcing mechanisms thought to be important to across-shelf sediment transport outside the surf zone. Thus, in this study, appropriate hydrodynamic

models are investigated and then implemented to examine the wind- and wave-driven processes which drive cross-shelf sediment transport in the inner shelf. The goal is to implement the simplest models possible which adequately represent the underlying physics. Related questions of interest include whether the presence of density gradients and stratification associated with a plume fundamentally alter the way in which wind and wave forcing lead to net cross-shore sediment transport. In particular, the stratification associated with the plume may alter the nature of the eddy viscosity profile, limiting the appropriateness of bilinear eddy viscosity models recently applied to the study of sediment transport by wind-driven currents on the inner shelf of the middle Atlantic Bight (e.g., Chisholm, 1993; Kim et al., 1997).

3.2. FIELD DATA

The U.S. Army Corps of Engineers Waterways Experiment Station, Field Research Facility (FRF) is located on the Outer Banks of North Carolina (Figure 2-1). The study area has characteristics typical of the US east coast in terms of wind climate and storm exposure (Birkemeier et al., 1985). The shoreline is straight and the bottom topography is regular over the inner shelf. In examining the wind- and wave-driven processes and implementing hydrodynamic models for sediment transport in the inner shelf, inputs are wind and waves at one location, while outputs are currents.

The right-handed coordinate system is adopted in this study: the onshore-offshore component (+ offshore) was taken to be the x-axis, while the along-shore component (+ upcoast) was taken to be the y-axis. The z-axis increases upward from the sea bed, unless stated otherwise. The shoreline at Duck is oriented 20° west of true North (Figure 2-1) and directions of the wind, waves and current were referenced to the shoreline. The directions of the wind and waves indicate where they are coming from, while current direction indicates where it is flowing toward.

3.2.1. Wind

The FRF has routinely collected wind, wave and current data every 6 hours since 1981 and every 34 min since 1986 (Table 3-1). The local wind data which served as an input to model currents were provided by the FRF. Wind speed and direction are measured by the FRF at the seaward end of their research pier at an elevation of 19 m above the sea surface (Figure 3-1a). The wind shear stress τ_s can be calculated from the wind speed, u_s and wind direction, ϕ_s , such that

$$\tau_{sx} + i\tau_{sy} = \rho_a C_a |\bar{u}_s| u_s e^{i\phi_s} \quad (3-1)$$

where ρ_a is the air density and C_a is the wind drag coefficient, which can be estimated from the following equation given by Wu (1980)

$$C_a = (0.8 + 0.065 u_d) \times 10^{-3} \quad (3-2)$$

(3-2) was originally suggested for the open ocean and may be inappropriate to the inner shelf.

Using observations of tidally-averaged current profiles near the sea bed at Duck, NC., Friedrichs and Wright (1997) examined the best-fit wind drag coefficient as a function of wave properties assuming a balance between the alongshore components of bottom stress and wind stress. For cases associated with rms near-bottom orbital velocities (u_b) > 35 cm/s, the best fit wind drag coefficients was high ($C_a = 0.0052$). They attributed the high C_a to input of momentum by occasional wave breaking outside the surf zone. For cases with $u_b < 35$ cm/s, the best predictor of C_a was whether the across-component of the wind was directed offshore ($C_a = 0.004$) or onshore ($C_a = 0.001$). Offshore directed winds on the inner shelf at Duck, NC. may be associated with large C_a because intense wind turbulence associated with air flow over the barrier island may act to more effectively transfer momentum to the surface of the adjacent ocean (Friedrichs and Wright, 1997). In this study, the wind drag coefficients associated with offshore directed winds were multiplied by a factor of three, a pattern which is also consistent with direct measurements of wind-induced Reynolds stress measured on the FRF pier in October 1996 by a turbulence resolving anemometer (C. Long, personal communication). Figure 3-1b shows the resulting wind shear stress during October 1996.

Gauge Type	Gauge Number	Data Collection		Location	Gauge Depth	Water Depth
		Start	End	Cross, Along (m)	m	m
Wind	3632	820331	940401			
	3932	870911	present	580, 517	+19.50	
Wave	3111	860901	present	915, 990	7.50	7.90
Bottom Profile	62	810101	931218 [#]	0-900, 1000		0-9

+ indicates distance above the sea level.

The date indicates the last day of survey of available data. Note that beach-nearshore profile survey continued after the day up to present.

Table 3-1. Wind, wave and bottom profile data collected at the FRF

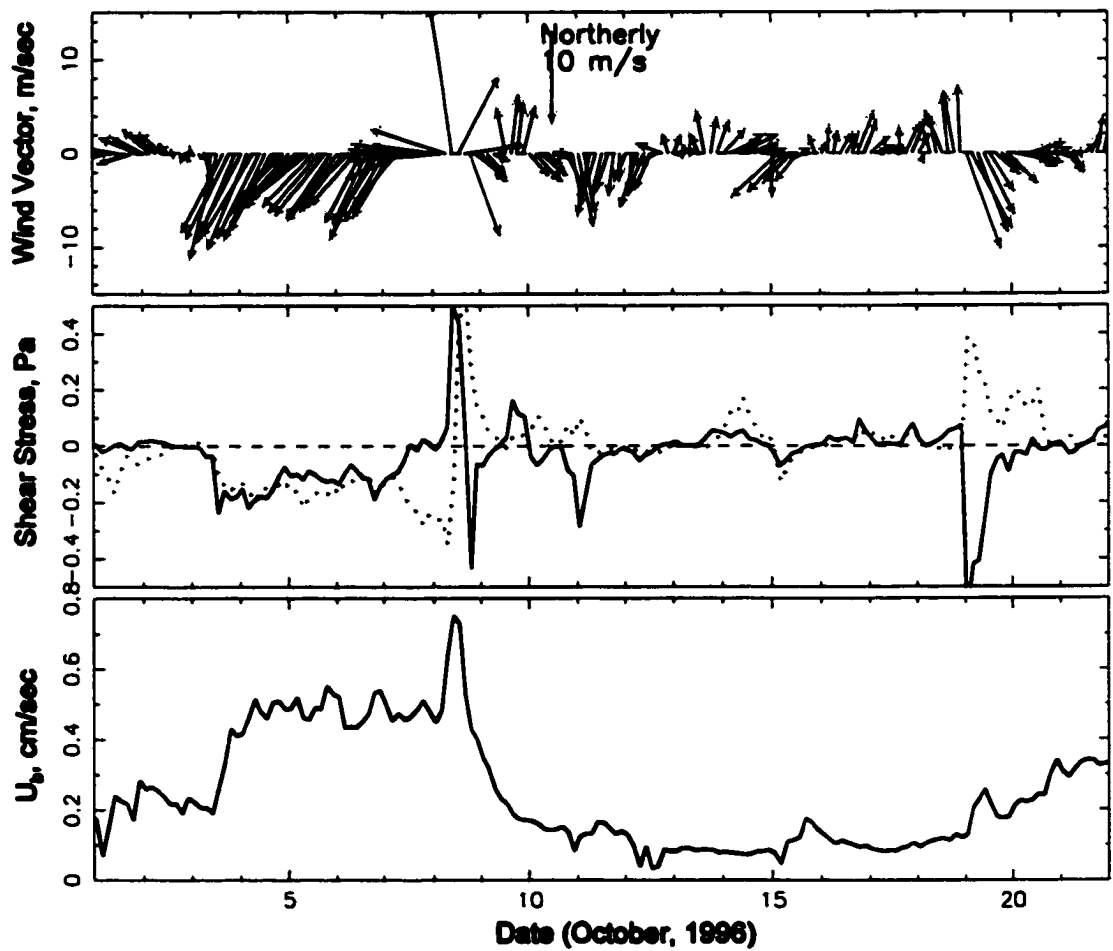


Figure 3-1. Wind velocity, surface shear stress and near-bottom wave orbital velocity during October 1996. Solid - along-shelf component of wind stress; dot - across-shelf component of wind stress.

3.2.2. Waves

Wave characteristics are measured at the FRF from three different sets of instruments. An array of fifteen pressure gauges is used to collect directional information at about 8-m depth and is called collectively gauge 3111. A Baylor staff gauge (625) and a pressure gauge (641), both attached to the pier at about 6-m depth, collect wave height and period. A Waverider buoy (gauge 630) is located at about 18-m depth. Among these three sets of instruments, wave data collected by gauge 3111 were used as input in this study because only gauge 3111 provides directional information. Reliable wave data from gauge 3111 are available beginning in 1987.

Wave height, H_{m0} , is an energy-based statistic equal to four times the standard deviation of the sea surface elevation and compensated for hydrodynamic attenuation using linear wave theory. Significant wave height, H_{m0} , was converted into rms wave height, H_{rms} , by the relationship (Dean and Dalrymple, 1992);

$$H_{m0} = \sqrt{2} H_{rms} \quad (3-3)$$

Rms near-bottom orbital velocity was calculated as

$$u_b = H_{rms} \omega / (2 \sinh(kh)) \quad (3-4)$$

where ω and k are radian frequency and wave number, respectively. Near-bottom wave orbital velocity at 8 m depth is shown in Figure 3-1c. Near-bottom wave orbital velocities observed at 13 m depth by the VIMS are described in Ch. 2.

3.2.3. Currents

Currents were measured by three types of instruments during October 1996 by VIMS: an Acoustic Doppler Profiler (ADP), an Acoustic Doppler Velocimeter (ADV) and an array of Electromagnetic Current Meters (EMCMs). One ADV and five EMCMs initially mounted at heights of 0.08, 0.19 (ADV), 0.38, 0.68, 0.98 and 1.25 m above bed (ab) on the tripod, measured boundary layer currents (Figure 2-2) and are described in Ch. 2. The 1200 kHz ADP was mounted on top of the tripod, 2.75 m ab, looking upward.

The ADP has 0.25 m bins and a 0.5 meter blanking distance from the transducer. The accuracy of EMCMs is 2-3 cm/s (Guza et al., 1988), while the accuracy of the acoustic current meters is about 1 cm/s.

On the inner shelf off Duck where the dominant current direction is shore parallel, estimates of the alongshore component of the current are relatively insensitive to coordinate rotation. However, the across-shore component of current velocity is relatively weak and highly sensitive to the definition of the across-shore direction. An error of ± 2 cm/s in the across-shelf current results from an angle error of 2° if the along-shelf current speed is 40 cm/s. The angle error due to EMCM alignment alone results in $\pm 2^\circ$, the compass on the tripod causes at least an additional $\pm 2^\circ$ measurement error, and the local orientation of the bathymetry is similarly uncertain. This does not cause a problem in estimating the magnitude of bottom shear stress (See Ch. 2), but becomes problematic in estimating across-shelf sediment flux, particularly during a storm when dominant the current direction is shore parallel.

It is not clear how much directional error occurred due to the combined effect of intrinsic instrument error, alignment error and compass error. Thus current directions were determined by defining across-shore as the direction of minimum variance for all measurements of burst-averaged current velocity during the experiment. This is equivalent to defining the along-shore direction as the direction of maximum variance for all measurements of burst-averaged velocity. Angle-corrected along- and across-shelf current velocities at 0.93, 3.25, 5, 6.75, 8.5 and 10.5 m ab are shown in Figure 3-2 and 3-3, respectively, along with variation associated with a 3° rotation either direction. Currents in Figures 3-2 and 3-3 are tidally-averaged using a 15-hour low pass filter.

3.3. WIND-DRIVEN CURRENT MODEL

The wind-driven current model adopted here is a solution to the time-averaged, linearized momentum equations for a homogeneous fluid (Mitchum and Clarke, 1985; Jenter and Madsen, 1989):

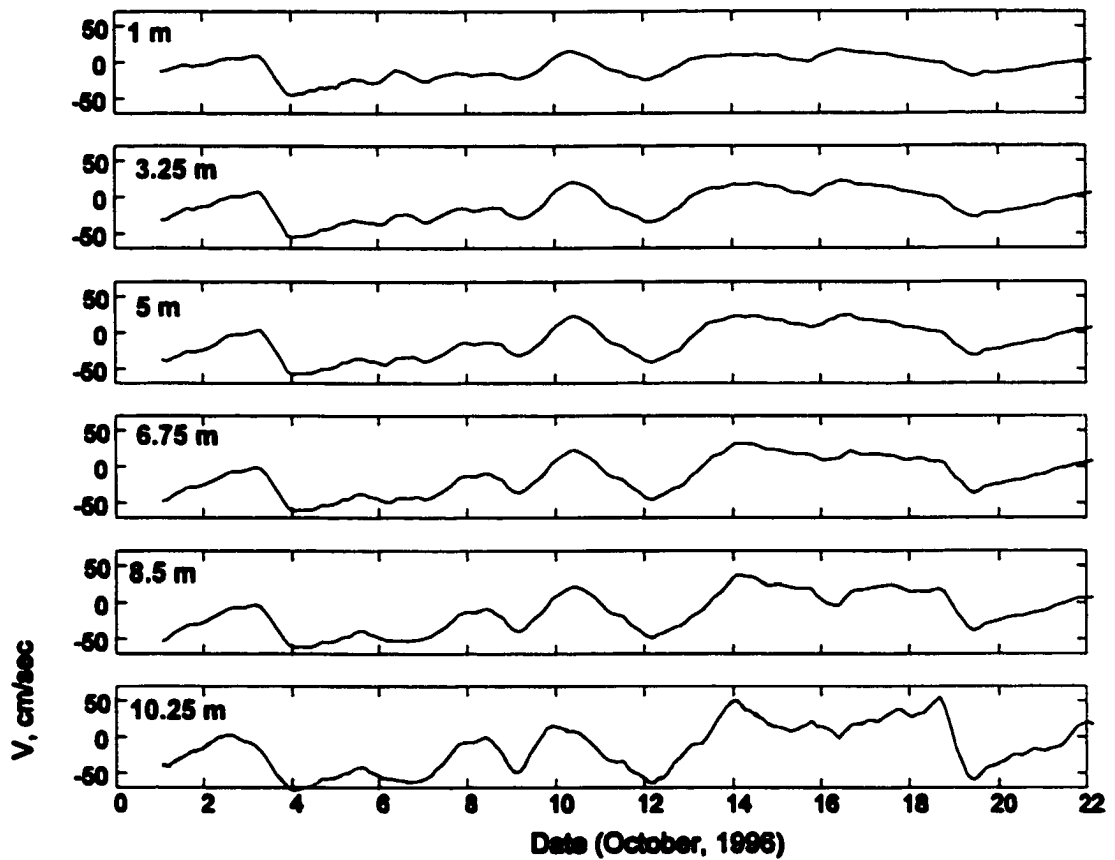


Figure 3-2. Angle-corrected along-shelf current velocities at 0.93, 3.25, 5, 6.75, 8.5 and 10.5 m ab, along with (the virtually undetectable) variation associated with a 3° rotation either direction.

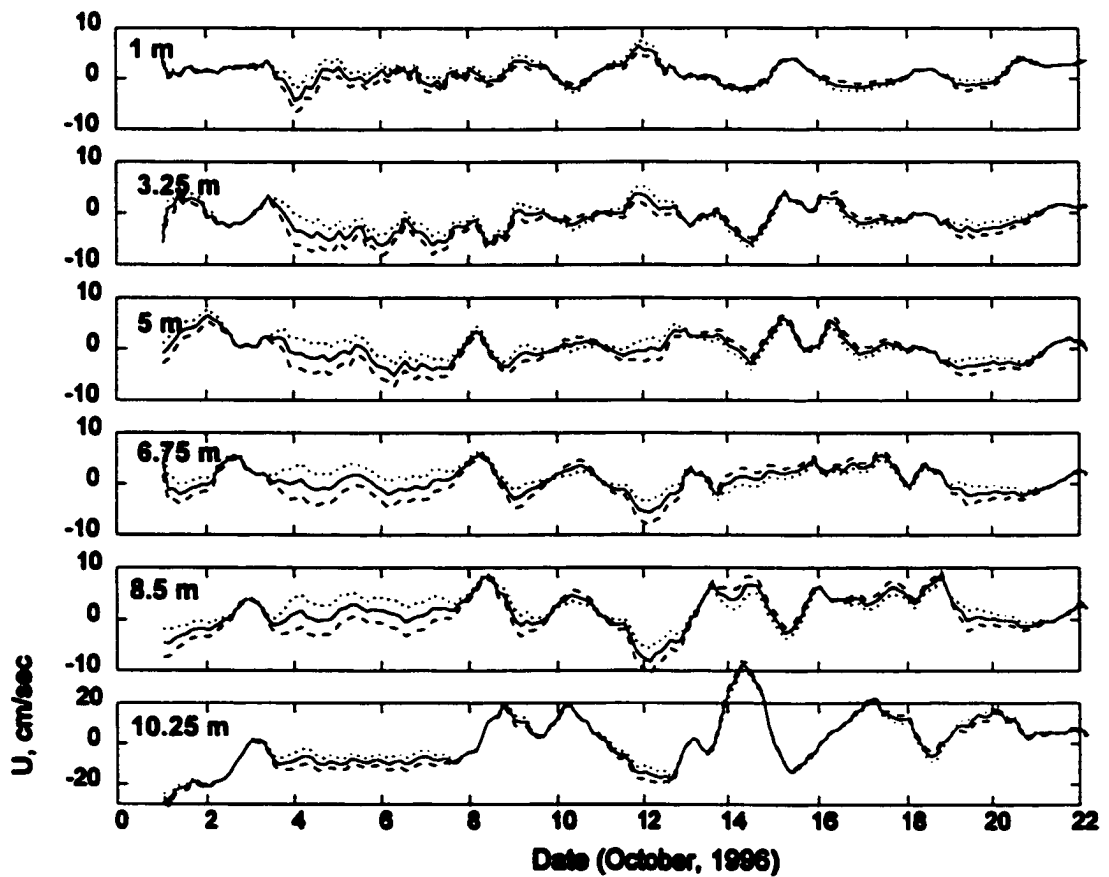


Figure 3-3. Angie-corrected across-shelf current velocities at 0.93, 3.25, 5, 6.75, 8.5 and 10.5 m ab, along with variation associated with a 3° rotation either direction.

$$-fv = -g \frac{\partial \zeta}{\partial x} + \frac{1}{\rho} \frac{\partial \tau_x}{\partial z} \quad (3-5a)$$

$$fu = -g \frac{\partial \zeta}{\partial y} + \frac{1}{\rho} \frac{\partial \tau_y}{\partial z} \quad (3-5b)$$

where u, v is the velocity in the x - y plane, f is the Coriolis parameter, ζ is the sea surface elevation, and τ_x, τ_y is the turbulent Reynolds' stress vector. Relating the turbulent shear stress term to the flow kinematics through the use of a turbulent eddy viscosity, A_z , gives:

$$\tau_x/\rho = A_z \partial u / \partial z \quad (3-6a)$$

$$\tau_y/\rho = A_z \partial v / \partial z \quad (3-6b)$$

Inserting (3-6) into (3-5) and then rearranging it by taking its dot product with $(1, i)$ ($i = \sqrt{-1}$) yields

$$\frac{d}{dz} \left(A_z \frac{dW}{dz} \right) - i f W = 0 \quad (3-7)$$

where $W = (u+iv) - (g/f)(-\partial \zeta / \partial y + i \partial \zeta / \partial x)$ is a complex representation of the difference between the total velocity and its depth-independent geostrophic component.

3.3.1. Momentum Balance

The depth-averaged momentum equations in their entirety are given by

$$\frac{\partial \bar{v}}{\partial t} + \bar{u} \bullet \bar{\nabla} \bar{v} + f \bar{u} = -g \frac{\partial \bar{\eta}}{\partial y} + \frac{1}{\rho h} [\tau_{sy} - \tau_{by} + \frac{\partial S_{xy}}{\partial x}] \quad (3-8a)$$

$$\frac{\partial \bar{u}}{\partial t} + \bar{u} \bullet \bar{\nabla} \bar{u} - f \bar{v} = -g \frac{\partial \bar{\eta}}{\partial x} + \frac{1}{\rho h} [\tau_{sx} - \tau_{bx} + \frac{\partial S_{xx}}{\partial x}] \quad (3-8b)$$

where $\bar{u}(x, y)$ is the time-averaged current vector, \bar{u} and \bar{v} are the depth averaged along-shelf and across-shelf components of the mean current, t is time, f is Coriolis

frequency, g is acceleration of gravity, ρ is water density, h is water depth, $\bar{\eta}$ is mean-surface elevation, τ_y and τ_b are surface and bottom shear stresses with subscript y and x designating the along-shelf and across-shelf components, S_{xy} is the oblique component of surface gravity wave radiation stress and S_{xx} is the component in the direction of wave propagation.

Figure 3-4 displays 12-hour low-passed time series of the local acceleration, Coriolis, pressure gradient, surface and bottoms stresses. Since available observations of the alongshelf pressure gradient are limited to barotropic components, the pressure gradient includes only the barotropic components which is calculated from tide gauge records at the Oregon inlet and the Chesapeake Bay Bridge. The nonlinear term and the radiation stress gradient term are not included in Figure 3-4 because they cannot be accurately estimated with this data set and are known to be small (Lentz et al., 1999). Largest terms are the surface and bottom shear stresses and the barotropic pressure gradients. Lentz et al. (1999) found that the along-shore momentum balance in the inner shelf (13-m depth) is between the surface and bottom shear stresses, with along-shelf pressure gradients usually a small contribution. The sum of the response terms $[\partial\bar{v} / \partial t + \tau_{by} / (\rho h)]$ was reported to be well correlated with the sum of two forcing terms $[-\rho^{-1}\partial P / \partial y + \tau_{sy} / (\rho h)]$ and its regression coefficient was about 1.0. In this study, the correlation between the surface and bottom shear stresses is high ($r=0.70$) and the correlation coefficient between two forcing terms and two response terms are only 0.81. This may result from inadequate resolution of the along-shelf barotropic pressure gradient and entirely neglecting the along-shelf baroclinic pressure gradient.

Available observations of the across-shelf pressure gradient are not of sufficient quality to justify a similar estimate of the across-shelf momentum balance. However, Lentz et al. (1999) reported the cross-shelf momentum balance at 13 m to be between the cross-shelf pressure gradient, wave radiation stress gradients, the Coriolis force, and to a less extent the cross-shelf wind stress.

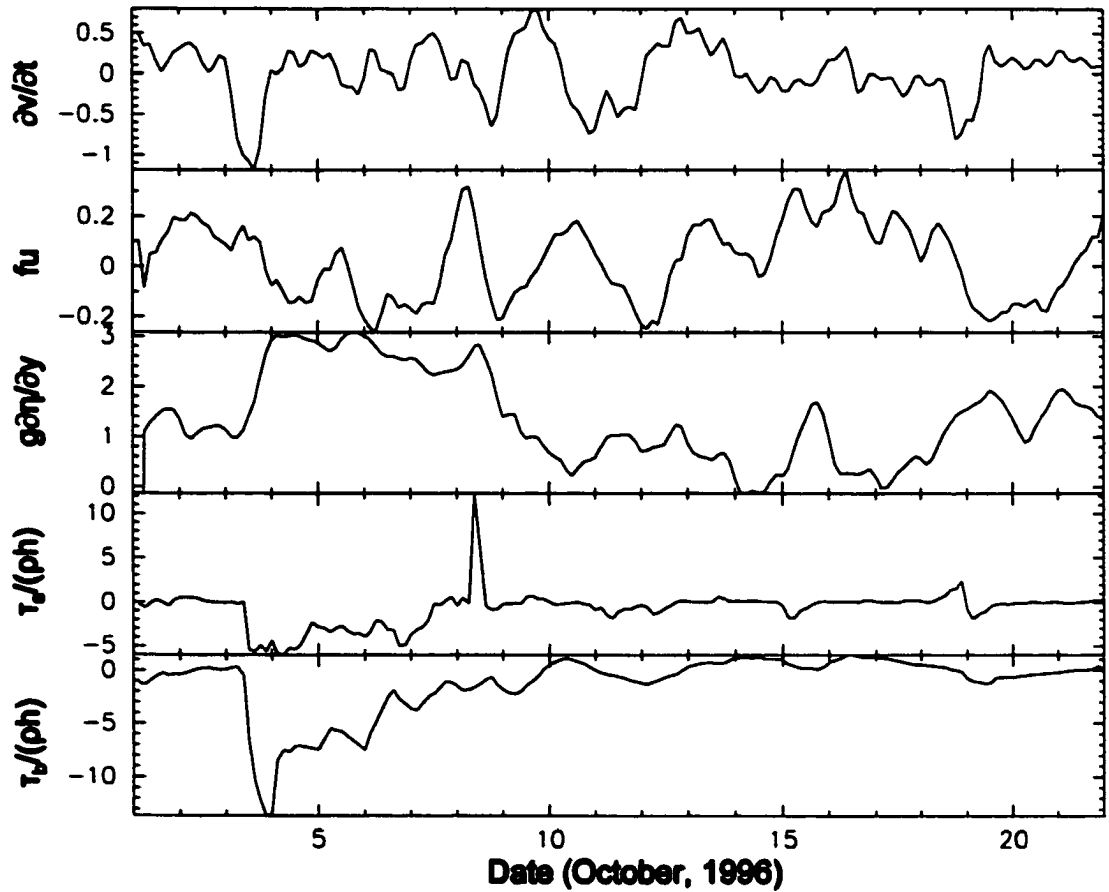


Figure 3-4. Time series of the largest terms in the along-shelf momentum balance at 13-m depth. Units are 10^{-5} cm/s^2 .

3.3.2. Bilinear Eddy Viscosity

In the Jenter and Madsen (1989) model, the eddy viscosity is assumed to have a bilinear form

$$A_z = \kappa u_{*s}(h-z) \quad z_m < z \leq h \quad (3-9a)$$

$$A_z = \kappa u_{*b} z \quad 0 \leq z < z_m \quad (3-9b)$$

where $\rho u_{*s}^2 = |\tau_s|$, $\rho u_{*b}^2 = |\tau_b|$ and

$$z_m = hu_{*b}/(u_{*s} + u_{*b}). \quad (3-10)$$

For bilinear eddy viscosity, Jenter and Madsen (1989) gave the following solution to (3-8)

$$W = A^* (ber 2\sqrt{f(h-z)/\kappa u_{*s}} + ibei 2\sqrt{f(h-z)/\kappa u_{*s}}) + B^* (ker 2\sqrt{f(h-z)/\kappa u_{*s}} + ikei 2\sqrt{f(h-z)/\kappa u_{*s}}) \quad z_m < z < h \quad (3-11a)$$

$$W = A^* (ber 2\sqrt{fz/\kappa u_{*b}} + ibei 2\sqrt{fz/\kappa u_{*b}}) + B^* (ker 2\sqrt{fz/\kappa u_{*b}} + ikei 2\sqrt{fz/\kappa u_{*b}}) \quad 0 < z < z_m \quad (3-11b)$$

where A^* and B^* are complex constants determined by surface and bottom boundary conditions and ber, bei, ker, and kei are zero-order Kelvin functions.

The boundary conditions for determining A^* and B^* are

$$W|_{z=z_0} = -\frac{g}{f} \left(-\frac{\partial \zeta}{\partial y} + i \frac{\partial \zeta}{\partial x} \right) \quad (3-12)$$

$$\lim_{z \rightarrow h} A_z \frac{dW}{dz} = \frac{\tau_{xx} + i\tau_{xy}}{\rho} \quad (3-13)$$

where τ_{xx} and τ_{xy} are the x and y component of the wind stress, τ_s . (3-12) specifies no slip at $z = z_0$ and (3-13) specifies that surface stress equals τ_s . These conditions are supplemented by matching conditions at the level of discontinuity in eddy viscosity to ensure continuous profiles of velocity and shear stress

$$W|_{z=z_m^-} = W|_{z=z_m^+} \quad (3-14)$$

$$A_z \frac{dW}{dz} \Big|_{z=z_m} = A_z \frac{dW}{dz} \Big|_{z=z_m} \quad (3-15)$$

The solution procedure for a long, straight inner shelf assumes along-shelf pressure gradients are negligible and that the mean depth-integrated cross-shelf velocity is zero such that

$$\int_{z_0}^h u dz = 0 \quad (3-16)$$

The solution can be obtained iteratively.

For model inputs, the surface shear stress, τ_s , was estimated as described in section 3.2.1. The bottom roughness was set at 1×10^{-4} m and the surface roughness was set at 1×10^{-3} m. Figure 3-5 and 3-6 display the tidally-averaged observed (solid line) and modeled (dash line) along- and across-shelf current velocity at .93, 3.25, 5, 6.75, 8.5, 10.25 m ab. Reasonable agreement was found between predicted and observed along-shelf current velocities with correlations greater than 0.60 for all depths (Table 3-2). Disagreement may largely be due to neglect of along-shelf barotropic and baroclinic pressure gradients. Rennie et al. (1999) observed that a low-salinity plume extended from Chesapeake Bay to Duck and interacted with wind-driven circulation during the CoOP experiment of 1994. Lentz et al. (1999) also indicated that along-shelf pressure gradients were important over the inner shelf during events associated with a low-salinity plume from the Chesapeake Bay. In addition, the effective wind drag might be higher during storms in the inner shelf off Duck (Friedrichs and Wright, 1997; Madsen et al., 1993), perhaps due to occasional depth-limited wave breaking outside the surf zone.

The predicted across-shelf current velocities are problematic. Positive correlations occurred only near the boundaries (Table 3-2). In the middle water column, the direction of the modeled across-shelf current was largely opposed to the observed current (Table 3-2; Figure 3-6). Kim et al. (1997) reported that although the Jenter and Madsen model reproduced the current velocity (along-shelf current was dominant) quite well at 20-m depth during a significant storm in October 1994 at Duck, NC, the predicted across-shelf current direction was opposite to the observed currents. They attributed the

Correlation							
Height ab	Along-shelf			Across-shelf			
	Bilinear		Constant	Bilinear	Constant		
m	JM	fu ignored	MC	JM	MC	τ_x	τ_y
0.93	0.683	0.659	0.602	0.085	0.323 (0.567)	0.228 (0.582)	0.375 (0.475)
3.25	0.650	0.650	0.600	-0.086	0.017 (0.452)	0.013 (0.637)	0.061 (0.144)
5	0.651	0.654	0.598	-0.267	0.009 (0.175)	0.180 (0.389)	-0.212 (-0.246)
6.75	0.666	0.664	0.592	-0.072	-0.089 (-0.211)	-0.070 (-0.199)	0.497 (-0.610)
8.5	0.667	0.661	0.581	0.113	0.518 (0.719)	0.355 (0.426)	0.572 (0.727)
10.25	0.785	0.786	0.781	0.568	0.760 (0.754)	0.909 (0.901)	0.288 (0.348)
Average absolute difference between observed and predicted currents							
0.93	8.69	9.10	11.87	1.88	2.01 (2.08)	1.74 (1.71)	3.00 (3.76)
3.25	12.97	12.81	15.57	3.02	3.83 (2.82)	3.31 (1.89)	5.60 (6.68)
5	15.08	14.98	17.60	3.33	3.33 (3.12)	2.96 (2.74)	4.41 (5.34)
6.75	16.88	16.54	18.95	3.26	2.51 (2.74)	2.54 (2.81)	2.22 (2.59)
8.5	18.76	18.02	20.20	3.59	2.73 (2.47)	2.77 (3.02)	2.98 (2.88)
10.25	22.91 (20.89)	19.71 (17.33)	20.17	9.34	7.08 (7.64)	6.56 (7.02)	10.77 (10.88)

Table 3-2. Correlations and average absolute differences between observed and modeled along- and across-shelf current velocities. Parentheses indicate exclusion of data during the October 1996 storm

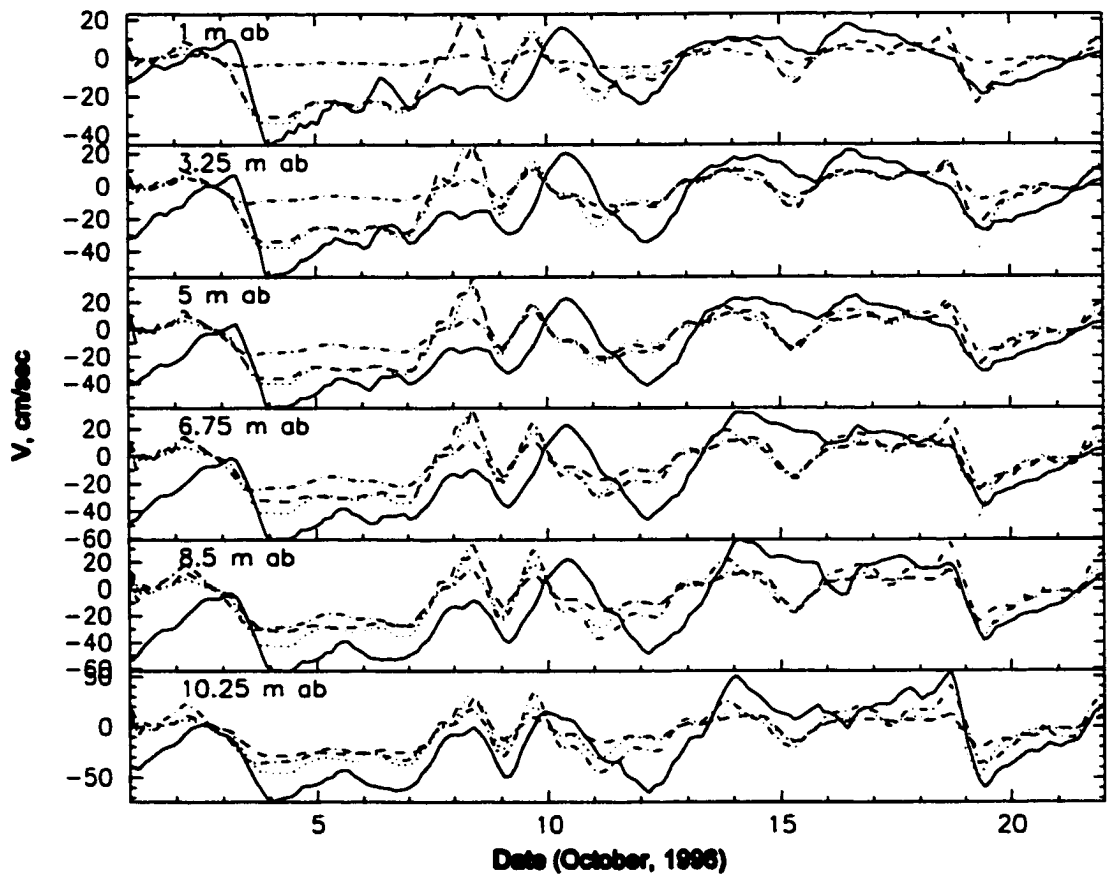


Figure 3-5. Comparison of observed and predicted along-shelf current velocities at 6 heights. Solid - observed; dash - predicted (Jenter and Madsen); dash-dot - predicted (Mitchum and Clarke); dot - predicted (fu neglected, bilinear eddy viscosity).

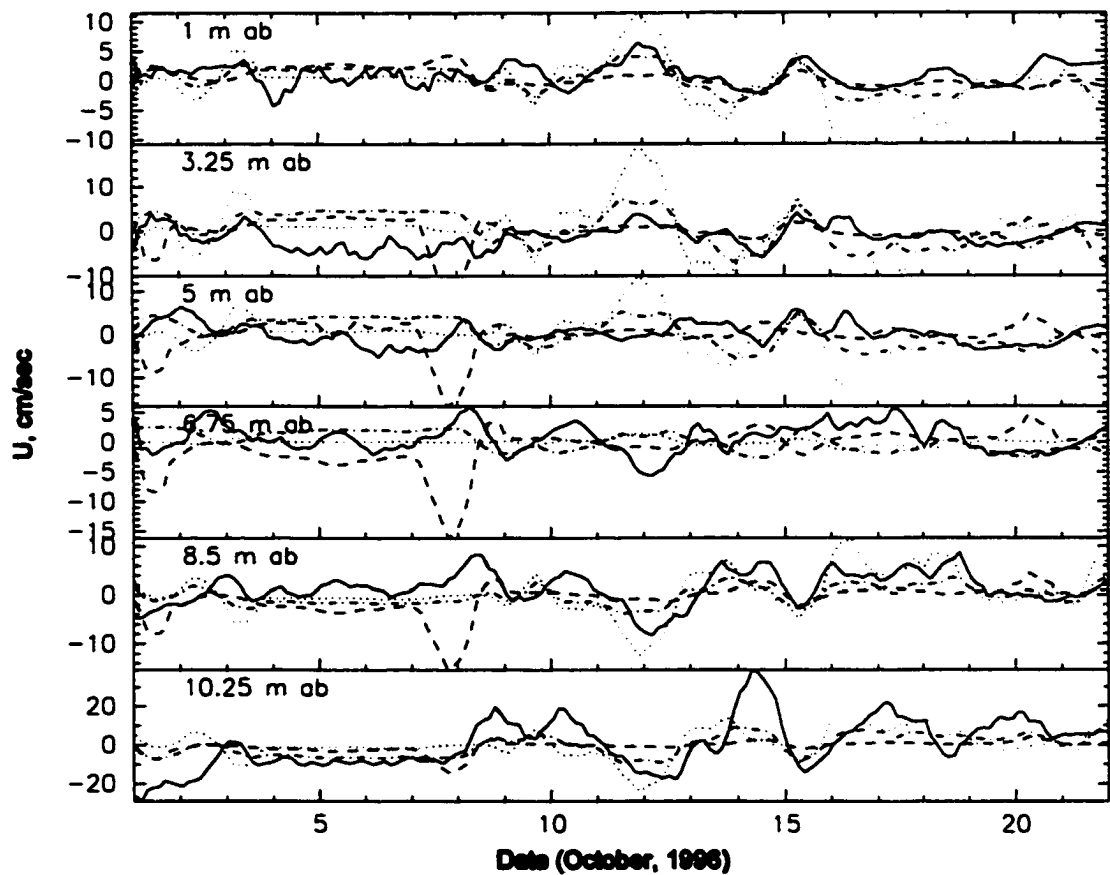


Figure 3-6. Comparison of observed and predicted across-shelf current velocities at 6 heights. Solid - observed; dash - predicted (Jenter and Madsen); dash-dot - predicted (Mitchum and Clarke); dot - predicted (f_u neglected, constant A_2).

near-bottom across-shelf flow variation to other possible sources such as stratification and wave effects (considered later in this paper). If stratification due to a low-salinity coastal plume as Rennie et al. (1999) observed, were present, bilinear eddy viscosity as implemented in the Jenter and Madsen model may be inadequate. In the next section, constant eddy viscosity, which is more consistent with stratification effects, is considered.

3.3.3. Constant Eddy Viscosity

Mitchum and Clarke (1985) presented an analytical solution to (3-8) for the same boundary conditions as Jenter and Madsen (1989), but using a constant eddy viscosity:

$$W = \left(\frac{2Q}{(1+i)\delta} \right) \frac{\sinh\left[(1+i)\left(\frac{z+h}{\delta}\right)\right]}{\cosh\left[(1+i)\left(\frac{h}{\delta}\right)\right]} - W_o \frac{\cosh\left[(1+i)\left(\frac{z}{\delta}\right)\right]}{\cosh\left[(1+i)\left(\frac{h}{\delta}\right)\right]} \quad (3-17)$$

where $\delta = (2A_z/f)^{1/2}$ and W_o is given by (3-13).

Mitchum and Clarke (1986) did not explicitly formulate A_z in terms of τ_x . A_z can be estimated from observations by rearranging (3-6b):

$$A_z = (\tau_x/\rho) / (\partial v/\partial z) \quad (3-18)$$

Apparent eddy viscosity was estimated by equating τ_x to observed τ_y and using current velocities obtained by the ADP to calculate $\partial v/\partial z$. The resulting estimate of A_z is not calibrated a priori to the across-shelf velocity, since only v was used in fitting (3-18). In estimating apparent eddy viscosity, only velocities in the middle water column (3 to 9 m) were used to avoid the logarithmic boundary layers where A_z is clearly not constant.

Figure 3-7a plots the apparent eddy viscosity against the surface shear stress. Although highly scattered, the apparent eddy viscosity increases with increasing surface shear. To reduce the scatter, values of eddy viscosity were grouped into logarithmic windows of the surface shear stress and median values for each window were obtained (Figure 3-7b).

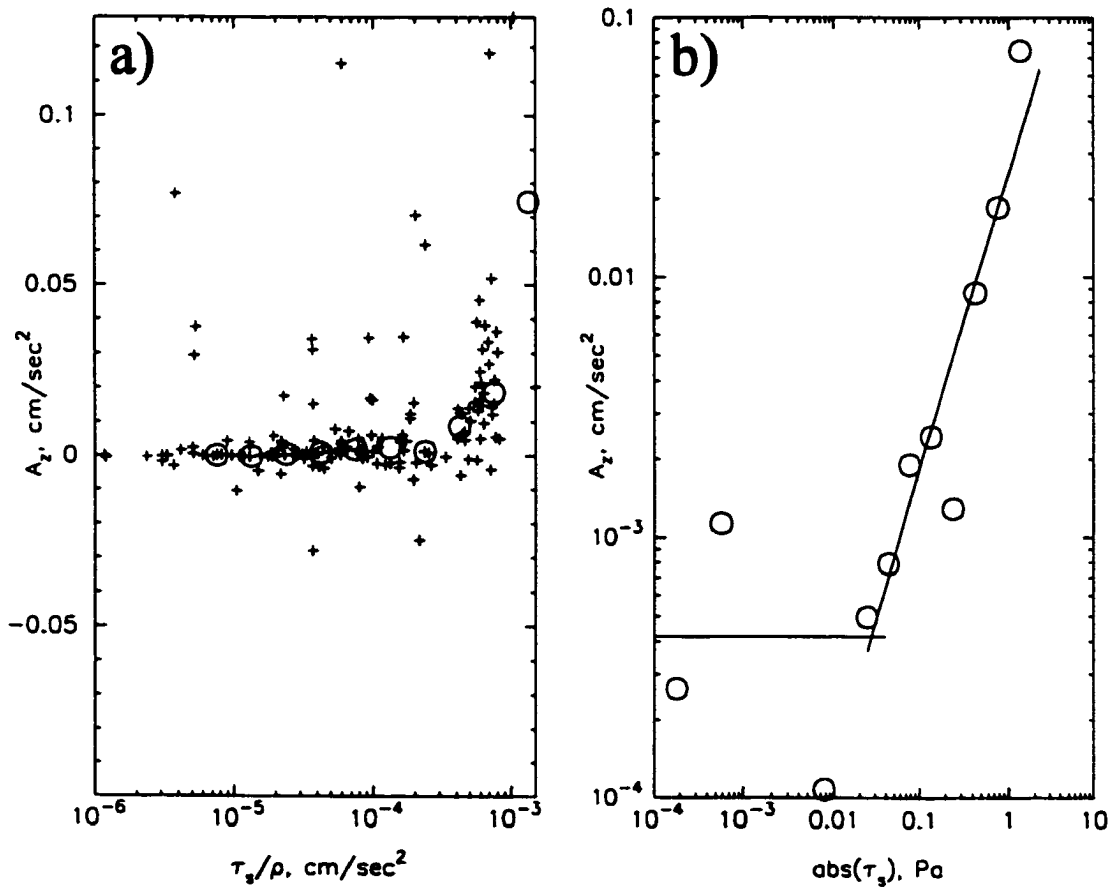


Figure 3-7. a) Apparent eddy viscosity versus surface shear stress, b) Best-fit between (τ_s/ρ) and A_z with A_z lagged 3 hours behind (τ_s/ρ) .

Since the flow in the middle water column takes time to reach steady state with the surface shear stress, various time-lagged A_z values were fitted with the shear stress. The best fit between (τ_s/ρ) and A_z occurred when A_z was lagged 3 hours behind the surface shear stress (Figure 3-7b) and A_z was found to be

$$A_z = 63.27 \times (|\tau_s|/\rho)^{1.132} \quad \text{for } |\tau_s| > 0.027 \text{ Pa} \quad (3-19a)$$

$$A_z = 4.175 \times 10^{-4} \quad \text{for } |\tau_s| \leq 0.027 \text{ Pa} \quad (3-19b)$$

The other inputs to the constant eddy viscosity model were the same values applied in Section 3.1. In applying (3-17), the along-shelf pressure gradient was assumed to be zero and the depth-integrated across-shelf current was forced to be zero to account for the return flow at the boundary. The predicted along- and across-shelf current velocities at 6 depths are shown as dotted lines in Figures 3-5 and 3-6, respectively. Moderate correlations ($r=0.63$ on average) between the predicted and observed along-shelf current velocities were obtained (Table 3-2). Close inspection of along-shelf current velocities reveals that the modeled near-bed velocities are close to zero during the storm and the average absolute difference between the observed and modeled along-shelf currents are higher than for the bilinear A_z model. This is because constant eddy viscosity does not adequately represent the enhanced shear in the along-shelf current very near the boundary.

However, correlations between the observed and predicted across-shelf current velocities reveal an encouraging result. Not only do correlations generally increase, but a positive relationship is achieved through most of the water column (Table 3-2). Furthermore, the average absolute differences between observed and modeled across-shelf currents are generally smaller for constant A_z . This may be because constant A_z is a better representation of the effects of density stratification in the middle portion of the water column. The vertical structure of the along-shelf current is most sensitive to the structure of A_z very near the boundaries, which is better represented as bilinear. In contrast, stress does not dominate the across-shelf balance. Thus shear in the across-shelf current is distributed more evenly throughout the water column and is more sensitive to the structure of eddy viscosity in the middle water column. Still, in the middle water

column, negative correlations were obtained. The negative correlation at 6.75 m ab may result from an inadequate representation of the turning point of the currents.

3.3.4. Analytical Solution with f_u Neglected

If f_u is small, the along- and across-shelf momentum balances decouple, and the along-shelf balance provides a simple solution for the along-shelf current in terms of the wind forcing. Neglecting the Coriolis term, f_u , in the along-shelf momentum is justified by the fact that f_u is usually small on the inner shelf at Duck, NC, under energetic wind forcing (e.g., Lentz et al., 1999). By assuming zero along-shelf pressure gradients as before, the along-shelf momentum equation reduces simply to

$$\tau_y^s = \tau_y = A_z \partial v / \partial z \quad (3-20)$$

throughout the water column. The boundary conditions on (3-20) consist of no-slip at the bottom ($v=0$ at $h=-z$) and the matching of surface stress and wind stress at the free surface ($A_z \partial v / \partial z = \tau_y^s / \rho$ at $z=0$).

The solution to (3-20) with constant eddy viscosity is

$$v = \tau_y^s h / (\rho A_z) (1 + z/h) \quad (3-21)$$

The predicted along-shelf current velocities are shown in Figure 3-5. The along-shelf current structure is virtually the same as that predicted by the Mitchum and Clarke model. It was shown earlier that a bilinear eddy viscosity profile predicted along-shelf currents more accurately, in particular at the boundaries (Table 3-2). Thus, (3-21) was also solved using a bilinear structure for eddy viscosity (3-9) and the solution is given by

$$v = -\tau_y^s / (\rho \kappa u_{*s}) \log(-z/z_m) + v(-z_m) \quad \text{for } z > -z_m \quad (3-22a)$$

$$v = \tau_y^s / (\rho \kappa u_{*b}) \log(z'/z_b) \quad \text{for } z \leq -z_m \quad (3-22b)$$

where $z' = h+z$. The surface and bottom shear velocity in (3-22) are $u_{*s} = (\tau_y^s / \rho)^{1/2}$ and $u_{*b} = (\tau_y^s / \rho)^{1/2}$. As expected, the along-shelf current velocities predicted by (3-22) are nearly identical to the Jenter and Madsen solution and are closer to the observed currents than those predicted by (3-21) (Figure 3-5, Table 3-2).

For the constant eddy viscosity case, it is relatively straightforward to substitute

(3-20) into (3-5b) and integrate in z to solve for cross-shelf velocity. To facilitate an analytical solution, u and $\partial\eta/\partial x$ were broken into x - and y -wind components:

$$A_z \partial u_{y\text{-wind}} / \partial z = - \int_z^0 \{g \partial \eta_{y\text{-wind}} / \partial x + f v\} dz \quad (3-23)$$

$$A_z \partial u_{x\text{-wind}} / \partial z = - \int_z^0 g \partial \eta_{x\text{-wind}} / \partial x dz + \tau_s^x / \rho \quad (3-24)$$

The boundary conditions are no-slip at the bed and no flow through the coast. The solutions for (3-23) and (3-24) for constant eddy viscosity are

$$u_{y\text{-wind}} = \tau_s^y h^3 f / (48 \rho_o A_z^2) (1 - 9z^2/h^2 - 8z^3/h^3) \quad (3-25)$$

$$u_{x\text{-wind}} = \tau_s^x h / (4 \rho_o A_z) (1 + 4z/h + 3z^2/h^2) \quad (3-26)$$

The model inputs are the same as those applied to the models considered previously. The predicted current velocities using (3-25) and (3-26) are shown in Figure 3-6. Correlations between the observed and predicted across-shelf current velocities increase slightly compared to those of the Mitchum and Clarke model. It is also interesting that the correlations between the observed current velocities and the predicted current velocities using $u_{x\text{-wind}}$ alone are highest on average (Table 3-2). Moreover, the average absolute difference between observed and predicted currents is smallest for (3-26) among the models considered. Correlations between (3-26) and observed across-shelf currents become even greater if data from the peak of the storm are removed from the comparison. If storm data are included, then $u_{y\text{-wind}}$ is better correlated than $u_{x\text{-wind}}$ to across-shelf currents recorded nearest the bed.

3.4. WAVE AND WAVE-DRIVEN CURRENT MODEL

In the previous section, models for wind-driven currents did not predict the observed across-shelf currents particularly well. Recent studies of inner shelf hydrodynamics have identified important roles for waves in the mean across-shelf momentum equation (Lentz et al., 1999) and in generating mean currents (Xu and Bowen,

1994). In this section, formulations are presented for orbital velocity, followed by simple wave transformation, and then wind-driven steady currents due to boundary layer streaming and return flow.

3.4.1. Wave Orbital Velocity

The leading order solutions for small amplitude, purely progressive waves propagating toward -x (unaffected by turbulence outside of the thin wave boundary layer) are the Airy result (e.g., Dean and Dalrymple, 1984):

$$\eta' = H/2 \cos(kx + \omega t) \quad (3-27)$$

$$u_b = H/2 \omega \{ \cosh k(h+z) \} / (\sinh kh) \cos(kx + \omega t) \quad (3-28)$$

$$\omega^2 = gk \tanh kh \quad (3-29)$$

where η' and u_b are wave elevation and orbital velocity, H is wave height, k is wave number, and ω is wave radian frequency. Wave asymmetry must be considered to produce non-zero bedload transport. The second order Stokes velocity, u_{2b} , is given as

$$u_{2b} = (kH_{rms}/2)^2 C_w \frac{\cosh 2k(h+z)}{\sinh^4 kh} \cos 2(kx - \omega t) \quad (3-30)$$

where H_{rms} is the rms wave height and $C_w = \omega/k$ is the wave celerity calculated from (3-29).

3.4.2. Wave Transformation

Wave transformation in the inner shelf is described here in terms of linear wave theory (Dean and Dalrymple, 1992). The energy transmitted forward between two adjacent wave orthogonals is

$$P_1 = nbEC_w \quad (3-31)$$

where b is the spacing between the orthogonals, E is total wave energy per unit surface area given by

$$E = (2/8)\rho g H^2 \quad (3-32)$$

and n is the ratio of wave group to phase velocity given by

$$n = \frac{1}{2} \left[1 + \frac{4\pi h/L}{\sinh(4\pi h/L)} \right] \quad (3-33)$$

Assuming constant energy transmission, the wave energy transmitted in deep water is

$$P_o = (1/2)b_o E_o C_{wo} \quad (3-34)$$

where the subscript o refers to deepwater conditions.

Equating (3-31) and (3-34) and then arranging them in terms of wave height,

$$H/H_o = \sqrt{E/E_o} = \sqrt{(1/2)(1/n)(C_{wo}/C_w)} \sqrt{b_o/b} \quad (3-35)$$

The term $\sqrt{(1/2)(1/n)(C_{wo}/C_o)}$ in (3-35) is the shoaling coefficient, K_s . This shoaling coefficient is a function of wavelength and water depth. Knowing the deepwater wave height, (3-35) enables determination of wave heights in transitional shallow water when the relative spacing between orthogonals can be determined.

The square root of this relative spacing, $\sqrt{b_o/b}$, in (3-35) is the refraction coefficient, K_r . The change of direction of an orthogonal as it passes over relatively simple bathymetry may be approximated by using the Snell's law

$$\sin \alpha = \sin \alpha_o C_w/C_{wo} \quad (3-36)$$

where α is the angle between the wave crest and the shoreline, and α_o is the angle between the deep water wave crest and the shoreline. From the geometry of the wave rays,

$$K_r = (b_o/b)^{1/2} = (\cos \alpha_o / \cos \alpha)^{1/2} \quad (3-37)$$

Thus, assuming that the wave energy is conserved, and neglecting reflection, diffraction and frictional dissipation, the wave height, H , at intermediate or shallow water can be determined from

$$H = H_o K_s K_r \quad (3-38)$$

Figure 3-8 displays near-bottom wave velocities observed at 8- and 13-m depths and inverse-transformed from 8 m to 13 m. The transformed near-bottom wave orbital

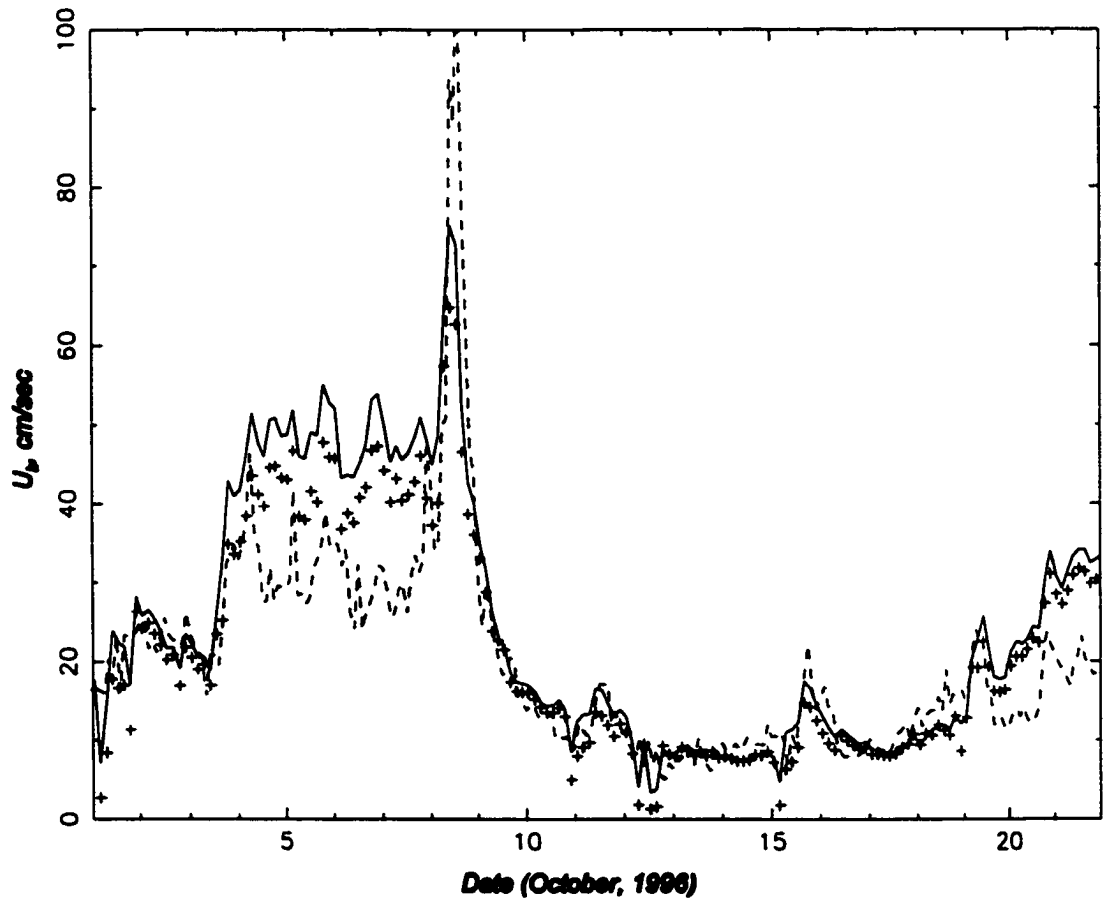


Figure 3-8. Comparison of u_b . Solid - u_b converted from observed H_{m0} at 8-m depth by the FRF; dash - observed u_b at 13-m depth; + - u_b transformed from 8-m to 13-m depth.

velocities reproduce the observed u_b well. During the storm, however, the transformed u_b overestimate the observed u_b . This may be because the wave transformation did not address wave attenuation due to bottom friction. Figure 3-9 displays wave direction observed at 8- and 13-m depths and inversed-transformed from 8 m to 13 m. The transformed wave direction also reproduces the observed wave direction well.

3.4.3. Wave-Driven Steady Current

Here it is assumed that the return flow associated with Stokes drift and boundary layer streaming are governed by a balance between surface slope and friction (e.g., Haines and Sallenger, 1994; Putrevu and Svendsen, 1993):

$$A_z \partial u_{\text{return}} / \partial z = - \int_z^0 g \partial \eta_{\text{return}} / \partial x dz \quad (3-39)$$

$$A_z \partial u_{\text{stream}} / \partial z = - \int_z^0 g \partial \eta_{\text{stream}} / \partial x dz \quad (3-40)$$

Along with no flow at the bed, (3-39) is constrained by the depth-integrated condition (e.g., Haines and Sallenger, 1994; Petrevu and Svendsen, 1993)

$$\int_{-h}^0 u_{\text{return}} dz = - \langle \int_0^{\eta'} u dz \rangle \quad (3-41)$$

The time-varying upper limit of the integration is dropped from the left hand side of (3-41) because it is a second-order contribution. On the right hand side, the only time-averaged contribution comes from the region between the trough and crest. From (3-28) and (3-29), it follows that

$$Q_w = - \langle \int_0^{\eta'} u dz \rangle = gH^2 k / (8\omega) \quad (3-42)$$

Note that below the wave trough level, the Eulerian velocity u varies harmonically in time and does not contribute to Q_w .

Rather than no flow at $z = -h$, the bottom boundary condition on (3-40) is $u_{\text{stream}} = U_w$ at $z = -h + \delta_w$ where U_w is the wave-averaged velocity at the top of the wave boundary

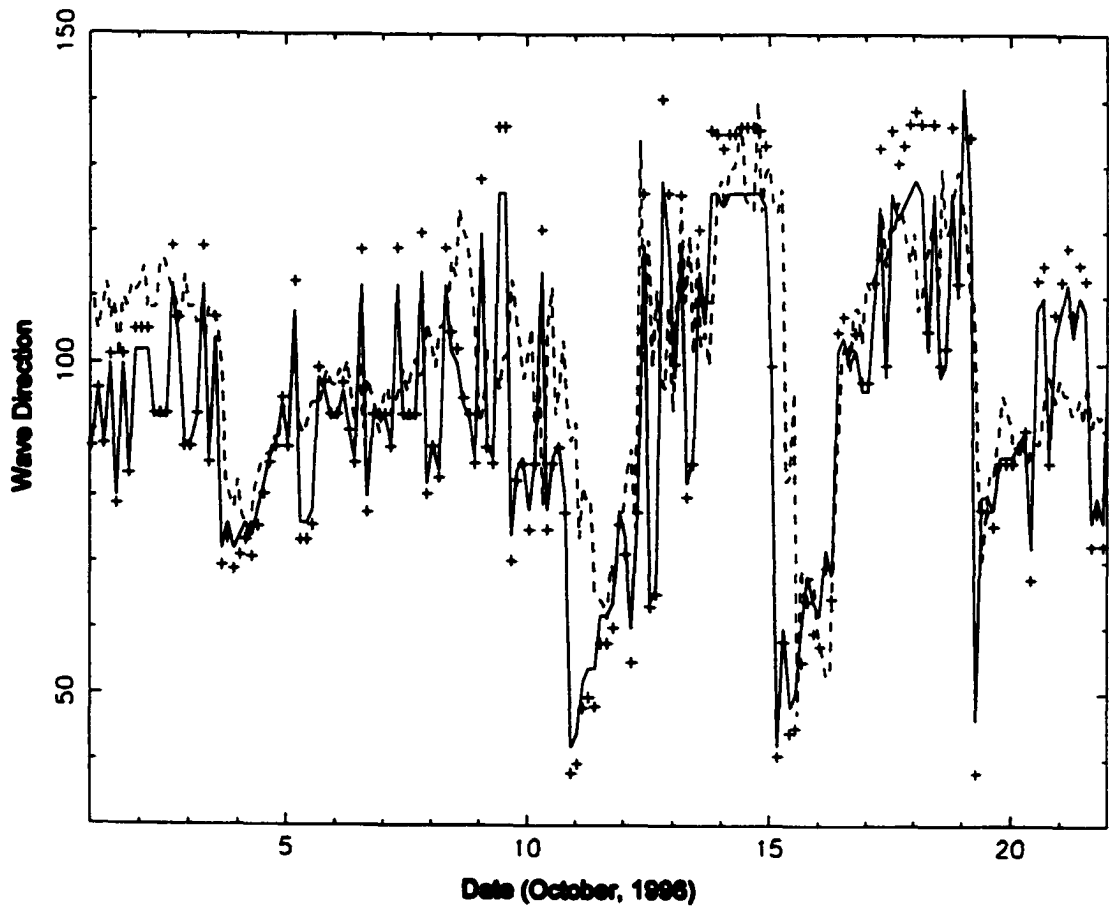


Figure 3-9. Comparison of wave directions. Legends are the same as in Figure 3-8.

layer, $z' = \delta_w$ due to boundary layer streaming. In addition, (3-40) is subject to no flow through the coast. The simplest relation for U_w assumes an eddy viscosity of arbitrary vertical structure within the wave boundary layer which does not vary in magnitude over a wave period. As shown by Longuet-Higgins (1958), it then follows that with $+x$ offshore

$$U_w = -(3/16) H^2 k \omega / (\sinh kh)^2 \quad (3-43)$$

The constant eddy viscosity solutions for mean wave-driven across-shelf velocity are:

$$u_{\text{return}} = 3Q_w / (2h) (1 - z^2/h^2) \quad (3-44)$$

$$u_{\text{stream}} = -(u_{\text{bsl}}/2) (1 - 3z^2/h^2) \quad (3-45)$$

A correlation matrix was obtained between the observed currents and the predicted current with return, streaming and both in addition to the wind-driven currents (Table 3-3). Unfortunately, inclusion of the wave-driven current does not improve the overall current prediction. The f_u -neglected current model is still best among the current models considered in predicting the across-shelf current velocities.

3.5. DISCUSSION AND CONCLUSIONS

The simplest possible analytical solutions were sought for wind- and wave-driven currents over the inner shelf which still capture the lowest-order hydrodynamics fundamental to across-shelf sediment transport. Two of three wind-driven current models considered are solutions to the time-averaged, linearized equations for a rotating, homogeneous, viscous fluid. One assumes bilinear eddy viscosity (Jenter and Madsen, 1989), while the other assumes constant eddy viscosity (Mitchum and Clarke, 1986). In the third wind-driven current model, the Coriolis term, f_u , in the along-shelf momentum is neglected, which decouples the along-shelf and across-shelf momentum balance and provides the simplest solutions. Wave-driven currents due to Stokes return flow and boundary layer streaming were formulated and were forced by the results of predicted wave transformation.

Correlation									
Height ab cm	MC			τ_x			τ_y		
	Return	Stream	Both	Return	Stream	Both	Return	Stream	Both
0.93	0.268	0.375	0.359	0.38 (0.64)	0.44 (0.35)	0.42 (0.41)	0.35 (0.49)	0.39 (0.43)	0.39 (0.45)
3.25	-0.138	0.102	-0.077	-0.03 (0.68)	0.10 (0.61)	0.004 (0.66)	-0.05 (0.15)	0.11 (0.14)	-0.00 (0.15)
5	-0.127	0.012	-0.126	-0.15 (0.34)	-0.07 (0.39)	-0.15 (0.34)	-0.30 (-0.27)	-0.21 (-0.25)	-0.30 (-0.27)
6.75	-0.032	-0.072	-0.025	-0.09 (-0.29)	-0.17 (-0.22)	-0.08 (-0.30)	0.09 (-0.54)	-0.35 (-0.63)	-0.07 (-0.51)
8.5	0.457	0.601	0.406	0.64 (-0.09)	0.64 (0.33)	0.63 (0.05)	0.58 (0.69)	0.60 (0.72)	0.56 (0.68)
10.25	0.706	0.770	0.641	0.61 (0.83)	0.64 (0.88)	0.59 (0.80)	0.19 (0.34)	0.27 (0.35)	0.16 (0.34)
Average absolute difference between observed and predicted currents									
0.93	2.20	2.48	2.22	3.56 (1.59)	3.72 (2.08)	3.50 (1.95)	3.05 (3.72)	3.78 (3.98)	3.48 (3.93)
3.25	4.80	3.50	4.44	7.54 (1.67)	6.30 (2.02)	7.20 (1.78)	6.50 (6.76)	5.28 (6.68)	6.16 (6.75)
5	4.58	3.32	4.56	6.50 (2.54)	5.30 (2.75)	6.48 (2.54)	5.53 (5.44)	4.40 (5.34)	5.52 (5.44)
6.75	3.81	2.60	4.08	4.02 (2.68)	2.84 (2.74)	4.28 (2.07)	3.35 (2.68)	2.22 (2.60)	3.63 (2.72)
8.5	2.91	2.34	3.44	3.30 (3.27)	2.76 (3.05)	3.83 (3.38)	3.46 (2.90)	2.67 (2.89)	3.98 (2.99)
10.25	8.29	7.32	8.77	9.11 (6.90)	8.11 (6.89)	9.62 (6.95)	12.08 (10.7)	11.08 (10.8)	12.51 (10.7)

Table 3-3. Correlations and average absolute differences between observed and modeled across-shelf current velocities. Parentheses indicate exclusion of data during the October 1996 storm.

3.5.1 Wind-Driven Currents

The along-shelf momentum balance was primarily between the surface stress and bottom stress on the inner shelf (Figure 3-4). The vertical structure of the along-shelf current observed off Duck in October 1996 displayed a vertical structure typical of along-shore wind-driven circulation. Currents at all depths were directed south with down-coast winds, while current flow was northward with up-coast winds (Figure 3-1 and 3-3). The pressure gradients due to the coastal plume from the Chesapeake Bay played a minor, but important role (e.g., Rennie et al., 1999).

Predicted wind-driven currents were compared and correlated with currents observed at 13 m depth off Duck, NC, during October, 1996. Along-shelf currents predicted by bilinear eddy viscosity had the highest correlation with along-shelf currents. Similar correlations were found with or without the f_u term (>0.6 throughout the water column). In contrast, currents predicted by constant eddy viscosity had the highest correlations with observed across-shelf currents (~ 0.3 near the bed, ~ 0.8 near the surface). Constant eddy viscosity was inadequate for reproducing along-shelf velocity because constant A_z was too large near the bottom and consequently the resulting current shear was too small. However, bilinear eddy viscosity continues to increase away from the boundaries, reaching maximum in the center of the water column, which is unrealistic in the presence of stratification. In such cases, constant eddy viscosity may be a better representation of shear in the across-shelf direction. This may explain why across-shelf currents modeled with constant eddy viscosity were better correlated with the observed current than were the across-shelf currents modeled with bilinear eddy viscosity (Table 3-2).

The effect of stable stratification or otherwise damped turbulence is to reduce eddy viscosity, which in turn reduces the thickness of the layer of constant stress layer associated with the along-shelf wind. If the reduced Ekman layer thickness is no longer much greater than the water depth, Ekman transport to the right of the wind becomes

important, and the across-shelf wind is no longer expected to dominate across-shelf velocity. However, Lentz et al. (1999) found high correlations between $\partial v/\partial z$ and the across-shelf density gradient on the inner shelf off Duck. Thus even when A_z is small, $f v$ might not drive a strong across-shelf current because its depth-variation may be balanced in across-shelf momentum by the across shelf density gradient. This may explain why u_{x-wind} was better correlated with observed across-shelf currents outside of storm conditions than was u_{y-wind} (Table 3-2). Nearest the bed during storms, however, u_{y-wind} was better correlated with the observed across-shelf current than was u_{x-wind} . This is significant because currents nearest the bed during storms are presumably those most important to cross-shore sediment flux and associated morphologic change. u_{y-wind} occurs when $\partial v/\partial z$ creates a depth varying across-shelf Coriolis force which cannot be balanced by the across-shelf pressure gradient. During storms, $\partial v/\partial z$ is particularly strong very near the bed and may overwhelm the ability of $\partial p/\partial x$ to balance depth-varying Coriolis. Thus shear in the across-shelf current (i.e., u_{y-wind}) will be required very near the bed to complete the momentum balance. Further above the bed, $\partial v/\partial z$ is much smaller and depth variation in the Coriolis force is much weaker. Thus Coriolis can be more effectively balanced by $\partial p/\partial x$ and u_{y-wind} is less essential. Thus in the mid-water column, u_{x-wind} is relatively more important and logically better correlated with the observed across-shelf current.

There are notable limitations in the performance of the wind-driven current model. For example, bottom stress was generally underestimated. A probable reason for this is that the along-shelf pressure gradient was neglected in the model. The Chesapeake Bay plume, as documented by the NSF CoOP study (Rennie et al., 1999; Lentz et al., 1999), may be associated with significant along-shelf and across-shelf pressure gradients. Another reason the model underestimated bottom stress may be underestimation of the surface shear stress. Wind drag coefficients inferred by other investigators at Duck during storms have been 4-5 times larger than the drag coefficient predicted by Wo's (1982) formula (Madsen et al., 1993; Friedrichs and Wright, 1997; Lentz et al., 1999). Increased wind drag was attributed by other investigators to extreme wave conditions in

the depth-limited inner shelf environment.

Figure 3-10 compares the vertical structure of various components of the modeled across-shelf current to the observed across-shelf current (solid). To highlight the response of the various components, two separate cases (storm versus non-storm) with downwelling favorable winds were selected. Note that during the storm of October 1996, stratification was observed at the end of the FRF research pier, while water was well-mixed for the non-storm case (Figure 3-11). The vertical structure of the observed across-shelf current velocities show two distinctive features during storm and non-storm periods. During the non-storm period of October 1996, the vertical current structure was two layered when responding to upwelling or downwelling favorable winds. This is consistent with previous observations (Lentz and Winant, 1986; Lee et al., 1989). During the storm when wind was downwelling favorable, the vertical structure was three or four layered (Figure 3-10). At the water surface during the storm, the current was directed onshore. Two or three meters below the surface, the current changed its direction toward offshore with its maximum about 4 m below the surface. At about half the water depth, the across-shelf current turned again toward onshore. Sometimes very near the bed, the current was directed offshore, exhibiting a four layered vertical structure. It is uncertain why there existed a four-layer vertical structure, but it may be associated with stratification caused by the low-salinity Chesapeake Bay plume. Two possibilities are an internal bottom Ekman layer at the pycnocline (e.g., Ott and Garrett, 1998) or three-layer cross-shelf estuarine circulation (e.g., Hansen and Rattray, 1972).

In general, there exists significant disagreement between observed and modeled current velocity, particularly in the across-shelf direction. A source of observational error is ambiguous along-shelf rotation (See Figure 3-3). However, insufficiently sophisticated eddy viscosity associated with stratification, poorly constructed along- and across-shelf pressure gradients, and wave-induced mean currents are probably all large sources of error.

3.5.2. Waves and Wave-Driven Currents

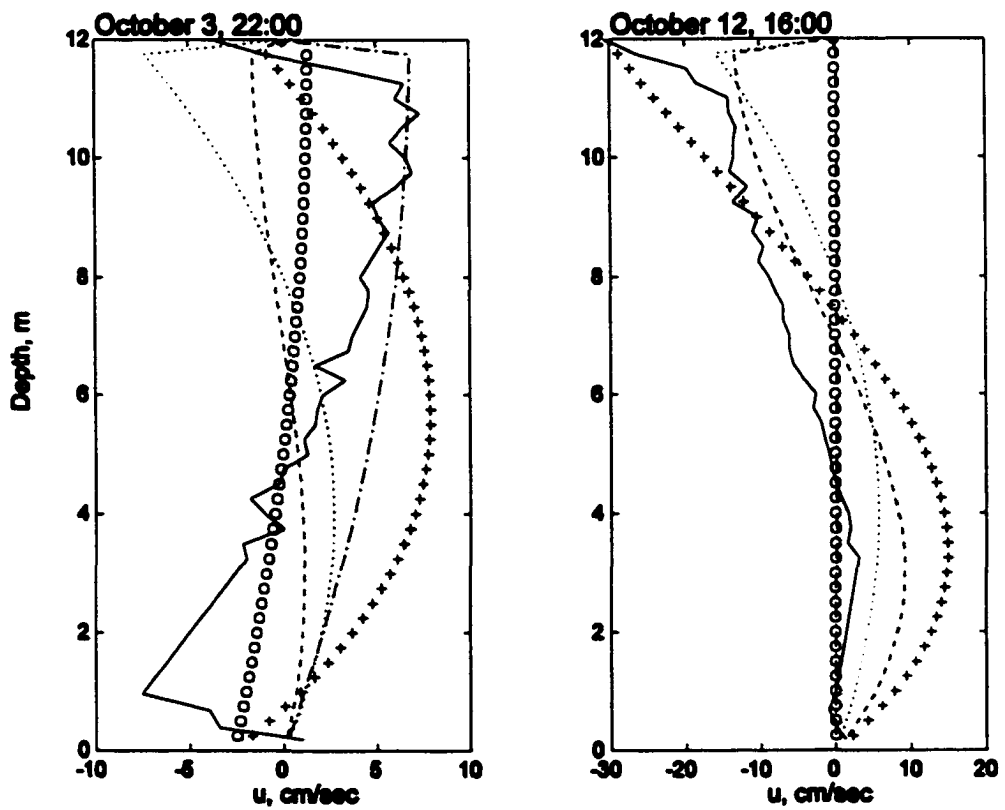


Figure 3-10. Vertical structure of u -components with downwelling favorable winds. Left panel shows the vertical structure during a storm, while the right panel is from a non-storm period. Solid - observed; dash - $u_{x\text{-wind}}$; dot - $u_{y\text{-wind}}$; dash-dot - return; circle - streaming; plus - total.

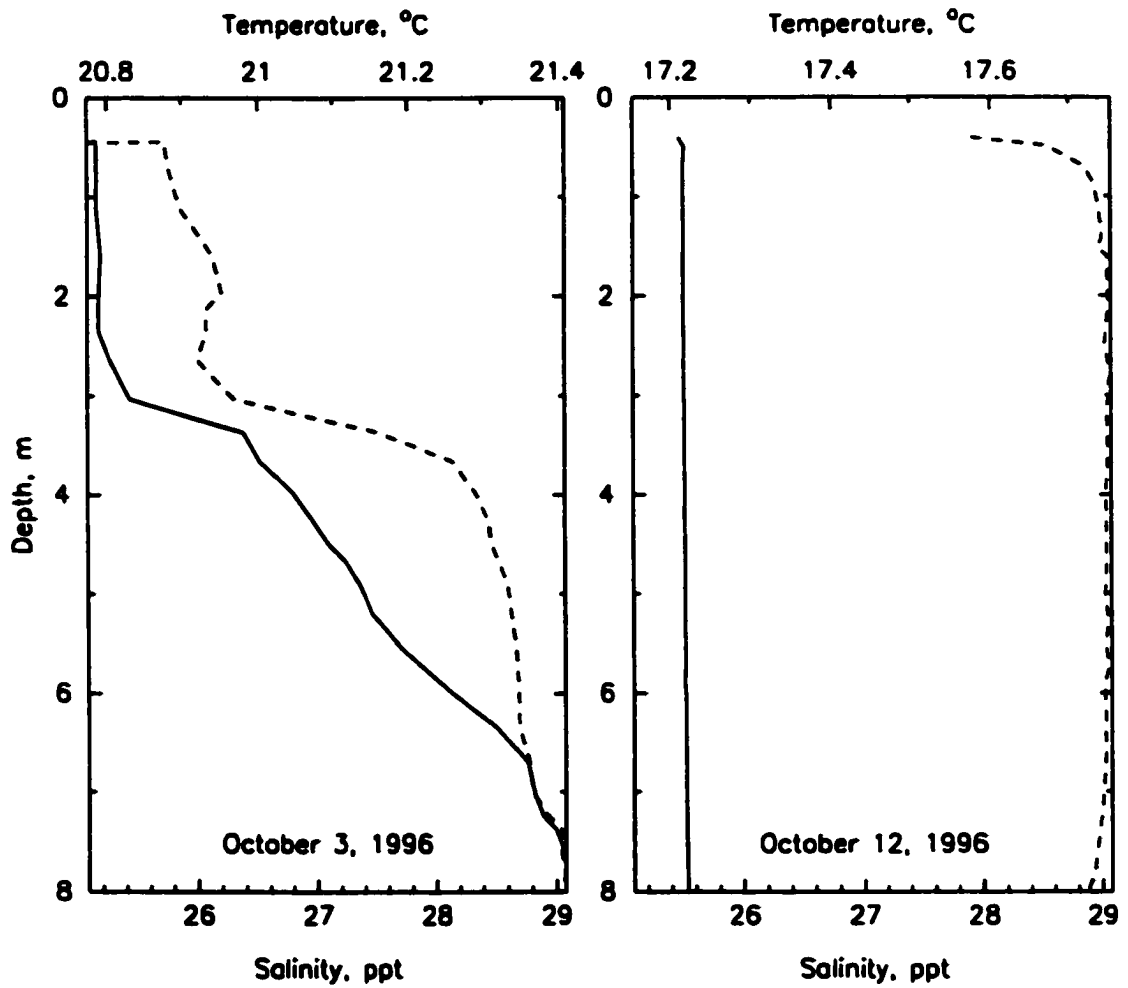


Figure 3-11. Vertical structure of salinity and temperature observed at the end of the FRF pier during storm and non-storm period. Note that depth increases from the water surface to bottom. Solid - salinity; dash - temperature.

Simple wave transformation across the inner shelf was modeled, including shoaling and refraction effects. Wave transformation reasonably predicted observed waves in terms of both magnitude and direction (Figures 3-8 and 3-9). However, near-bottom orbital velocity was overpredicted during the storm of October 1996, perhaps because energy dissipation due to bottom friction was not considered in the wave transformation. Wave asymmetry was modeled using Stokes second-order theory. Although wave velocity predicted by the Stokes second-order approximation provided wave asymmetry, it may have inadequately represented the actual asymmetry present. This is problematic since wave asymmetry may have important ramifications with regard to shoreward sediment transport (Niedoroda et al., 1985; Wright et al., 1991).

Simple analytical solutions were found for wave-driven currents associated with Stokes return flow and boundary layer streaming. Wave-driven currents are weak offshore and during low energy conditions (Figure 3-10b), but they are predicted to become dominant towards shore and during high wave energy conditions such as those which occurred during the October 1996 storm (Figure 3-10a). Inclusion of wave-driven currents for the entire study period does not generally improve the modeled cross-shelf currents throughout the water column (Table 3-2). However, inclusion of u_{stream} does increase correlations near the bed slightly and cause the current to turn shoreward very near the bed, as observed during the peak of the October 1996 storm. If only the non-storm period is considered, correlations improve near the bed with the inclusion of u_{return} . The boundary layer streaming solution may be inadequate because it assumes eddy viscosity within the boundary layer does not vary with time. Trowbridge and Madsen (1984a,b) showed that if eddy viscosity varies over individual waves then u_{stream} will also vary as a function of bottom roughness and may be negligible or even directed onshore. However, a time-dependent eddy viscosity for the wave boundary layer is beyond the scope of this study. Xu and Bowen (1994) suggested an alternate solution for u_{return} , such that u_{return} is exactly opposite to the mean Lagrangian wave-induced velocity. However, applying Xu and Bowen's formulation for u_{return} does not improve the correlation between observed and modeled currents.

Lentz et al. (1999) recently showed that radiation stress contributes at lowest order to the depth-integrated cross-shelf momentum balance on the inner shelf off Duck. Although radiation stress is entirely balanced by an associated cross-shelf pressure gradient in a depth-integrated sense, a depth-dependent imbalance may exist (e.g., Putrevu and Svensen, 1993). An analytical solution for the depth-dependent flow driven by radiation stress associated with intermediate depth shoaling waves is presently under development (Friedrichs and Lee, in prep.).

IV. CROSS-SHORE SEDIMENT TRANSPORT MODELING AND ASSOCIATED MORPHOLOGICAL CHANGE ACROSS THE INNER SHELF DURING STORMS

4.1. INTRODUCTION

It has long been emphasized that onshore-offshore sediment exchange is not confined within the surf zone, but extends to the inner shelf (e.g, Niedoroda et al., 1985; Wright, 1987; Lee et al., 1998). The inner shelf not only serves as a pathway for across-shelf sediment transport, linking the surf zone to the mid and outer shelf, but also modulates the hydrodynamic forcings that drive surf zone processes (Wright, 1995). If one is interested in modeling changes in profile configuration or shoreline movement, it is important to understand sediment transport processes over the inner shelf. For example, through analysis of beach-nearshore profiles collected over 11 years at Duck, NC., Lee et al. (1998) found that sediments usually accreted on the inner shelf (5-9 m depths) during or immediately after large storms. During intervening periods, the inner shelf gradually lost sediments, feeding sands onshore. These two processes of morphologic change, namely accretion during storm events followed by steady onshore transport, appear to play an important role in the long-term profile evolution at Duck, NC. However, the sediment source for and physical mechanisms driving accretion on the inner shelf during storms has yet to be established. This question motivated the present study that attempts to understand and predict sediment transport on the inner shelf.

The most commonly applied process-based models for suspended sediment transport in combined wave and current environments are energetics (Bagnold, 1963; Bowen, 1980; Bailard, 1981) and Rouse-type models (Smith, 1977; Grant and Madsen, 1986; Glenn and Grant, 1987). Energetics-type models are depth integrated and time-

dependent, whereas Rouse-type models are depth-resolving and time-averaged. These two models were originally formulated and calibrated for different marine environments. The energetics model was developed for application to the surf zone and stresses the importance of instantaneous orbital velocity in the absence of strong wind-driven currents. The Rouse-type model was developed for use in mid-shelf environments where mean currents often dominate sediment transport and wave asymmetry is often unimportant. Since the inner shelf is the region of transition between the mid-shelf and surf-zone, both models have advantages in this region.

The energetics model is based on the original idea of Bagnold (1963) that a proportion of fluid energy is expended in maintaining a sediment transport load. Bowen (1980) first applied this concept to cross-shore sediment transport using Bagnold's (1963) formulae for bed- and suspended load transport. Bailard (1981) re-derived these formulae and gave the notation commonly used now. Guza and Thornton (1985) analyzed the effect of randomness and nonlinearity of waves on the velocity moments. Reolvink and Stive (1989) included the effect of long waves and breaking-induced turbulence. The strengths of the energetics model lie in its simplicity, its ability to include wave-driven sediment flux, and its ability to provide a quick first estimate of the sediment transport. Since the energetics load is a simple power function of the near bed velocity, sediment transport can be described by a linear combination of velocity moments, sediment parameters and the bottom slope. However, all the physics is incorporated in the coefficient of proportionality between fluid energy dissipation and sediment transport rate. The goal of the present study is to apply a practical sediment transport model based as closely as possible to physical first principles. Therefore, the energetics model will not be applied to estimate suspended sediment transport in this investigation.

Wright et al. (1991) used both observations and Bailard's energetics formulation to compare the relative contributions to sediment transport across the inner shelf of 1) incident waves, 2) long-period oscillations, 3) mean flows and 4) gravity. They examined the above mechanisms for fairweather, moderate energy, swell and storm conditions on the inner shelf of the Middle Atlantic Bight. Their results showed that mean flow was

dominant, causing offshore flux during storms, and contributed significantly to onshore and offshore flux during fairweather and moderate energy. Incident waves were the major source of bed shear stress and caused either onshore or offshore sediment fluxes depending on the bottom morphology. However, waves caused strong onshore advection of sediment during swell. Low-frequency waves and gravity made only secondary contributions to cross-shore sediment flux.

Depth-resolving models for suspended sediment transport under combined waves and currents have been developed mainly for application outside the surf zone, where waves agitate the bottom primarily during large storms accompanied by significant wind-driven currents (e.g., Madsen et al., 1994). They have also been applied to the nearshore environments successfully (e.g., Brøker Hedegaard et al., 1991). In terms of steady, periodic and random components, sediment flux in depth-resolving models can be written as:

$$\langle q_x \rangle = \int_z (\bar{u}\bar{C} + \tilde{u}\tilde{C} + \overline{u'C'})dz \quad (4-1)$$

where \bar{u} , \tilde{u} , and u' , and \bar{C} , \tilde{C} , and C' represent mean, wave and turbulent components of flow velocity and concentration, respectively. The last term, $\overline{u'C'}$, in (4-1) is generally expected to be small (Nielsen, 1992). Under some conditions on the inner shelf, across-shelf transport due to the second term in (4-1) has been shown to be larger than transport due to the first term, most often under swell or fairweather conditions (e.g., Traykovski et al., 1999). However, previous work has shown mean transport to generally dominate total sediment transport across the shelf during storms (e.g., Wright et al., 1991).

Depth-resolving models which consider only the first term in (4-1) generally predict the time-averaged suspended sediment concentration profile using the Rouse-type equation. Assuming steady state and negligible horizontal advection, suspended sediment concentration in the Rouse-type model is determined by a diffusive process such that upward sediment flux by turbulent diffusion is balanced by downward flux due to gravitational settling (see Eq. 2-3). A common assumption in turbulent diffusion is that

sediment eddy diffusivity equals eddy viscosity. In the previous chapter, the Rouse-type equation with eddy viscosity linearly increasing up to a few 10's of cm above the bed was shown to predict suspended sediment concentration well. Many studies of sediment transport on the continental shelf have successfully employed the Rouse-type model (e.g, Glenn and Grant, 1987; Madsen et al., 1994; Wiberg et al., 1995)

Near-bed sediment transport under waves and currents is generally described with bedload transport formulae. Originally formulated for steady currents, bedload transport formulae have been applied to coastal environments by assuming that the instantaneous intra-wave transport rate is a function of the instantaneous bed shear stress or the instantaneous velocity above the wave boundary layer. However, bedload transport is not well understood in terms of depth-varying sediment velocity distribution and concentration distribution in the bedload layer (Nielsen, 1992).

The most common approach for estimating bedload transport is to assume a transport formulae of the form (Nielsen, 1992)

$$\Phi_b \sim (\theta' - \theta_c)^{1.5} \quad (4-2)$$

where Φ_b is the dimensionless bedload flux, θ' is the Shields parameter, and θ_c is the critical Shields parameter. The physically-based Shields parameter, which is proportional to velocity squared, is derived using dimensional scaling arguments which balance hydrodynamic drag on sediment against gravitational resistance. Using (4-2), Traykovsky et al. (1999) reported that in the summer on the inner shelf off New Jersey, the predicted bedload transport rate dominated observed suspended sediment transport and was consistent with the observed ripple migration rate. The energetics-based formula for bedload transport has a form which is also proportional to velocity cubed and, when calibrated, is effectively identical to (4-2). Wright et al. (1991) compared sediment transport predicted by energetics formulae for bedload and suspended load on the inner shelf off Duck, NC. during storms and concluded that the suspended load was probably much greater than the bed load.

To date, physically-based models of sediment transport which have been applied to morphological change on the inner shelf or shoreface have been forced either with

observed velocities (e.g., Gallagher et al., 1998), by modeled wind-forced currents (e.g., Zhang et al., 1999), or by modeled wave-driven processes (e.g., Stive and de Vriend, 1995). Models of morphological evolution under development which will attempt to include both wave and wind-driven processes appear to be computationally intensive numerical approaches with aims at engineering predictions, rather than physical understanding of dominant underlying forcing (e.g., de Vriend et al., 1993). Thus a major goal of the present study is to implement the simplest physically-based models possible to morphological change which include both wave- and wind-driven sediment transport across the inner shelf. The specific objectives are;

2. Incorporating the resulting predictions for currents and waves into the simplest possible physically-based models for sediment flux which adequately represent the dominant modes of sediment transport across the inner shelf.
3. Using resulting output from sediment transport models to predict changes in bed elevation across the inner shelf during a series of significant storms and comparing that output with existing observations of morphologic change.
4. Determining and understanding which components of hydrodynamic forcing and resulting sediment transport are predicted and observed to be most significant to morphological change on the inner shelf of the Middle Atlantic Bight and why.

The organization of this paper is as follows:

First, section 2 overviews field data used to force and calibrate the sediment transport model. Sediment transport, including suspended sediment and bedload, are modeled in section 3. The morphologic change model along with morphologic response during storms are described in section 4. The results are discussed in section 5. Finally, section 6 presents the conclusions of the study along with a discussion of the study's limitations.

4.2. FIELD DATA

In the 1D model for sediment transport and morphological change, inputs are wind and waves at one location, initial bathymetry and sediment size distribution along a

profile across the inner shelf, while outputs are waves, currents, suspended sediment concentration, sediment flux and bottom change along that same profile. Two data sets from Duck, N.C., are utilized in this study: data from a bottom boundary layer tripod deployed in October 1996 are used in developing the sediment transport model, and a multi-storm data set from the Field Research Facility data base is used to test the likely contribution of various transport components to morphological change on the inner shelf.

4.2.1. Field Site

The U.S. Army Corps of Engineers Waterways Experiment Station, Field Research Facility (FRF) is located on the Outer Banks of North Carolina (see Figure 2-1). The study area has characteristics typical of the US east coast in terms of sand grain size, wind climate and storm exposure (Birkemeier et al., 1985). The shoreline is straight and the bottom topography is regular over the inner shelf.

The right-handed coordinate system is adopted in this study: the onshore-offshore component (+ offshore) was taken to be the x-axis, while the along-shore component (+ upcoast) was taken to be the y-axis. The z-axis increases upward from the sea bed, unless stated otherwise. The shoreline at Duck is oriented 20° west of true North (Figure 2-1) and directions of the wind, waves and current were referenced to the shoreline. The directions of the wind and waves indicate where they are coming from, while current direction indicates where it is flowing toward.

4.2.2. Bathymetry

The initial bathymetry from 6 m to 20 m depths was taken from the Office of Naval Research CoOP bathymetry data set. Landward of 6 m, bathymetry was supplemented by the FRF beach-nearshore profile survey, selected from a non-barred profile. The alongshore coordinate of the bathymetry corresponds to FRF profile survey line 62, which is about 500 m north from the FRF research pier. This alongshore location

was selected because not only the VIMS tripod was deployed along this coordinate, but also many FRF measurements, including wave, beach-nearshore survey and sediment sampling, were performed along this coordinate. The across-shelf bathymetric grid is spaced at 200 m intervals from 200 m to 5000 m offshore, comprising 25 grid points (Figure 4-1). There exists a break in slope at about 13 m depth, the slope landward of the break being steeper (0.005) compared to the slope seaward of the break (0.002). Note that the slope of the beach face is much steeper (0.06).

Data on morphological change is available from repeated profiles between 1981 and 1993. Over this period, the beach-nearshore profile data have been collected approximately biweekly along four profile lines (lines 58, 62, 188 and 190). Offshore distance is measured relative to a shore parallel baseline located behind the dune system and elevation is referenced to the 1929 National Geodetic Vertical Datum. Two pairs of profile lines (58 and 62, 188 and 190) are separated about 500 m from the FRF research pier to minimize the influence of localized scour near the pier (Miller et al., 1983). Each profile line extends from the dune to approximately 9-m depth (900 m offshore from the shoreline). Howd and Birkemeier (1987) and Lee and Birkemeier (1993) tabulated the profile data and discussed survey methods, errors, and accuracy in detail.

4.2.3. Sediment

Surficial bottom sediment size distribution for each grid point was obtained from two sources: FRF and VIMS. The FRF collected surface sediment grab samples from the dune crest to 8-m depth (about 1000 m offshore) along profile line 62 over a period of 18 months between March 1984 and September 1985. Sediment size distributions for the collected samples are reported in Stauble (1992). For this study, the sediment samples were grouped by offshore distance corresponding to the bathymetric grid, and sediment sizes were averaged to minimize temporal and spatial variability. Sediment size

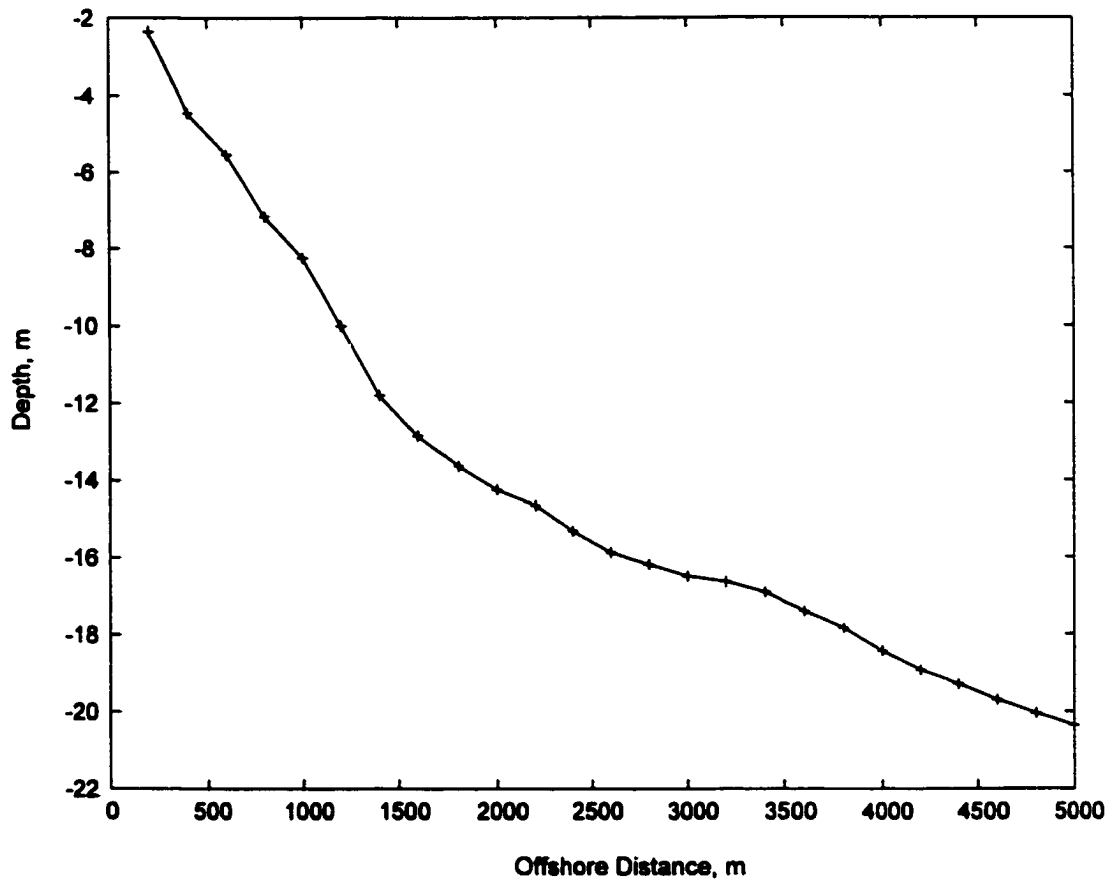


Figure 4-1. Input bathymetry. Pluses represent 25 model grid points.

information at deeper depth (> 9 m) comes from a sediment sample collected at 13 m depth at the beginning of the VIMS October 1996 experiment (See Ch. 2). The sediment size distribution at each grid is shown in Table 4-1. Bold indicates observed sediment size distribution and plain type indicates those taken from the nearest landward observation.

Suspended sediment concentration was measured in October 1996 by Acoustic Backscatter Sensors (ABSs), providing sediment concentration profiles from the bed to about 80 cm ab with a vertical resolution of 1 cm. A more detailed description of sediment concentration measured by the ABSs is found in Ch. 2.

4.2.4 Significant Storms

The time period that high quality FRF data sets for directional waves, wind and bathymetric change are available spans from 1987 to 1993. Only significant storms were chosen to examine morphodynamic response because only relatively large storms affect the shoreface (the seaward end of the FRF profile surveys) (Lee et al., 1998; Birkemeier et al., 1999). Significant storms between 1987 and 1993 were identified by using a partial-duration series of wave height applied to the entire wave record recorded by FRF gauge 630 between 1985 and 1997. The partial duration series is useful for estimating events of low recurrence interval from a short record (Dunne and Leopold, 1978). The partial-duration series consists of all events greater than some arbitrary base magnitude, usually the smallest of the annual-maximum series. The smallest maximum significant wave height in the annual-maximum series was 3.43 m, occurring on October 17, 1997.

Storm duration was computed from the time the wave height exceeded 3.0 m until the height fell below 2.35 m (the mean height over the entire wave record plus two times the standard deviation). The peak wave height, integrated wave power (intensity), and duration were computed for each storm (Table 4-2). A slightly different method to define a significant storm was employed in Birkemeier et al. (1999), but significant storms

Offshore Distance	Sediment Size Class in phi							
	m	> 2 pi	2-2.5	2.5-3	3-3.5	3.5-4	Silt	Clay
200	0.3165	0.3601	0.2728	0.0464	0.0042	0.0000	0.0000	0.0218
400	0.0678	0.2419	0.4916	0.1646	0.0336	0.0005	0.0000	0.0156
600	0.0157	0.0483	0.4969	0.3653	0.0718	0.0022	0.0000	0.0129
800	0.0075	0.0394	0.4475	0.4104	0.0920	0.0032	0.0000	0.0125
1000	0.0264	0.0133	0.2003	0.5639	0.1360	0.0200	0.0400	0.0110
1200	0.0264	0.0133	0.2003	0.5639	0.1360	0.0200	0.0400	0.0110
1400	0.0069	0.0190	0.2915	0.6003	0.0284	0.0323	0.0216	0.0120
1600	0.0069	0.0190	0.2915	0.6003	0.0284	0.0323	0.0216	0.0120
1800	0.0069	0.0190	0.2915	0.6003	0.0284	0.0323	0.0216	0.0120
2000	0.0069	0.0190	0.2915	0.6003	0.0284	0.0323	0.0216	0.0120
2200	0.0069	0.0190	0.2915	0.6003	0.0284	0.0323	0.0216	0.0120
2400	0.0069	0.0190	0.2915	0.6003	0.0284	0.0323	0.0216	0.0120
2600	0.0069	0.0190	0.2915	0.6003	0.0284	0.0323	0.0216	0.0120
2800	0.0069	0.0190	0.2915	0.6003	0.0284	0.0323	0.0216	0.0120
3000	0.0069	0.0190	0.2915	0.6003	0.0284	0.0323	0.0216	0.0120
3200	0.0069	0.0190	0.2915	0.6003	0.0284	0.0323	0.0216	0.0120
3400	0.0069	0.0190	0.2915	0.6003	0.0284	0.0323	0.0216	0.0120
3600	0.0069	0.0190	0.2915	0.6003	0.0284	0.0323	0.0216	0.0120
3800	0.0069	0.0190	0.2915	0.6003	0.0284	0.0323	0.0216	0.0120
4000	0.0069	0.0190	0.2915	0.6003	0.0284	0.0323	0.0216	0.0120
4200	0.0069	0.0190	0.2915	0.6003	0.0284	0.0323	0.0216	0.0120
4400	0.0069	0.0190	0.2915	0.6003	0.0284	0.0323	0.0216	0.0120
4600	0.0069	0.0190	0.2915	0.6003	0.0284	0.0323	0.0216	0.0120
4800	0.0069	0.0190	0.2915	0.6003	0.0284	0.0323	0.0216	0.0120
5000	0.0069	0.0190	0.2915	0.6003	0.0284	0.0323	0.0216	0.0120

Table 4-1. Sediment size distribution at various depths. Observed sediment size distributions are in bold. Stations without direct measurements use the nearest directly observed location.

between 1987 and 1993 were essentially the same for both methods. 27

Storm Peak	Date				H _{ms} m	Wave Power Joule	Duration Hour	Volume Change	
	FRF Profile Survey		Storm based on Wave					Total m ³ /m	Shoreface m ³ /m
	Start	End	Start	End					
870126	870123	870213	870125	870129	3.65	1.77E+06	16.05	126.08	3.20
870217	870213	870219	870215	870220	5.07	5.61E+06	48.00	-7.36	10.16
870310	870303	870318	870310	870317	4.85	9.63E+06	76.78	16.94	34.32
870425	870402	870430	870425	870429	3.92	4.59E+06	39.50	-14.06	24.83
880413	880401	880518	880412	880416	5.20	5.95E+06	36.00	18.69	6.74
890224	890221	890227	890222	890225	4.63	5.49E+06	36.24	73.16	50.05
890307	890227	890312	890306	890313	4.29	1.16E+07	88.30	33.82	60.52
891209	891207	891212	891207	891211	4.15	5.95E+06	44.52	-12.65	13.20
891224	891221	891228	891221	891226	5.63	7.58E+06	45.71	46.35	49.65
901026	901015	901031	901025	901028	4.71	3.82E+06	28.95	29.14	5.34
901110	901031	901115	901108	901111	3.65	3.57E+05	3.66	-38.64	-6.26
910420	910327	910422	910418	910421	3.50	1.05E+06	11.64	6.26	-25.57
910818	910813	910823	810818	910820	4.83	8.35E+05	5.03	27.71	21.24
911031	911023	911103	911026	911102	5.93	1.34E+07	82.75	30.98	-37.83
911109	911103	911112	911107	911112	4.86	5.05E+06	31.55	-34.58	18.92
920104	920102	920124	920102	920106	4.34	4.74E+06	36.19	4.30	4.64
920326	920325	920330	920325	920328	3.91	1.43E+06	13.14	-47.67	11.16
920507	920504	920511	920505	920509	3.89	3.52E+06	31.95	14.00	15.28
920925	920921	920926	920923	920927	4.58	4.67E+06	32.22	28.97	24.34
921005	920926	921026	921004	921010	4.56	4.70E+06	37.36		
921214*	921026	921218	921208	921217	4.73	1.33E+07	83.70	-18.63	12.18
930110	930104	930113	930108	930113	3.89	4.90E+06	41.68	-4.68	-9.34
930313	930312	930315	930312	930314	4.64	2.52E+06	11.74	-8.00	53.11
930406	930315	930412	930405	930410	4.20	5.46E+06	52.11	-4.47	-9.03
931027	931015	931029	931026	931028	4.73	2.57E+06	18.60	18.60	-0.59
931128*	931122	931129	931123	931203	4.12	4.00E+06	36.40	-32.70	5.43
931217	-	-	931211	931219	3.85	4.02E+06	40.71		

* Two storms occurred within a day and there were no profile survey between them.; - No profile survey

Table 4-2. Significant storms identified between 1987 and 1993.

significant storms were identified between 1988 and 1993. Two storms out of 27 storms are not considered further because the December 12, 1993 storm did not have corresponding profile survey data and wind data were not available during the August 4, 1988 storm. There were two occasions that two storms occurred successively in a couple of days with no profile survey in between. Thus each pair of storms was treated as one storm, as indicated by an asterisk in Table 4-2.

4.3. SEDIMENT TRANSPORT MODEL

4.3.1. Suspended Sediment

Prediction of wave-averaged sediment suspension was described in Ch. 2 in detail. Estimation of benthic boundary layer structure used the GMG model with linearly increasing eddy viscosity. The GMG model requires current velocity at a reference height (usually 1 m ab), near-bottom wave orbital velocity, and wave period and angle between waves and currents. Waves and currents were modeled as described in the previous chapter, with (3-22) used for the along-shelf current and (3-25), (3-26), (3-44) and (3-45) used for the across-shelf current. It is noted that accurate prediction of the magnitude and direction of the across-shelf current becomes very important in estimating sediment flux and resultant bottom change. However, the across-shelf current is secondary in predicting benthic boundary layer structure and sediment suspension, because the total current vector is used in the GMG model and along-shelf currents become dominant during extra-tropical storms at Duck.

Figure 4-2a compares maximum shear velocity due to combined waves and currents, u_{*cw} , predicted by the GMG model, using the observed waves and current and the predicted waves and current. Figure 4-2b does the same for skin friction shear velocity (u_{*sf}) which does not include drag from bed forms and is more directly important in determining the reference concentration. During the storm period, u_{*cw} and u_{*sf} obtained using the predicted waves and current overestimated u_{*cw} and u_{*sf} using the

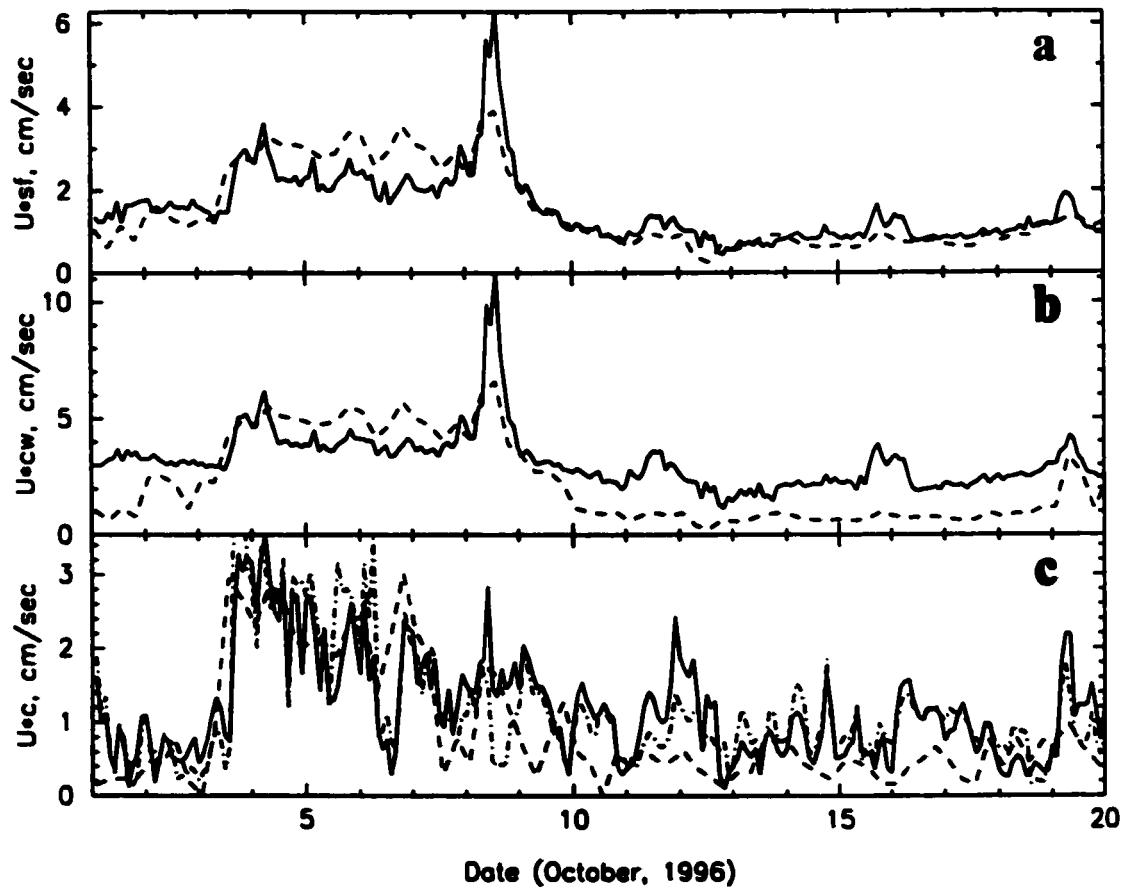


Figure 4-2. Comparison of shear velocities using the GMG model with observed currents and waves (solid) and predicted currents and waves (dash) at 13-m depth. a) skin friction shear velocity; b) shear velocity due to the combined effect of waves and currents; and c) shear velocity due to currents outside the wave boundary layer. Note that dot-dashed line in c) is shear velocity due to currents obtained by log-fitting observed currents.

observed waves and current. This may result from the model overestimating u_b during the storm (see Figure 3-8). In Figure 4-2c, shear velocity due to the current, u_{*c} , estimated using predicted waves, currents and the GMG model is compared to u_{*c} estimated by fitting the observed current to a log-profile. The current velocity was underpredicted in the current model, causing model u_{*c} to be generally lower than observed u_{*c} .

Wave-averaged suspended sediment concentration was calculated using a Rouse-type equation (2-16). The seven grain sizes used in the model are shown in Table 4-1, and a mixing depth was incorporated as described in Ch. 2. Enhanced vertical exchange due to vertical advection by wave-induced vortices, present when the current was relatively weak, was incorporated via a thickened wave boundary layer. The criteria for the time of enhanced vertical exchange was the R-value as discussed in Ch.2. Figure 4-3 presents the observed and predicted suspended sediment concentration at 5 and 20 cm ab. The model predicts the observed concentration well. Overestimation of predicted concentration at 20 cm ab during the storm may be due to the overestimation of u_b and associated shear velocities.

Wave-averaged suspended sediment fluxes for each component of wind- and wave-driven currents at heights of 36 cm ab are shown in Figure 4-4. $u_{x-wind}C$, $u_{y-wind}C$ and $u_{return}C$ are directed offshore with relatively small magnitude. $u_{stream}C$ is the dominant component and directed onshore. Because of dominance of $u_{stream}C$, total suspended sediment flux was directed onshore and the magnitude of sediment flux is comparable to observed suspended sediment flux. Overestimation of suspended sediment flux in the middle of the storm may be due to overprediction of shear as pointed out earlier. Figure 4-4 also displays observed wave-induced suspended sediment flux (i.e., the correlation of u and C over the course of individual bursts). The wave component is much smaller than the mean component, and modeling its depth dependence with respect to wave phase is problematic. Thus wave-driven suspended sediment transport is neglected in this study.

4.3.2. Bedload

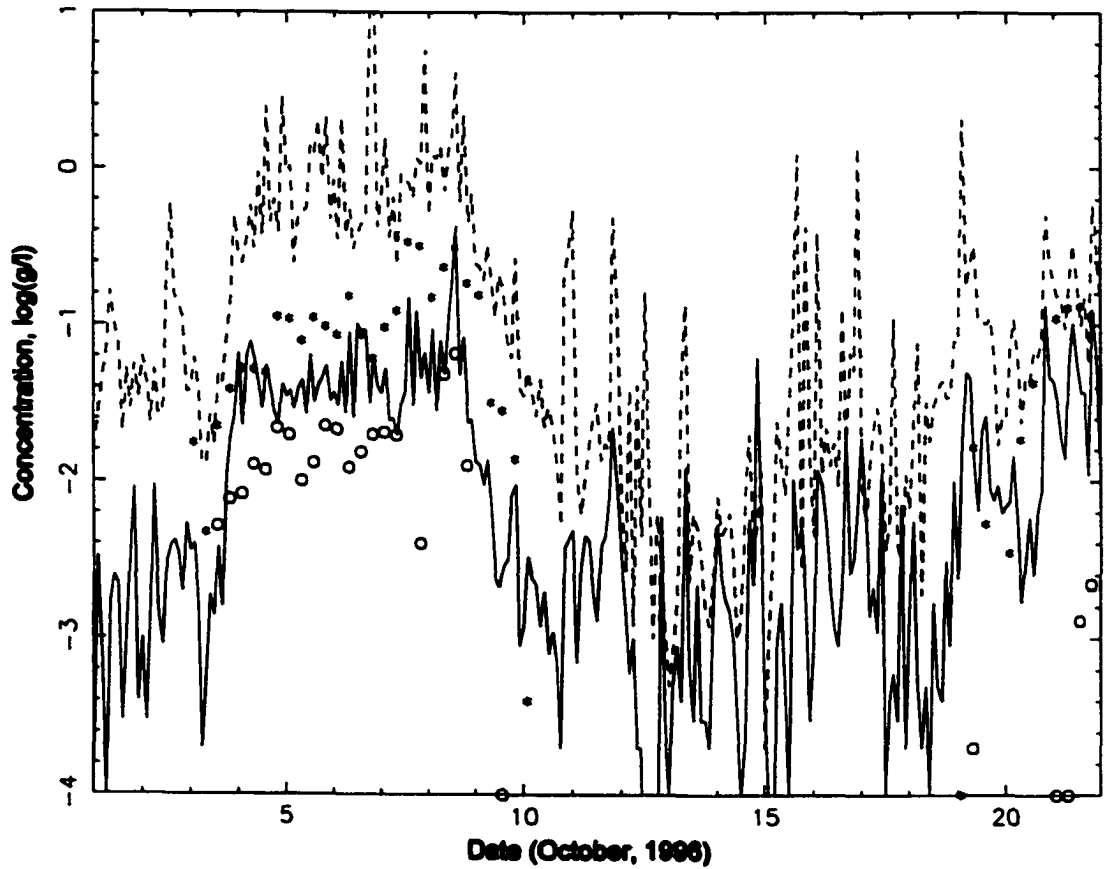


Figure 4-3. Suspended sediment concentration at 5 and 20 cm ab using observed waves and currents (dash - 5 cm ab; solid - 20 cm ab) and predicted waves

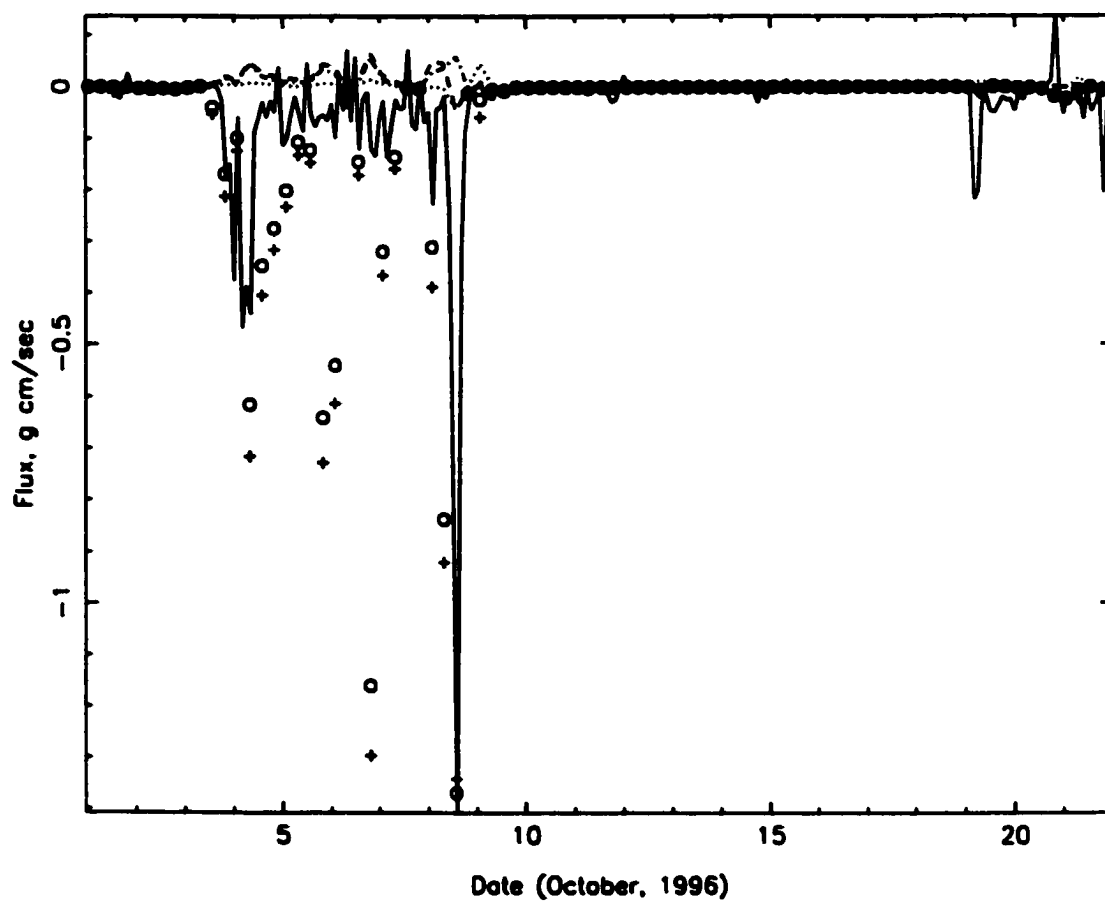


Figure 4-4. Wave-averaged suspended sediment flux for u_{x-wind} , u_{y-wind} , u_{return} and u_{stream} components along with observed sediment flux. Solid - observed; dash - u_{x-wind} ; dot - u_{y-wind} ; dash-dot - u_{return} ; plus - u_{stream} ; circle - total.

For the bedload sediment transport, the Meyer-Peter and Müller (1948) equation was adopted because this semi-empirical expression is widely used and is consistent with the mixing depth concept used in the previous chapter. In order to obtain fractional bedload sediment transport, the Meyer-Peter and Müller formula was modified using the grain size parameter, following Sleath's (1978) approach. The bedload transport rate, $q_{b,i}$, is then given by

$$\begin{aligned}\Phi_{b,i} &= \frac{q_{bl,i}}{\rho_s d_{si} \sqrt{g d_{si} (s-1)}} \\ &= 8(|\theta_{w,i}^{sf}| - \theta_{cr,i})^{1.5} \frac{\theta_{w,i}^{sf}}{|\theta_{w,i}^{sf}|} \quad \text{for } |\theta_{w,i}^{sf}| > \theta_{cr,i} \quad (4-3a)\end{aligned}$$

$$= 0 \quad \text{for } |\theta_{w,i}^{sf}| < \theta_{cr,i} \quad (4-3b)$$

where $q_{bl,i}$ is the bedload flux in g/cm s for sediment size class, d_{si} , $\theta_{w,i}^{sf}$ is the wave skin friction Shields parameter, and $\theta_{cr,i}$ is the critical Shields parameter. The quantity $|\theta_{w,i}^{sf}| - \theta_{cr,i}$ is the excess Shields parameter above the critical threshold. The wave skin friction Shields parameter, extended to spectral waves with non-zero skewness, is (Nielsen, 1992)

$$\theta_{w,i}^{sf}(t) = \frac{0.5 f_{2.5} \sqrt{2} u_b u_w(t)}{g d_{si} (s-1)} \quad (4-4)$$

where $u_w(t)$ is instantaneous wave velocity and $f_{2.5} = \exp[5.213(2.5d_{si}/A_b)^{0.194} - 5.977]$ is the grain roughness wave friction factor.

For modeling purpose, u_w was specified using (3-28). Under regular sine waves, however, the net transport rate due to waves becomes zero. Thus, wave asymmetry was incorporated into u_w using the Stokes second-order approximation given by (3-30).

Figure 4-5 displays wave-forced across-shelf bedload transport predicted by (4-3) and (4-

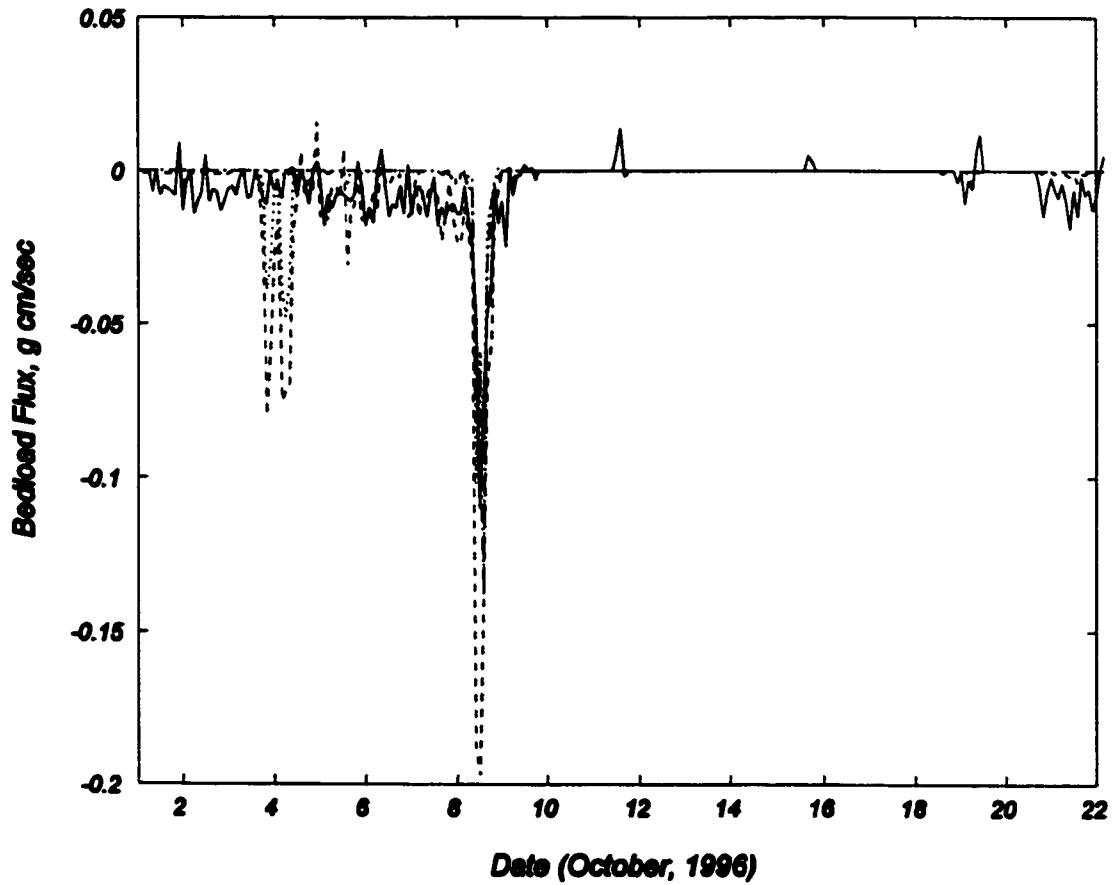


Figure 4-5. Comparison of bedload transport. Solid - wave-forced bedload transport using observed instantaneous wave velocity; dash - current-enhanced bedload transport using observed instantaneous wave velocity; dot - wave-forced bedload transport using Stokes second order wave velocity; dash-dot - current-enhanced bedload transport using Stokes second order wave velocity.

4) using observed instantaneous wave velocity (solid) and using modeled u_w including Stokes asymmetry (dot). Prediction of the magnitude and direction of transport based on a bedload formula similar to (4-3) was reported to be consistent with the observed ripple migration rate at the inner shelf (13-m depth) in New Jersey (Traykovski et al., 1999). Traykovski et al. (1999) reported that the numerical constant in (4-3) was generally greater than 8, perhaps because a portion of the transport incorporated into ripple migration occurs as near-bed suspended load. Nielsen (1992) also found a scaling constant larger than 8 for high stress conditions ($\theta > 1$) and reasoned that it is likely due to the rapidly increasing rate of suspended transport. This study adopted the original constant of 8, resulting in a conservative estimate bedload transport rate.

To test the possible role of bedload under combined waves and currents, (4-3) was modified to

$$\theta_{w,i}^{sf}(t) = \frac{0.5f_{cw}|u_\delta|u_\delta(t)}{gd_{si}(s-1)} \quad (4-5)$$

where $u_\delta(t)$ is the vector sum of the near-bottom orbital velocity and the steady current at the top of the wave boundary layer, and f_{cw} is the combined wave-current friction factor from the GMG model (f_{cw} is nearly equal to $f_{2.5}$). The steady current at the top of the wave boundary layer was also given by the GMG model.

Figure 4-5 also displays the across-shelf component of current-enhanced bedload transport predicted by (4-3) and (4-5) using observed instantaneous wave and current (dash) and using modeled instantaneous wave and current velocity (dash-dot). Wave-forced and current-enhanced across-shelf bedload transport using observed waves were of similar magnitude during most of the storm, except when current was strong (October 3~4). When the current was strong (4-5) predicted significantly greater onshore transport. As described above, Traykovsky et al. (1999) reported that predicted bedload transport using (4-3) (i.e., no current contribution) was consistent with the observed ripple migration rate in magnitude and direction. Thus there exists field evidence for using the wave-forced bedload transport formula. Using modeled waves underestimates bedload

transport for both wave-forced and current-enhanced bedload transport. It may be that the Stokes second order approximation is inadequate to properly represent bedload transport by real waves.

4.4. MORPHOLOGIC CHANGE MODEL

4.4.1. Model Formulation

The basic structure of the inner shelf cross-shore morphodynamics model is described in Figure 4-6. The initial bathymetry was taken from an ONR survey collected during the CoOP experiment and is shown in Figure 4-1. The spatial scale in the across-shelf direction is about 5 km between the 2 m and 20 m depth contours. The field was equally divided into 25 cross-shelf grid points with one grid space being 200 m. The grid point at the seaward end was set to be the seaward boundary of the computational field. Hydrodynamics and sediment transport processes in the surf zone are different from those in the inner shelf and this model is specifically developed for the inner shelf. Thus, it would be problematic if the entire computational field were considered. Further, the surf zone expands seaward with increasing wave energy during a storm, and then retreats landward with decreasing wave energy. If the varying surf zone width were not considered, bottom change in the transitional zone could be biased by the time it was occupied by the surf zone. To circumvent this problem, the seaward-most break point was identified during a storm of interest before initializing the model, and the grid point at which the seaward-most breaker occurred was defined as the landward boundary. To conserve mass, bottom change at the landward boundary was allowed to propagate landward. The vertical grid for depth-integrating sediment flux is spaced exponentially ($\exp(i/10)/100$, where i is the i th grid point) from the bottom, resulting in 70 grid points at 13 m depth. To force the model, waves, currents and sediment fluxes were computed for the entire across-shelf as described earlier in this chapter.

In order to predict bottom profile change under varying hydrodynamic forcing, a

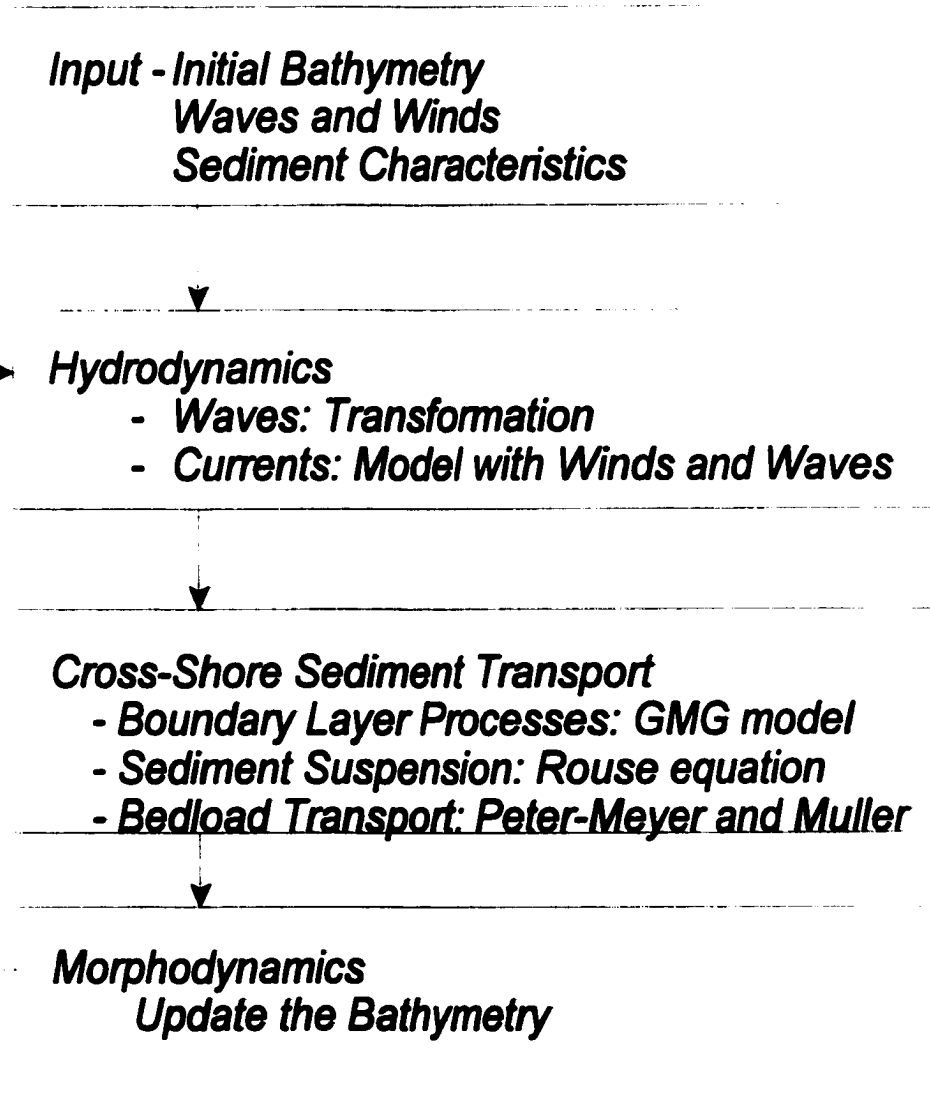


Figure 4-6. Basic structure of morphodynamics model.

change of bottom elevation, z_b , can be determined by employing continuity of sediment volume (e.g., Wright, 1995)

$$C_b \frac{\partial z_b}{\partial t} + \frac{\partial C_s}{\partial t} = -\nabla \cdot \bar{Q}_t \quad (4-7)$$

where C_b is sediment concentration in the bed, and \bar{Q}_t is the total sediment flux vector.

C_s is depth-integrated concentration of suspended sediment in the water column, given by

$$C_s = \int_z^h C_z dz \quad (4-8)$$

where C_z is suspended sediment concentration at any particular elevation, z , above the bed. Assuming bottom contours are straight and parallel, and the alongshore sediment flux, Q_y , is uniform such that $\partial Q_y / \partial y = 0$, (4-7) can be written as:

$$C_b \frac{\partial z_b}{\partial t} = -\left(\frac{\partial C_s}{\partial t} + \frac{\partial Q_x}{\partial x}\right) \quad (4-9)$$

The time-averaged horizontal volume flux is given by

$$Q_x = \int_z^h [u(z,t)C_z(z,t)]dz + Q_{bl} \quad (4-10)$$

where u is the across-shelf velocity and Q_{bl} is dimensionalized bedload transport. The temporal change of z_b can then be accounted for in terms of the time rate of change of depth-integrated sediment concentration, $\partial C_s / \partial t$, and the cross-shore sediment flux divergence, $\partial Q_x / \partial x$.

Morphodynamic models generally estimate bottom elevation based on predictions of cross-shore sediment flux alone (e.g., Nielsen, 1992):

$$C_b \frac{\partial z_b}{\partial t} = -\frac{\partial Q_x}{\partial x} \quad (4-11)$$

by assuming the local change of sediment concentration with respect to time contributes insignificantly to bottom elevation over time-scales of morphologic change. In this study,

(4-11) is solved via a difference equation using a backward difference scheme

$$C_b \frac{z_{bj}^{n+1} - z_{bj}^n}{\Delta t} = -\frac{Q_{xj}^n - Q_{xj-1}^n}{\Delta x} \quad (4-12)$$

where the superscript n represents the time step, the subscript j represents the spatial step, and Δt and Δx represent the increments of the time and spatial step, respectively. Q_x is determined by integrating (4-12) over the vertical grid at each horizontal grid point. The time step was set to 1200 sec to acquire a stable solution. If the time step is too large (4-12) becomes unstable (Naim and Southgate, 1993). To save computer time, the hydrodynamics were normally updated in (4-12) only every six hours, which is the standard interval for observed wind and wave data recorded by the FRF. However, if bottom change exceeded 0.5 cm at any across-shelf grid point between hydrodynamic updates, the hydrodynamic module was called with updated bathymetry and the most recent available wind and waves.

4.4.2. Application to October 1996

The inner shelf cross-shore morphodynamics model was initially applied to the October 1996 storm. Depth-integrated instantaneous across-shelf sediment fluxes for a downwelling favorable wind condition during the October 1996 storm are shown along the across-shelf grid in Figure 4-7. Components include $u_{x-wind}C$, $u_{y-wind}C$, $u_{return}C$, $u_{stream}C$, $Q_{b,w}$ (wave-forced bedload), and $Q_{b,cw}$ (current-enhanced bedload). Among suspended sediment fluxes, boundary layer streaming was the dominant component, directed onshore. The other wave-driven component, $u_{return}C$, was an order of magnitude smaller than $u_{stream}C$, and was directed offshore. Wind-driven components were weaker than wave-driven component and were directed offshore. $u_{y-wind}C$ was the weakest component. Bedload sediment fluxes were directed onshore and current-enhanced bedload was an

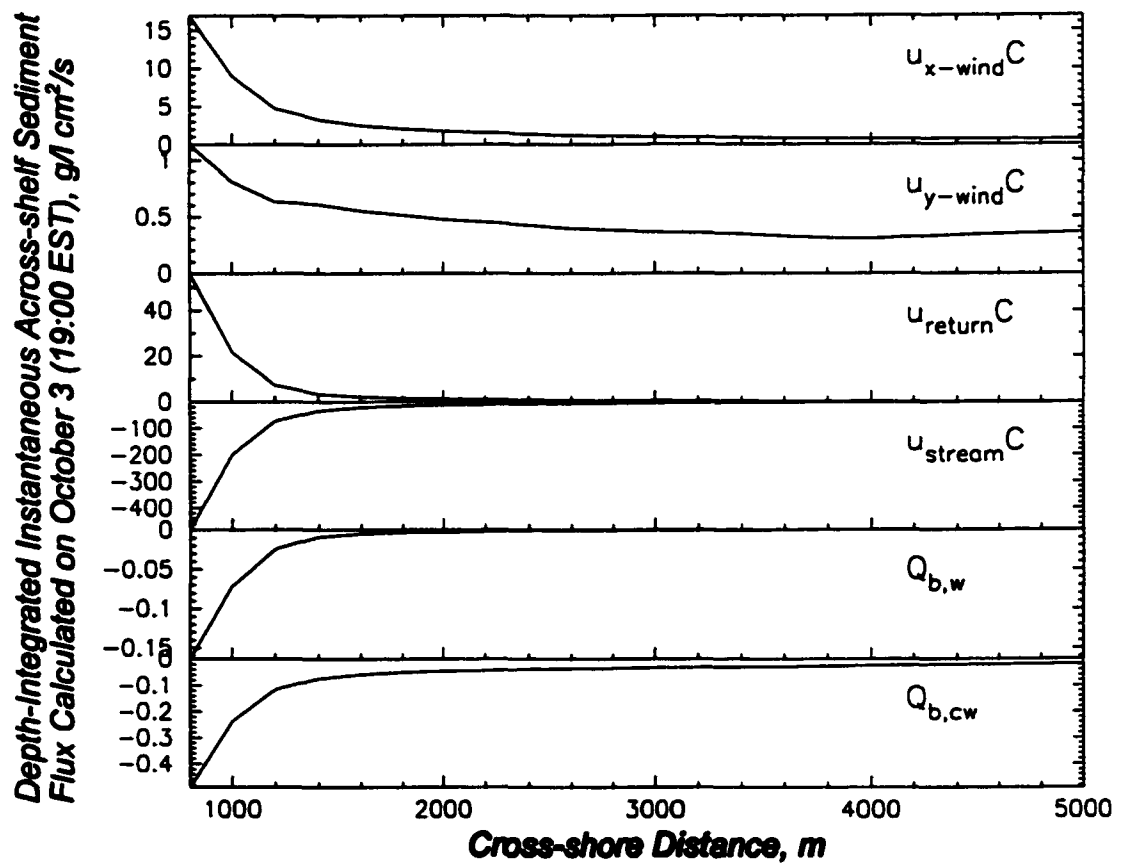


Figure 4-7. Depth-integrated instantaneous sediment flux along the across-shelf grid on October 3 (19:00 EST).

order of magnitude greater than wave-forced bedload flux.

A key feature of sediment flux across the inner shelf as illustrated in Figure 4-7 is that the magnitude of all components of suspended and bedload sediment flux increase rapidly landward of 1200 m offshore. This is because the magnitude of all components are positively related to water depth, mainly through the influence of u_b . For the suspended sediment components, the overall level of concentration is controlled by the reference concentration which, in turn, is related to u_b^3 through its dependence on the mixing depth (see Ch.2). Figure 4-8a shows across-shelf variation in u_b . Since u_b^3 increases dramatically landward of 1200 m where depth decreases sharply (see Figure 4-1), the magnitude of sediment flux also increases dramatically. The one component of across-shelf sediment flux which does not increase nearly as rapidly with decreased water depth is that associated with the along-shelf wind. u_{y-wind} (Figure 4-8b) is proportional to h^3 (see 3-25), and h^3 decreases rapidly toward shore. As water depth decreases, the relative importance of the Coriolis term to the across-shelf momentum balance decreases and the current vector induced by the along-shelf wind becomes oriented more completely in the along-shelf direction. The sediment flux component associated with u_{x-wind} increases somewhat more slowly than those associated u_{return} , u_{stream} or wave orbital asymmetry, u_{2b} , because u_{x-wind} (Figure 4-8b, Eq. 3-26) is proportional to h (which decreases slowly towards shore), whereas u_{return} , u_{stream} , u_{2b} (Figure 4-8b, Eqs. 3-44, 3-45, 3-30) are themselves each proportional to H^2 (which increases toward shore). The current-enhanced bedload component does not increase as rapidly toward shore because waves become more shore-normal in shallower water, which decreases the asymmetry in bedload induced by wave-current superposition. Relative to their magnitude, the landward gradient is much steeper for the wave-driven flux components, which indicates that wave-driven components of sediment transport and morphological change become increasingly important in shallower water.

Instantaneous bed level changes due to each component of wave-averaged sediment transport along the cross-shelf grid for a downwelling favorable wind condition are shown in Figure 4-9. As anticipated based on the across-shelf flux gradient,

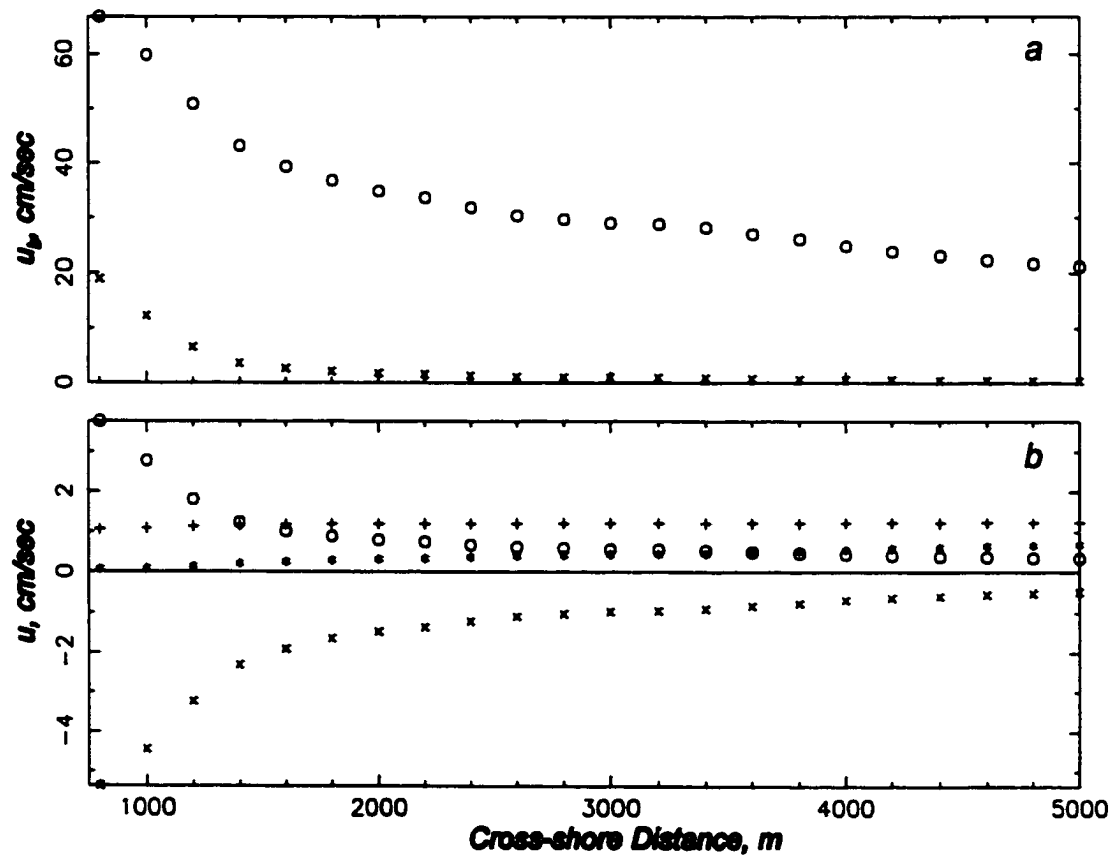


Figure 4-8. a) Near-bottom wave orbital velocity. o - u_{b1} ; x - u_{b2} ; b) Across-shelf current at 1 m ab for each wind- and wave-driven currents calculated on October 3 (19:00 EST). + - u_{x-wind} ; * - u_{y-wind} ; o - u_{return} ; x - u_{stream} .

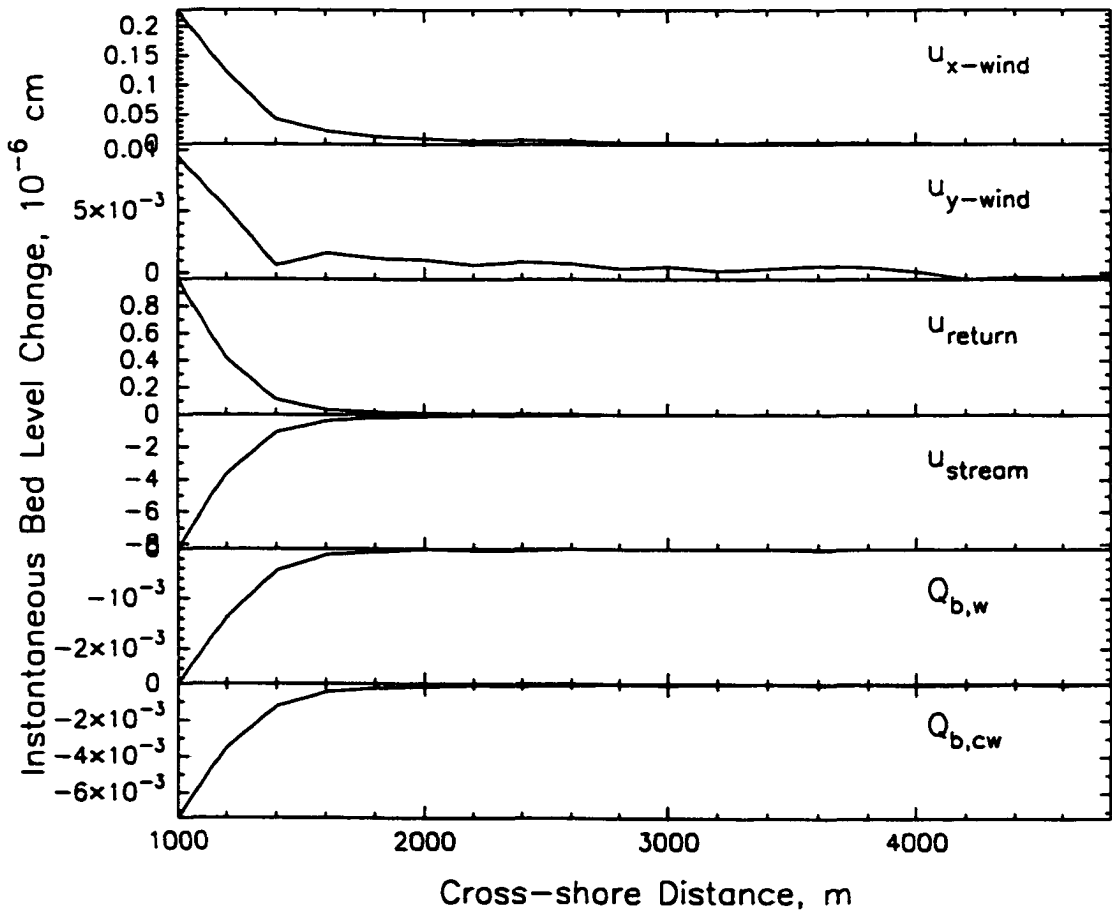


Figure 4-9. Instantaneous bed level change induced by each sediment transport components calculated on October 3 (19:00 EST).

significant bottom change occurs landward of the inner shelf slope break where depth decreases rapidly. For each component of sediment flux, an increase in magnitude of sediment transport toward shore causes the gradient in flux to be of opposite sign to the flux itself. Bed elevation change, which is negatively related to sediment flux (see Eq. 4-11), is then of the same sign as the flux itself. Thus bedload, u_{stream} , which causes onshore directed (i.e., negative) sediment flux, produces erosion; whereas u_{x-wind} , u_{y-wind} , and u_{return} , which cause offshore (i.e., positive) flux, produce deposition. The largest bottom change occurs due to boundary layer streaming, with that due to u_{return} second. The bottom change due to u_{y-wind} is particularly small because the across-shelf gradient and its associated flux are relatively weak.

Figure 4-10 displays modeled and observed bottom change at 13-m depth during October 1996. The 13-m depth was chosen because flow, suspended sediment concentration and bed elevation change were observed at 13 m depth and these data were used to verify various components of the morphodynamic model. Bottom changes by each sediment transport components are also shown in Figure 4-10. The observed bottom change displays accretion, while the modeled, total bottom change exhibits net erosion. The observed bottom change, O(20 cm), is an order of magnitude greater. It is possible that much of the observed bottom change could be due to tripod settling or along-shelf sediment transport. As indicated above, the modeled bottom change is mainly due to boundary layer streaming. It is noted that the trend of bed accretion is similar between the observed bottom change and the modeled bottom change due to return flow, but the observed bottom change is an order of magnitude greater.

4.4.3. Application to Storm Data Set

The morphodynamics model was applied to 24 significant storms which occurred between 1987 and 1993 (Table 4-2). The model formulation was the same as that applied to the October 1996 storm. Bottom change at 13 m depth induced by each component of across-shelf sediment transport is tabulated for all 24 storms in Table 4-3. As indicated

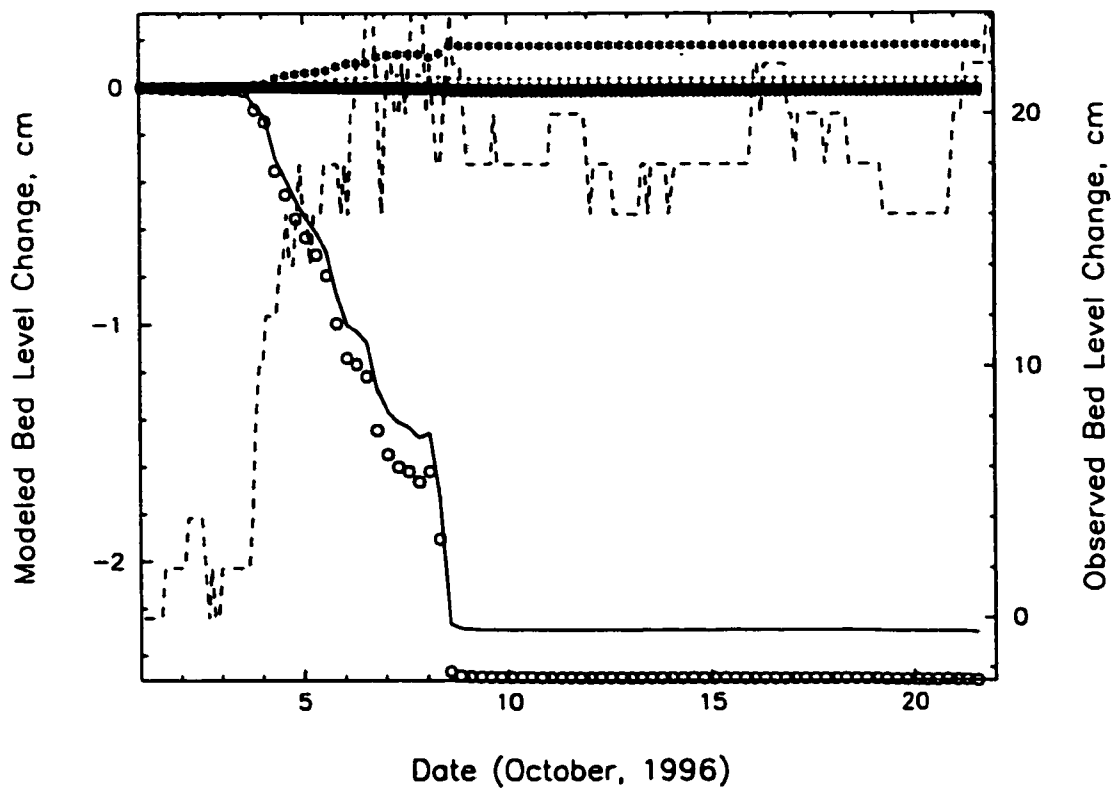


Figure 4-10. Time series of modeled and observed bed level change during October 1996. Modeled bottom change by each sediment transport component is also shown. dashed line - observation; solid line - modeled total bottom change; u_{x-wind} (°); u_{y-wind} (+); u_{return} (*); u_{stream} (o); $Q_{b,w}$ (x); $Q_{b,cw}$ (box).

Date of Storm Peak	Dominant Wind Direction	Percentage of time that breaking occurred on the shoreface	Shoreface Volume Change m ³ /m	Bottom Change on the inner shelf 13-m depth, cm					
				Wind		U _{return}	U _{stream}	BedLoad	
				T _x	T _y			Wave-forced	Current-enhanced
870126	/	0.0	3.20	-0.0001	0.0023	0.0028	-0.0254	0.0000	-0.0001
870217	/	33.3	10.16	0.0504	0.0003	0.4010	-1.6089	-0.0002	-0.0005
870310	/	51.7	34.32	0.1577	-0.0045	1.9915	-8.4668	-0.0007	-0.0042
870425	/	0.0	24.83	0.0032	0.0013	0.0082	-0.0653	-0.0001	-0.0002
890224	/	54.2	50.05	0.0205	0.0086	1.0476	-4.2228	-0.0005	-0.0020
890307	/	36.5	60.52	0.2040	-0.0196	2.4999	-10.4072	-0.0009	-0.0039
891209	/	70.0	13.20	0.1514	-0.0060	2.0107	-7.7728	-0.0006	-0.0022
891224	\	60.7	49.65	0.0337	-0.0006	2.8784	-10.0481	-0.0005	-0.0024
901026	/	31.3	5.34	0.0140	0.0031	0.6376	-2.4030	-0.0003	-0.0005
901110	varying	0.0	-6.26	0.0014	-0.0041	0.0031	-0.0358	0.0000	0.0000
910420	/	4.8	-25.57	0.0081	-0.0022	0.0835	-0.2905	-0.0001	-0.0001
910818	/	0.0	21.24	0.0001	0.0000	0.0000	-0.0023	0.0000	0.0000
911031	/	47.7	-37.83	0.1978	2.0079	1.2377	2.1331	-0.0018	-0.0225
911109	/	33.3	18.92	0.1636	-0.0092	1.2450	-5.2940	-0.0005	-0.0019
920104	\	62.5	4.64	-0.0047	-0.0039	0.1054	-1.0817	-0.0006	-0.0025
920326	\ \	0.0	11.16	0.0000	-0.0001	0.0013	-0.0347	-0.0001	-0.0001
920507	/	60.7	15.28	0.0484	-0.0001	0.1778	-0.8841	-0.0002	-0.0004
920925	/	53.6	24.34	0.0880	-0.0033	0.5395	-2.3033	-0.0003	-0.0006
921210	/	13.7	12.18	0.0481	0.0264	0.5728	-3.7048	-0.0013	-0.0085
930110	/	30.6	-9.34	0.0139	0.0017	0.0309	-0.2371	-0.0001	-0.0003
930313	-	50.0	53.11	-0.0013	-0.0009	0.0126	-0.1348	-0.0001	-0.0002
930406	/	18.8	-9.03	0.0284	0.0037	0.1087	-0.6336	-0.0003	-0.0008
931027	/	16.1	-0.59	0.0311	0.0111	0.8493	-2.8229	-0.0002	-0.0007
931126	/	46.4	5.43	0.0206	-0.0039	0.1527	-0.8027	-0.0002	-0.0005

Table 4-3. Volume change on the shoreface and bottom changes at 13-m depth during storms. Volume change was observed, while bottom change at 13-m depth was modeled.

above, the largest bottom change was associated with u_{stream} , which induced erosion, and the second largest bottom change was associated with u_{return} , which induced accretion. The largest bottom changes induced by u_{stream} occurred during the storms of March 10, 1987, March 7, 1989 and December 24, 1989. Based on bathymetric surveys, Lee et al. (1998) identified these three storms as causing the biggest morphologic change over their study period, and the present model result is consistent with their findings in that respect. The wind-driven components usually induced accretion at 13 m depth. However, the case-by-case predictions depended on the direction of wind. The dominant wind direction for each storm is shown by a wind vector in Table 4-3. With downwelling favorable winds, which is typical for 'northeasters', wind-driven components caused accretion. If upwelling occurred, however, the wind-driven component induced erosion.

There are no bottom profile change data available for the Duck Inner shelf farther than about 800 m offshore. This makes impossible to quantitatively compare the predicted bottom change with observed bottom change. Thus predicted bottom change induced at 13 m depth had to be compared to observed volume change in the vicinity of 9 m depth. Based on surveys immediately before and after each significant storm, volume change per unit distance alongshore was calculated for the inner shelf between 600 and 800 m offshore (Table 4-3). Hydrodynamics within the surf zone is quite different from that outside the surf zone. Sediment transport and resulting bottom profile change will be greater within the surf zone. Thus, surf zone width was modeled and the percentage of time that the region of the inner shelf between 600 and 800 m offshore was within the surf zone was calculated for each storm (Table 4-3). In order to examine the relationship between the observed and predicted bottom change, correlations were calculated for all storms and storms that the region between 600 and 800 m offshore was within the surf zone more (less) than 50 percent of time between two consecutive surveys, along with their statistical significance (Table 4-4). Significant correlations were found between observed morphological change and predicted change due to u_{y-wind} , u_{return} , u_{stream} , and current-enhanced bedload, but not due to u_{x-wind} or wave-forced bedload.

Higher correlation between observed volume change and bottom change

		u_{x-wind}	u_{y-wind}	u_{return}	u_{stream}	Bedload	Bedload
All storms	R^2	0.012	0.212	0.210	0.408	0.006	0.092
	r	0.108	-0.460	0.458	-0.639	0.080	0.303
	F-value	0.26	5.92	5.83	15.18	0.14	2.23
Less** break-ing	R^2	0.037	0.275	0.183	0.568	0.012	0.128
	r	0.192	-0.524	0.428	-0.754	0.111	0.358
	F-value	0.54	5.31	3.14	18.43	0.176	2.06
More*** break-ing	R^2	0.065	0.334	0.076	0.052	0.057	0.002
	r	-0.255	0.578	0.275	-0.228	0.239	0.044
	F-value	0.418	3.00	0.49	0.33	0.363	0.01

* wave-forced bedload transport.

current-enhanced bedload transport.

** Wave breaking occurred less than 50 % of time seaward of the shoreface during a storm.

*** Wave breaking occurred more than 50 % of time seaward of the shoreface during a storm.

Table 4-4. Significance test between shoreface volume change and bottom change induced by each component of modeled currents at 13 m depth. F-values significant at 95% confidence are in bold.

predicted by u_{y-wind} than by u_{x-wind} is consistent with the earlier finding that for the October 1996 storm u_{y-wind} was better correlated than u_{x-wind} with observed currents very near the bed. The higher correlation between observed shoreface volume change and bottom change predicted by current-enhanced bedload relative to wave-induced bedload is consistent with the earlier finding that current-enhanced transport dominated overall bedload during the October 1996 storm. The predicted component most highly correlated to observed profile change is that due to boundary layer streaming. This result is counter-intuitive, since previous observations on the inner shelf of Duck have suggested that cross-shelf sediment flux during storms (and presumably morphological change) are dominated by wind-driven currents (Wright et al., 1991).

4.5. DISCUSSION AND CONCLUSIONS

A physics-based model was developed to determine and understand which components of hydrodynamic forcing and resulting sediment transport are predicted to be most significant to morphological change on the inner shelf of the Middle Atlantic Bight. With incorporation of the predicted results for current and waves, benthic boundary layer structure was estimated using the GMG model with eddy viscosity linearly increasing away from the bed. As discussed above, a linear eddy viscosity is probably inappropriate in the mid-water column. However, as shown in Ch. 2, predicted concentration is largely insensitive to the structure of A_z more than a few 10's of cm above the bed. Predicted suspended sediment concentration reproduced the observed concentration well (Figure 4-3). In spite of difficulties in predicting across-shelf currents accurately, the model for suspended sediment reproduced observed concentration well because the total current vector was used in the GMG model.

The largest offshore flux during the October 1996 storm was predicted to be due to Stokes return flow. Model results suggest the along- and across-shelf components of the wind caused comparable amounts of offshore-directed suspended sediment transport. The largest onshore flux was predicted to be due to boundary layer streaming. Predicted

across-shelf velocity due to u_{stream} is greatest at the top of the wave boundary layer ($O(5$ cm) and decreases into the middle of water column (Figure 3-10). The formulation of u_{stream} may be incorrect because of the reasons discussed in the previous section. Thus the relatively high velocity predicted by u_{stream} near the bottom may overestimate the actual onshore sediment flux.

Modeled bedload sediment transport was directed onshore primarily due to wave asymmetry. The current-enhanced bedload transport is an order of magnitude larger than the wave-forced bedload transport. This is because superposition of strong along-shelf currents on top of wave orbital velocity enhances the onshore-offshore asymmetry in the time-dependent Shield parameters as formulated in (4-5). However, wave-forced bedload transport may dominate during swell with a weak mean current. These two mechanisms which may drive onshore bedload transport have long been recognized (Vincent et al., 1981, Niedoroda et al., 1985; Nielsen, 1992; Traykovsiky et al., 1999), but their relative importance cannot be settled without more direct field measurements. Nonetheless, bedload transport was predicted to be much smaller than the mean component of suspended sediment transport. It is also worth noting that the wave-driven component of suspended sediment transport was directly observed in this study to be much smaller than the mean component, which is consistent with previous observations from Duck, NC (e.g., Wright et al., 1991).

One important finding is that the magnitude of most components of across-shelf sediment transport are predicted to increase towards shore during storms as the inner shelf slope steepens landward of about 13 m depth (Figure 4-7). As a result, sediment transport gradients became larger in this zone and the rate of bottom change increased (Figure 4-9). Thus transport components which are directed onshore generally cause erosion, whereas components which are directed offshore generally cause deposition. Wave-induced sediment flux gradients were greater because the across-shelf gradient in wave properties was greater than the across-shelf current gradient. This may have important ramifications concerning maintenance of the slope of the inner shelf over the long-term.

There are notable limitations with regards to the model predictions of across-shelf sediment transport. Foremost, uncertainties in modeling the across-shelf current directly translate to uncertainties in modeling across-shelf sediment flux. These uncertainties in predicting the across-shelf current overwhelm uncertainties in predicting suspended sediment concentration. This is somewhat counter-intuitive, since prediction of water velocity is typically thought to be simpler than prediction of suspended sediment concentration.

Using a physically-based, wind- and wave-forced morphodynamics model, bottom change was modeled for 24 significant storms which occurred off Duck between 1987 and 1993. Significant correlations were found between observed shoreface volume change between 600 to 800 m offshore and predicted bottom change at 13 m depth forced by u_{y-wind} , u_{return} , u_{stream} , and current-enhanced bedload components, but not for those forced by u_{x-wind} or wave-forced bedload. The only two components which had significant positive correlations with observed bed change were u_{return} and current-enhanced bedload. This result is unexpected, since previous observations of sediment transport on the inner shelf off Duck have suggested that cross-shelf sediment flux during storms (and presumably morphological change) are dominated by wind-driven suspended sediment transport (Wright et al., 1991). The results of the present study indicate that under certain circumstances during downwelling-favored winds, increased wind velocity can actually reduce the strength of downwelling in the inner shelf, and then wave-driven suspended sediment transport may dominate wind-driven suspended sediment transport. This is because increased turbulent mixing can cause eddy viscosity to increase faster than the stress itself. The increased eddy viscosity reduces the strength of downwelling faster than the effect of increased wind stress enhances downwelling.

Three of the four predicted components found to be significantly related to observed morphological change are wave-forced. There is more than one possible explanation for this result. It is possible that morphological change on the inner shelf of the Middle Atlantic Bight is indeed dominated by wave-induced transport during storms. The

morphodynamic model did predict that the largest components of onshore and offshore sediment flux, along with the largest components of corresponding morphological change are the result of wave-driven currents, namely boundary layer streaming and Stokes return flow. Not only do these terms produce the greatest magnitude of across-shelf sediment flux, they also exhibit the strongest gradients in across-shelf flux, which further enhances their ability to produce morphological change.

The two largest absolute correlations with observed profile change are negative, namely those associated with u_{stream} and $u_{y\text{-wind}}$. This may indicate that these two forcings are significantly related to bed change, but that this study's formulation of their across-shelf gradient is incomplete. First, this study has not included any dependence of A_z on the depth of the water column. Lentz et al. (1999) found A_z to increase dramatically landward at the edge of surf zone as wave breaking greatly increased turbulence levels. A_z can also be expected to decrease offshore where wind and bottom stress are less able to fully mix the water column. If A_z is assumed to be inversely related to h , then (3-25) predicts $u_{y\text{-wind}}$ will increase even more quickly toward deeper water. The magnitude of across-shelf sediment transport associated with $u_{y\text{-wind}}$ may then increase seaward instead of landward during storms, and the correlation between $u_{y\text{-wind}}$ and observed bottom change may switch from negative to positive. Second, this study has not accounted for time-dependent eddy viscosity in the wave boundary layer. As noted earlier, modeled bottom change at 13 m depth displayed erosion during the October 1996 storm, while observed bottom change was accretionary with an absolute value an order of magnitude greater than the modeled bed level change. Trowbridge and Madsen (1984a,b) showed that time-dependent eddy viscosity within the wave boundary layer causes u_{stream} to be directed offshore instead of onshore under long waves. A change in the direction of sediment transport due to u_{stream} may then cause the correlation between u_{stream} and observed bottom to become positive.

However, addition of these forcings to the hydrodynamic model only very slightly increased correlations between observed and predicted across-shore velocity during the October 1996 storm. Furthermore, the simple formulations implemented for u_{stream} and

u_{return} in this study are at odds with some theoretical papers (e.g., Trowbridge, 1984a,b; Xu and Bowen, 1994). Thus another possible explanation for this result is the close proximity of the shoreface profile data to the surf zone, particularly during storms. During all the significant storms included in the observed morphology data set, the surf zone extended past 600 m and, in many of the storms, it also extended past 900 m. Lee et al. (1998) suggested that the volume change on the upper shoreface (600-900 m offshore) is closely related to the evolution of the outer bar. Thus the data set itself may be fundamentally impacted by surf zone processes, which, by definition, are dominated by waves. Moreover, other surfzone-related sediment transport processes such as mega-rips are neglected in this study. Gravity currents may develop during extreme storms, but they are also neglected in this study. Inclusion of these processes may improve the prediction of bed level change on the inner shelf. During storms, along-shelf sediment flux dominates across-shelf sediment flux. In this study, gradients in along-shelf sediment flux were assumed to be negligible, but the importance of along-shelf sediment flux gradient remains uncertain. What is needed in future studies of fundamental physical processes impacting the morphology of the inner shelf is a long term data set which unambiguously documents morphological change well outside the surf zone during storms. This study also demonstrates that uncertainties in the magnitude of sediment flux across the inner shelf off Duck, and presumably in other similar environments, are presently limited by our ability to predict across-shelf velocity, not sediment concentration. Thus future studies of inner shelf hydrodynamics also need to regularly incorporate better measurements of the factors which influence across-shelf velocity, including along- and across-shelf barotropic and baroclinic pressure gradients as well as high resolution of stratification. Although suspended sediment was much better resolved in the October 1996 field experiment considered in this paper, data available from the October 1994 CoOP study has the potential to help shed further light on the hydrodynamic forcings which dictate velocity and, thus sediment flux across the inner shelf.

IV. CONCLUSIONS

A benthic boundary layer tripod supporting 6 point-measuring current meters, an upward-looking acoustic Doppler current profiler, and three nearbed profiling acoustic backscatter sensors (ABSs) documented storm and swell conditions during October, 1996 at a depth of 13 m on the inner shelf off Duck, NC. Sediment concentration was higher in the wave boundary layer during storm conditions, but higher ~30 cm above the bed during swell conditions. Three sediment suspension models were used to examine these data, including the two-layered GMG Rouse-type model, Nielsen's combined diffusion and advection model with constant eddy diffusivity, and the three-layered GMGW model plus vertical advection. Suspended sediment concentrations observed by ABSs were used to invert the vertical diffusion equation and solve for eddy diffusivity from 1 to 50 cm ab. During the storm period, diffusivity derived from the ABS up to ~30 cm ab agreed well with viscosity derived above the wave boundary layer from observed current profiles and from the GMG model. During the swell period, diffusivity inferred from observed concentration up to ~30 cm ab did not agree with viscosity derived from observed mean current shear above this level nor with the GMG model. Diffusivity inferred from observed concentration did agree with modeled viscosity due to waves within the wave boundary layer extrapolated to a height greater than the modeled wave boundary layer.

It is speculated that during swell conditions shedding vortices enhanced mass and momentum exchange above the wave boundary layer, extending the eddy viscosity associated with waves above the predicted wave boundary layer. During storm conditions, strong currents prevented vortices from penetrating beyond the predicted wave boundary layer. These two conditions were delineated by a scaling parameter, R , which is the ratio of vertical velocity associated with vortex shedding off bed roughness elements relative to the crossflow velocity associated with the mean current at the top of

the wave boundary layer. The period that observed diffusivity agreed with predicted viscosity outside the wave boundary layer corresponded to the period of low R-values ($R < 0.5$) and strong currents. Higher R-values ($R > 0.5$) and weak currents corresponded to the period that observed diffusivity above the classical wave boundary layer agreed with an extrapolation of predicted viscosity associated with waves out beyond the classical wave boundary layer. During the storm when diffusion was dominant process for suspending sediment, two- and three-layered eddy viscosity reproduced the observed concentration well. During swell (weak current conditions), all the models considered underpredicted the observed concentration if applied with a standard wave boundary layer thickness. However, the Rouse models with enhanced vertical exchange incorporated via a thick wave boundary layer reproduced the observed concentrations remarkably well.

A physics-based model was then developed to determine which components of hydrodynamic forcing and resulting sediment transport are predicted to be most significant to morphological change outside the surf zone on the inner shelf of the middle Atlantic Bight. The simplest possible analytical solutions were sought for wind- and wave-driven currents over the inner shelf which still capture the lowest order hydrodynamics fundamental to across-shelf sediment transport. Two of three wind-driven current models considered are solutions to the time-averaged, linearized momentum equations for a rotating, homogeneous, viscous fluid. One assumes bilinear eddy viscosity (Jenter and Madsen, 1989), while the other assumes constant viscosity (Mitchum and Clarke, 1985). In the third wind-driven current model, the Coriolis term, f_u , in the along-shelf momentum is neglected, which decouples the along-shelf and across-shelf momentum balance and provides the simplest solutions.

Predicted wind-driven currents were compared and correlated with currents observed at 13 m depth off Duck, NC, during October, 1996. The along-shelf current model with bilinear eddy viscosity predicted the along-shelf current structure reasonably well ($r > 0.6$). Constant eddy viscosity was inadequate for reproducing along-shelf velocity because constant A_z was too large near the bottom and consequently the resulting current shear was too small. Across-shelf current velocities predicted with constant eddy

viscosity were correlated better with observed current velocities than were those with bilinear eddy viscosity. This is probably because bilinear eddy viscosity continues to increase away from the boundaries and reaches maximum in the center of the water column, which is unrealistic in the presence of stratification. Across-shelf currents forced by the across-shelf wind were more highly correlated to observed currents in the middle and upper water column (up to $r \sim 0.9$ at surface). Whereas across-shelf currents forced by the along-shelf wind were more highly correlated to observed near-bed currents ($r \sim 0.4$). In general, there was significant disagreement between observed and modeled current velocities, particularly in the across-shelf direction. Large sources of error probably included insufficiently sophisticated eddy viscosity associated with stratification, poorly constrained along- and across-shelf pressure gradients, and wave-induced mean currents.

Simple analytical solutions were found for wave-driven currents associated with Stokes return flows and boundary layer streaming. Wave-driven currents were predicted to be weak in deeper depths (14-20 m) and during low energy conditions, but they were predicted to become dominant towards shore and during high wave energy conditions. Inclusion of wave-induced currents due to boundary layer streaming slightly increased correlations with observed near-bed currents during the storm and caused the total mean current very near the bed to turn shoreward, as observed during the peak of the storm. If only the non-storm period is considered, correlations improve near the bed with the inclusion of u_{return} . The boundary layer streaming solution may be inadequate because it assumes eddy viscosity within the wave boundary layer does not vary with time, while it has been reported that u_{stream} may be negligible or even directed offshore if eddy viscosity varies over individual waves (Trowbridge and Madsen, 1984a,b).

With incorporation of the predicted results for current, waves, and sediment suspension, predicted across-shelf sediment flux associated with the various hydrodynamic forcings were compared. In addition, bedload transport was estimated using Peter-Meyer and Muller's semi-empirical equation. The largest onshore and offshore components of sediment flux during storms were predicted to be due to

boundary layer streaming and Stokes return flow, respectively. Predicted transport due to the across-shelf and along-shelf wind were smaller and generally directed offshore. Predicted bedload transport, which was onshore directed, was about the same magnitude as wind-driven transport. The largest uncertainty in across-shelf transport was not associated with sediment concentration, but with uncertainty concerning the sign, magnitude and proper formulation of across-shelf velocity.

Using a physically-based, wind- and wave-forced morphodynamics model, bottom change was predicted for 24 significant storms which occurred off Duck between 1987 and 1993. The largest bed level change was associated with boundary layer streaming, which induced erosion, and the second largest bottom change was associated with wave-driven Stokes return flow, which induced accretion. Significant correlations were found between observed shoreface volume change between 600- 800 m offshore and predicted bed level change at 13 m due to components forced by the along-shelf wind, Stokes return flow, boundary layer streaming and current-enhanced bedload, but not between observed shoreface volume change and predicted change due to the across-shelf wind or wave-forced bedload. Three of the four predicted components found to be significantly related to observed morphological change are wave-forced. This result contradicts previous observations which have indicated that across-shelf sediment flux during storms is dominated by wind-driven currents. It is possible that morphological change on the inner shelf of the Middle Atlantic Bight is indeed dominated by wave-induced transport during storms. The morphodynamic model did predict the largest components of onshore and offshore sediment flux, along with the largest components of corresponding morphological change to be the result of wave-driven currents. Another possible explanation for this result is the shallow depth of the shoreface profile data, which is partly inside the surf zone during storms. Thus the data set itself may be fundamentally impacted by surf zone processes.

The beach-nearshore profile data collected at the FRF are unique in terms of their survey interval, length, accuracy and cross-shore extent. However, this study indicates a need for a long term data set which unambiguously documents morphological changes

well outside the surf zone during storms. This study also demonstrates that uncertainties in the magnitude of sediment flux across the inner shelf off Duck are presently limited by our ability to predict across-shelf velocity, not sediment concentration. Thus future studies of inner shelf hydrodynamics also need to regularly incorporate better measurements of the factors which influence across-shelf velocity, including along- and across-shelf barotropic and baroclinic pressure gradients as well as high resolution of stratification. During storms, along-shelf sediment flux dominates across-shelf sediment flux. In this study, gradients in along-shelf sediment flux were assumed to be negligible, but the importance of along-shelf sediment flux gradient remains uncertain. Understanding along-shelf sediment flux gradients and associated bottom change is also an important topic for future research.

LITERATURE CITED

- Amos, C.L., A.J. Bowen, D.A. Huntley, and C.F.M. Lewis, Ripple generation under the combined influences of waves and currents on the Canadian continental shelf, *Cont. Shelf Res.*, 8: 1129-1153; 1998.
- Andreopoulos, J., and W. Rodi, Experimental investigation of jets in a crossflow, *J. Fluid Mech.*, 138: 93-127; 1984.
- Bagnold, R.A., Mechanics of marine sedimentation, in *The sea*, Vol. 3, edited by M.N. Hill, pp. 507-528, John Wiley & Sons, New York, 1963.
- Bailard, J.A., An energetics total load sediment transport model for a plane sloping beach, *J. Geophys. Res.*, 86: 10938-10954; 1981.
- Battjes, J.A., R.J. Sobey, and M.J.F. Stive, Nearshore circulation, in *Ocean Engineering Science*, edited by B. LeMehaute, and D.M. Hanes, pp. 467-494, John Wiley & Sons, New York, 1990.
- Birkemeier, W.A., H.C. Miller, S.D. Wilhelm, A.E. DeWall, and C.S. Gorbics, A user's guide to the Coastal Engineering Research Center's Field Research Facility, *Instruction Rep. CERC-85-1*, Coastal Eng. Res. Center, U.S. Army Corps of Eng., Vicksburg, Miss., 1985.
- Birkemeier, W.A., R.J. Nicholls, and G. Lee, Storms, storm groups and nearshore morphologic change, in *Coastal Sediment '99*, pp. 1109-1123, Amer. Soc. Civil Eng., 1999.
- Bowen, A.J., 1980, Simple models of nearshore sedimentation: beach profiles and longshore bars, in *The coastline of Canada*, edited by S.B. McCahn, pp. 1-11, Geological Survey of Canada, 1980.
- Brøker Hedegaard, I., R. Deigaard, and J. Fredsøe, Onshore/offshore sediment transport and morphological modeling of coastal profiles, in *Coastal Sediment '91*, pp. 643-657, Amer. Soc. Civil Eng., 1991.
- Chisholm, T.A., Analysis of field data on near bottom turbulent flows and suspended sediment concentrations, C.E. Thesis, MIT., 1993.

- De Vriend, H.J., J. Zyserman, J. Nicholson, J.A. Roelvink, P. Pechon, and H.N. Southgate, **Medium-term 2DH coastal area modeling**, *Coastal Eng.*, 21: 193-224; 1993.
- Dean, R.G., and M. Perlin, **Intercomparisons of near-bottom kinematics by several wave theories and field and laboratory data**, *Coastal Eng.*, 9: 399; 1986.
- Dean, R.G., and R.A. Dalrymple, *Water wave mechanics for engineers and scientist*, 353 pp., World Scientific, Singapore, 1986.
- Dick, J.E., and J.F.A. Sleath, **Velocities and concentrations in oscillatory flow over beds of sediment**, *J. Fluid Mech.*, 233: 165-196; 1991.
- Dietrichs, W.E., **Settling velocity of natural particles**, *Water Resource Res.*, 18: 1615-1626; 1982.
- Dunne, T.D., and L.B. Leopold, *Water in environmental planning*, 818 pp., W.H. Freeman and Company, 1978.
- Dyer, K.R., *Coastal and estuarine sediment dynamics*, 342 pp., Wiley, New York, 1985.
- Folk, R.L., *Petrology of Sedimentary rock*, 182 pp., Hemphill Pub. Co., Austin, Texas, 1968.
- Fredsøe, J., and R. Deigaard, *Mechanics of coastal sediment transport*, 369 pp., World Scientific, Singapore, 1992.
- Friedrichs, C.T., and L.D. Wright, **Wave effects on inner shelf wind drag coefficients**, In *Proc. 3rd International Symposium, WAVES 97*, pp. 1033-1047, Amer. Soc. Civil Eng., November 3-7, 1997, Virginia Beach, Virginia, USA, 1997.
- Gallagher, E.L., S. Elgar, and R.T. Guza, **Observations of sand bar evolution on a natural beach**, *J. Geophys. Res.*, 103: 3203-3215; 1998.
- Glenn, S.M., and W.D. Grant, **A suspended sediment stratification correction for combined wave and current flows**, *J. Geophys. Res.*, 92: 8244-8264; 1987.
- Grant, W.D., and O.S. Madsen, **The continental shelf bottom boundary layer**, *Annu. Rev. Fluid Mech.*, 18: 265-305; 1986.
- Glenn, S.M., and W.D. Grant, **A suspended sediment stratification correction for combined wave and current flow**, *J. Geophys. Res.*, 92: 8244-8264; 1987.
- Guza, R.T., and E.B. Thornton, **Velocity moments in nearshore**, *J. Waterways, Port, Coastal and Ocean Eng.*, 111: 235-256; 1985.

- Guza, R.T. M.C. Clifton, and F. Rezvani, Field intercomparisons of electromagnetic current meter, *J. Geophys. Res.*, 93, 9302-9314; 1988.
- Haines, J.W., and A.H. Sallenger, Vertical structure of mean cross-shore currents across a barred surf zone, *J. Geophys. Res.*, 99: 14,223-14,242; 1994.
- Hansen, D.V., and M. Rattray, Estuarine circulation induced by diffusion, *J. Mar. Res.*, 36: 281-294; 1972.
- Howd, P.A., and W.A. Birkemeier, Beach and nearshore survey data: 1981-1984, CERC Field Research Facility, *Technical Rep. CERC-87-9*, Coastal Eng. Res. Center, US Army Corps of Eng., Vicksburg, MS., 1987.
- Jenter, H.L., and O.S. Madsen, Bottom stress in wind-driven depth averaged coastal flows, *J. Phys. Oceanog.*, 19: 962-974; 1989.
- Kim, S.C., L.D. Wright, and B.O. Kim, The combined effects of synoptic-scale and local-scale meteorological events on bed stress and sediment transport on the inner shelf of the Middle Atlantic Bight, *Cont. Shelf Res.*, 17: 407-433; 1997.
- Lee, G., and W.A. Birkemeier, Beach and nearshore survey data: 1985-1991, CERC Field Research Facility. *Technical Rep. CERC-93-3*, Coastal Eng. Res. Center, US Army Corps of Eng., Vicksburg, MS., 1993.
- Lee, G., R.J. Nicholls, W.A. Birkemeier, and S.P. Leatherman, Storm-induced variability of the beach-nearshore profile at Duck, North Carolina, USA, 1981-1991, *Mar. Geol.*, 148: 163-177; 1998.
- Lee, T.H., and D.M. Hanes, Comparison of field observations of the vertical distribution of suspended sand and its prediction by models, *J. Geophys. Res.*, 101: 3561-3572; 1996.
- Lee, T.N., E. Willaims, J. Wang, R. Evans, and L. Atkinson, Reponse of South Carolina continental shelf waters to wind and Gulf Stream forcing during winter of 1986, *J. Geophys. Res.*, 94: 10715-10754; 1989.
- Leffler, M.W., C.F. Baron, B.L. Scarborough, K.K. Hathaway, and R.T. Hayes, Annual data summary for 1991, CERC Field Research Facility: Volume 1, Main Text and Appendix A and B, *Technical Rep. CERC-93-3*, Coastal Eng. Res. Center, U.S.

- Army Corps of Eng., Vicksburg, Miss., 1993.
- Lentz, S.J., and C.D. Winant, Subinertial currents on the southern California shelf, *J. Phys. Oceanog.*, 16: 1737-1750; 1986.
- Lentz, S., R.T. Guza, S. Elgar, F. Feddersen, and T.H.C. Herbers, Momentum balances on the North Carolina inner shelf, *J. Geophys. Res.*, 104: 18,205-18,226; 1999.
- Li, M.Z., C.L. Amos, and D.E. Heffler, Boundary layer dynamics and sediment transport under storm and non-storm conditions on the Scotian Shelf, *Mar. Geol.*, 141: 157-181; 1997.
- Longuet-Higgins, M.S., Mass transport in water waves, *Phil. Trans. Royal Soc.*, A245: 535-581; 1953.
- Lynch, J.F., J.D. Irish, T.F. Gross, P.L. Wiberg, A.E. Newhall, P.A. Traykovski, and J.D. Warren, Acoustic measurements of the spatial and temporal structure of the near-bottom boundary layer in the 1990-1991 STRESS experiment, *Cont. Shelf Res.*, 17: 1271-1295; 1997.
- Madsen, O.S., L.D. Wright, J.D. Boon, and T.A. Chisholm, Wind stress, bed roughness and sediment suspension on inner shelf during an extreme storm event, *Cont. Shelf Res.*, 13: 1303-1324; 1993.
- Madsen, O.S., and P.L. Wikramanayake, Simple models for turbulent wave-current bottom boundary layer flow, *Contract Rep. DRP-91-1*, Coastal Eng. Res. Center, U.S. Army Corps of Eng., Vicksburg, MS., 1991.
- Meyer-Peter, E., and R. Müller, Formulas for bedload transport, In *Proc. 2nd Meeting, International Assoc. Hydraul. Res.*, pp. 39-64, Amer. Soc. Civil Eng., Stockholm, Sweden, 1948.
- Miller, H.C., W.A. Birkemeier, and A.E. DeWall, Effects of CERC research pier on nearshore processes, in *Coastal Structures '83*, pp. 765-782, Amer. Soc. Civil Eng., 1983.
- Mitchum, G.T., and A.J. Clarke, The frictional nearshore response to forcing by synoptic scale winds, *J. Phys. Oceanog.*, 16: 934-946; 1986.
- Nielsen, P., Field measurements of time-averaged suspended sediment concentrations under

- waves, *Coastal Eng.*, 8: 51-72; 1984.
- Nielsen, P., *Coastal bottom boundary layers and sediment transport*, 324 pp., World Scientific, Singapore, 1992.
- Niedoroda, A.W., D.J.P. Swift, and T.S. Hopkins, The shoreface, in *Coastal sedimentary environments*, edited by R.A. Davis, pp. 533-624, Springer-Verlag, New York, 1985.
- Osborne, P.D., and B. Greenwood, Frequency dependent cross-shore suspended sediment transport. 2. A barred shoreface, *Mar. Geol.*, 106: 25-51; 1992
- Osborne, P.D., and C.E. Vincent, Vertical and horizontal structure in suspended sand concentrations and wave-induced fluxes over bedforms, *Mar. Geol.*, 131: 195-208; 1996.
- Ott, M.W., and C. Garrett, Frictional estuarine flow in Juan de Fuca Strait, with implications for secondary circulation, *J. Geophys. Res.*, 103: 15,657-15,666; 1988.
- Putrevu, U., and L.A. Svendsen, Vertical structure of the undertow outside the surf zone, *J. Geophys. Res.*, 98: 22707-22716; 1993.
- Rennie, S.E., J.L. Lagier, and S.J. Lentz, Observations of a pulsed buoyancy current downstream of Chesapeake Bay, *J. Geophys. Res.*, 104: 18227-18240; 1999.
- Ribberink, J.S., and A.A. Al-Salem, Sediment transport in oscillatory boundary layers in cases of rippled beds and sheet flow, *J. Geophys. Res.*, 99: 12707-12727; 1994.
- Roelvink, J.A., and M.J.F. Stive, Bar generating cross-shore flow mechanisms on a beach, *J. Geophys. Res.*, 94: 4785-4800; 1989.
- Sheng, J., and A.E. Hay, Sediment eddy diffusivities in the nearshore zone, from multifrequency acoustic backscatter, *Cont. Shelf Res.*, 15: 129-147; 1995.
- Sleath, J.F.A., Measurements of bedload in oscillatory flow, *J. Waterway Port Coastal Ocean Div.*, ASCE, 104: 291-307; 1978.
- Sleath, J.F.A., The suspension of sand by waves, *J. Hydraul. Res.*, 20: 439-452; 1982.
- Sleath, J.F.A., *Sea bed mechanics*, 355 pp., John Wiley & Sons, New York, 1984.
- Sleath, J.F.A., Seabed boundary layers, in *The sea*, vol. 9B, edited by B. Le Méhauté, and D.M. Hanes, pp. 693-728, John Wiley & Sons, 1990.
- Smith, J.D., Modeling of sediment transport on continental shelves, in *The sea*, vol. 6, edited

- by E.D. Goldberg, I.N. McCave, J.J. O'Brian, and J.H. Steele, pp. 539-577, John Wiley & Sons, New York, 1977.
- Stauble, D.K., Long-Term Profile and Sediment Morphodynamics: Field Research Facility Case History, *Technical Report CERC-92-7*, Coastal Eng. Res. Center, U.S. Army Corps of Eng., Vicksburg, MS. 1992.
- Stive, M.J.F., and H.J. de Vriend, Modelling shoreface profile evolution, *Mar. Geol.*, 126: 235-248; 1995.
- Thorne, P.D., P.J. Hardcastle, and R.L. Soulsby, Analysis of acoustic measurements of suspended sediments, *J. Geophys. Res.*, 98: 899-910; 1993.
- Traykovski, P., A.E. Hay, J.D. Irish, and J.F. Lynch, Geometry, migration, and evolution of wave orbital ripples at LEO-15, *J. Geophys. Res.*, 104: 1505-1524; 1999.
- Trowbridge, J., and O.S. Madsen, Turbulent wave boundary layer 1. Model formulation and first-order solution, *J. Geophys. Res.*, 89: 7989-7997; 1984a.
- Trowbridge, J., and O.S. Madsen, Turbulent wave boundary layer 2. Second order theory and mass transport, *J. Geophys. Res.*, 89: 7999-8007; 1984b.
- Van Rijn, L.C., W.C. Nieuwjaar, T. Van Der Kaay, E. Nap, and A. Van Kampen, Transport of fine sands by currents and waves, *J. Waterway, Port, Coastal, and Ocean Eng.*, 119: 123-143; 1993.
- Vanoni, V.A., *Sedimentation engineering*, 745 pp., ASCE, New York, 1975.
- Vincent, C.E., R.A. Young, and D.J.P. Swift, Sediment transport on the Long Island shoreface, North American Atlantic shelf: role of waves and currents in shoreface maintenance, *Cont. Shelf Res.*, 2: 163-181; 1983
- Vincent, C.E., and M.O. Green, Field measurements of the suspended sand concentration profiles and fluxes and of the resuspension coefficient γ_0 over a rippled bed, *J. Geophys. Res.*, 95: 11591-11601; 1990.
- Vincent, C.E., and A. Downing, Variability of suspended sand concentrations, transport and eddy diffusivity under non-breaking waves on the shoreface, *Cont. Shelf Res.*, 14: 223-250; 1994.
- Vincent, C.E., and P.D. Osborne, Predicting suspended sand concentration profiles on a

- macro-tidal beach, *Cont. Shelf Res.*, 15: 1497-1514; 1995.
- Wai, O.W.H., K.W. Bedford, C.M. Libicki, and R.E. Van Evra, The structural evolution of a wave current sediment concentration boundary layer, in *Coastal Sediment '91*, pp. 342-355, Amer. Soc. Civil Eng., 1991.
- Wiberg, P.L., and C.K. Harris, Ripple geometry in wave-dominated environments, *J. Geophys. Res.*, 99: 775-789; 1994.
- Wiberg, P.L., D.E. Drake, and D.A. Cacchione, Sediment suspension and bed armoring during high bottom stress events on the northern California inner continental shelf: measurements and predictions, *Cont. Shelf Res.*, 14: 1191-1219; 1994.
- Wright, L.D., Shelf-surfzone coupling: diabathic shoreface transport, in *Coastal Sediment '87*, pp. 25-40, Amer. Soc. Civil Eng., 1987.
- Wright, L.D., J.D. Boon, S.C. Kim, and J.H. List, Modes of cross-shore sediment transport on the shoreface of the Middle Atlantic bight, *Mar. Geol.*, 96: 19-51; 1991.
- Wright, L.D., O.S. Madsen, T.A. Chisholm, and J.P. Xu, Inner continental shelf transport processes: The middle Atlantic Bight, in *Coastal Dynamics '96*, pp. 867-878, Amer. Soc. Civil Eng., 1994.
- Wright, L.D., *Morphodynamics of inner continental shelf*, 233 pp., CRC Press, 1995.
- Wu, J., Wind-stress coefficients over sea surface from breeze to hurricane, *J. Geophys. Res.*, 87: 9704-9706; 1982.
- Xu, J.P., and L.D. Wright, Tests of bed roughness models using field data from the Middle Atlantic Bight, *Cont. Shelf Res.*, 15: 1409-1434; 1995.
- Xu, Z., and A.J. Bowen, Wave- and wind-driven flow in water of finite depth, *J. Phys. Oceanog.*, 24: 1850-1866; 1994.
- Zhang, Y., D.J.P. Swift, S. Fan, A.W. Niedoroda, and C.W. Reed, Two-dimensional numerical modeling of storm deposition on the northern California shelf, *Mar. Geol.*, 154: 155-167; 1999.

VITA

Guan-hong Lee

Born July 16, 1963 in Young-am, Korea. Graduate from Kyung Hee University in Seoul, Korea in February 1984, with a Bachelor of Science in Geography. Earned a Master of Science in Geography from Kyung Hee University in August 1989. Entered the graduate program of Geography at the University of Maryland in College Park, Maryland in January 1990 and graduated in January 1994 with a Master of Science in Geography. Worked at the Field Research Facility of the US Army Corps of Engineers at Duck, North Carolina from February 1992 to May 1994. Entered the School of Marine Science in September 1994.